



Theses and Dissertations

2015-07-01

Vector Intensity and Holography-Based Acoustic Source Characterization of a Military Jet Aircraft

Trevor Alden Stout
Brigham Young University

Follow this and additional works at: <https://scholarsarchive.byu.edu/etd>

BYU ScholarsArchive Citation

Stout, Trevor Alden, "Vector Intensity and Holography-Based Acoustic Source Characterization of a Military Jet Aircraft" (2015). *Theses and Dissertations*. 8120.
<https://scholarsarchive.byu.edu/etd/8120>

This Thesis is brought to you for free and open access by BYU ScholarsArchive. It has been accepted for inclusion in Theses and Dissertations by an authorized administrator of BYU ScholarsArchive. For more information, please contact scholarsarchive@byu.edu, ellen_amatangelo@byu.edu.

Vector Intensity and Holography-Based Acoustic Source
Characterization of a Military Jet Aircraft

Trevor Alden Stout

A thesis submitted to the faculty of
Brigham Young University
in partial fulfillment of the requirements for the degree of
Master of Science

Kent L. Gee, Chair
Tracianne B. Neilsen
Timothy W. Leishman

Department of Physics and Astronomy
Brigham Young University

July 2015

Copyright © 2015 Trevor Alden Stout

All Rights Reserved

ABSTRACT

Vector Intensity and Holography-Based Acoustic Source Characterization of a Military Jet Aircraft

Trevor Alden Stout
Department of Physics and Astronomy, BYU
Master of Science

The scientific community has employed multiple methods to analyze and describe the jet noise emanating from the turbulent exhaust flow from modern military aircraft engines, with the goal that better characterization of the sound radiation will improve noise reduction efforts. This thesis utilizes three different approaches to characterize the noise source region from a static F-22A Raptor. First, the energy flow field along planes near the aircraft and along an arc is measured using a multidimensional vector intensity probe. The resulting vector intensity maps give a clear indication of the directionality of the noise as a function of frequency at different engine conditions. A straightforward ray-tracing method shows the utility of vector intensity measurements in source characterization by estimating the region from which the loudest portions of sound are emanating. Second, intensity reconstructions from near-field acoustical holography (NAH) provide an estimate of the three-dimensional radiated energy flow field. The sound field is shown to be dominated by mutually incoherent radiation lobes, which can be partially isolated by a partial decomposition method. Lastly, a wavepacket source model is optimized in light of amplitude-based NAH reconstructions near the jet axis. The wavepacket model successfully fits the NAH-reconstructed partial fields, especially at frequencies above 50 Hz, indicating that the source may be modeled by multiple wave packets at each frequency.

Keywords: vector intensity, jet noise, acoustical holography

ACKNOWLEDGMENTS

I'd like to first acknowledge and thank my committee members, Drs. Kent Gee, Tracianne Neilsen, and Timothy Leishman, for always finding time to teach me how to research and develop as an acoustician. They have taught me not only in academic settings, but also in frequent meetings and informal discussions, and with their examples of dedication to the science and to their colleagues. I am honored to have worked with them. Thanks to the generosity of Drs. Gee and Neilsen, I have been able to attend many national and international conferences, which have helped me find the perspective necessary for this work. I'm also honored to have worked with my fellow students, many of whom have contributed to this thesis. Of them, I'd like to especially thank Alan Wall, Benjamin Christensen, Blaine Harker, Brent Reichman, and Eric Whiting. Finally, I'd like to thank my parents and my brothers and their wives for always showing interest in my research, no matter how esoteric it might be.

SBIR DATA RIGHTS - (DFARS 252.227-7018 (JUNE 1995)); Contract Number: FA8650-08-C-6843; Contractor Name and Address: Blue Ridge Research and Consulting, LLC, 29 N Market St, Suite 700, Asheville, NC Expiration of SBIR Data Rights Period: March 17, 2016 (Subject to SBA SBIR Directive of September 24, 2002) The Government's rights to use, modify, reproduce, release, perform, display, or disclose technical data or computer software marked with this legend are restricted during the period shown as provided in paragraph (b)(4) of the Rights in Noncommercial Technical Data and Computer Software—Small Business Innovation Research (SBIR) Program clause contained in the above identified contract. No restrictions apply after the expiration date shown above. Any reproduction of technical data, computer software, or portions thereof marked with this legend must also reproduce the markings. Portions of this thesis have been cleared under the following statement: Distribution A – Approved for Public Release;

Distribution is Unlimited 88ABW-2013-4808.

TABLE OF CONTENTS

TABLE OF CONTENTS.....	v
LIST OF FIGURES	vii
Chapter 1.....	1
1.1 Background	1
1.2 Thesis outline	3
1.3 Experiment	3
Chapter 2.....	6
2.1 Intensity methodology.....	7
2.2 Tetrahedral intensity probe.....	8
2.3 PAGE methodology	10
2.4 Performance of PAGE vs FD.....	12
2.5 Vector intensity maps.....	16
2.6 Analysis.....	22
2.6.1 Maximum intensity directions	22
2.6.2 Ray-tracing.....	26
2.6.3 Ray-tracing validation.....	29
Chapter 3.....	33
3.1 Introduction	34
3.2 Theoretical formulation.....	35
3.3 OLVR Partial field decomposition.....	39
3.4 Results	42
3.4.1 Military reconstructed intensity	44
3.4.2 Afterburner reconstructed intensity	49
3.5 Comparison with probe intensity estimates	55
Chapter 4.....	59
4.1 Introduction	60
4.2 SONAH wavepacket optimization.....	62
4.3 Optimization results	64
Chapter 5.....	79
5.1 Conclusion.....	79
5.2 Contributions.....	81

5.3	Future work	81
	References.....	82
	Appendix.....	90
A.	Intensity analysis of the dominant frequencies of military jet aircraft noise.....	90
A.1	Introduction	90
A.2	Spectral Analysis	92
A.3	Intensity Measurements.....	95
A.4	Intensity Simulations	101
	Conclusions.....	103

LIST OF FIGURES

- Figure 1-1. Measurement setup, with F-22 tethered to concrete run-up pad. The rectangular microphone rig is visible on the right, atop an aluminum guide rail. 5
- Figure 1-2. View of 90-microphone rig with attached tetrahedral intensity probe (a), and close-up of intensity probe (b). The microphones are attached to the vertices of the tetrahedron, with diaphragms facing inward. 5
- Figure 2-1. Top-down schematic of intensity probe data locations along the measurement planes and arc, (black). A schematic of the probe microphone orientation indicating channel number is superimposed, not to scale, (blue). Compare with Fig. 1-2. 8
- Figure 2-2. Waveforms as recorded by the four intensity probe microphones at two different locations, near $z = 8$ meters (a), and near $z = 17$ m downstream (b). Note the apparent arrival time at each microphone differs between the two locations. 10
- Figure 2-3. One-third octave sound pressure levels (SPL) averaged over the four intensity microphones, compared with the sound intensity levels (SIL) estimated using the finite difference (FD) and the PAGE method. The FD method underpredicts the intensity level beginning at 1 kHz, while the PAGE method SIL matches the SPL up to about 8 kHz. The disagreement between both SIL estimates and measured SPL near 100 Hz is likely due to error in the relative phase calibration between the four microphones on the intensity probe. 14
- Figure 2-4. Acoustic vector intensity maps of the F-22 sound field at 1250 (top) and 5000 Hz (bottom) at afterburner, estimated using the PAGE method (a, left) and the FD method (b, right). The estimated shear layer of the jet exhaust is indicated by a blue dashed line. Though both methods agree at 1.25 kHz, for 5 kHz the PAGE method gives physically reasonable intensity directions and magnitudes, while the vector directions predicted by the FD method are clearly nonphysical, and the magnitudes are much lower compared to PAGE estimations. 15
- Figure 2-5. Acoustic intensity at afterburner engine conditions for select one-third octave band center frequencies. The intensity probe was located at the base of each vector arrow. The estimated shear layer is indicated by a blue dashed line. Vector length scaling used by the rendering program is kept consistent between this figure and Fig. 2-7. Note how the region of maximum intensity shifts upstream with increasing frequency, while the overall sound intensity level decreases. Maximum intensity magnitude levels are higher at afterburner than at military engine conditions by up to 5 dB. 17
- Figure 2-6. Acoustic intensity at afterburner engine conditions for select one-third octave band center frequencies. The intensity probe was located at the base of each vector arrow. The estimated shear layer is indicated by a blue dashed line. Vector length scaling used by the rendering program is kept consistent between this figure and Fig. 2-8. Note how the maximum intensity region location is generally consistent at these frequencies, while the overall sound intensity level decreases at higher frequencies. 18

Figure 2-7. Similar to Fig. 2-5 except at military power. Vector scaling is kept consistent between this figure and Fig. 2-5. 19

Figure 2-8. Similar to Fig. 2-6 except at military power. Vector scaling is kept consistent between this figure and 2-6. Maximum intensity magnitude levels are lower at military than at afterburner engine conditions by up to 5-7 dB. 20

Figure 2-9. Angular span of the acoustic intensity vectors contained within the 3dB-down regions along plane 2 at one-third octave band center frequencies, after intensity vectors are integrated over one-third octave bands, at afterburner (top) and for military engine conditions (bottom). Angles are measured from the engine inlet. For both conditions, the range of vector directions increases in width for frequencies about 1000 Hz for afterburner and 600 Hz for military, indicating the prominence of a more omnidirectional source. The rapid change at 200-250 Hz is an effect of the transition between two maximum intensity locations with discrete directionalities in that frequency range and is more apparent at military engine conditions. The forward shift at 100 Hz may be due to error in phase calibration within the intensity probe. Also, note how angles at afterburner are up to 10° farther forward than for military conditions. 23

Figure 2-10. Generalized equivalent source locations as a function of frequency found from intensity ray-tracing, at afterburner (top) and military engine conditions (bottom). Ray-tracing results are presented at one-third octave band center frequencies, from intensity vectors integrated over each band. The rapid transition region around 200 Hz corresponds to the switch in dominant intensity regions seen in Figs. 2-5 and 2-7, and is more apparent at military engine conditions. At all frequencies, results at afterburner are about 1 m farther downstream than for military. 28

Figure 2-11. Simulated intensity fields at 100 Hz (a), resulting from either a correlated or uncorrelated array of amplitude-shaded monopoles, and ray-tracing results compared to the actual source distribution, (b). In (a), the black vectors represent the acoustic intensity from an uncorrelated distribution of monopoles, and the blue vectors show intensity from a correlated distribution. In (b), the solid black line shows the amplitude shading applied to the line array of monopoles for both cases. The dark blue bar indicates the ray-traced source width from the resultant 3 dB-down region in the uncorrelated case; the light blue indicates the same for the correlated case. A dotted line shows the amplitude that is 3 dB down from the maximum of the source distribution. Note how the ray-tracing method predicts a broader source extent in the correlated case, while approximately the top 1 dB of source energy is represented in the source predictions for both source models. 31

Figure 2-12. Similar to Fig. 2-11 except at 250 Hz. 32

Figure 3-1. M-SONAH total reconstructed intensity field (top left) at nozzle height of $y = 1.9$ m and the first five OLVR partial fields decomposed from the total field, at 50 Hz and military conditions. Sound intensity levels are indicated by the color map and are scaled to reflect a 5.9 Hz bin width. The color scale and vector scaling is consistent between partial fields. Data within the approximate shear layer has been removed. 44

Figure 3-2. M-SONAH total reconstructed intensity field (top left) and the first five OLVR partial fields decomposed from the total field, at 80 Hz and military conditions. 45

Figure 3-3. M-SONAH total reconstructed intensity field (top left) and the first five OLVR partial fields decomposed from the total field, at 100 Hz and military conditions.	45
Figure 3-4. M-SONAH total reconstructed intensity field (top left) and the first five OLVR partial fields decomposed from the total field, at 125 Hz and military conditions.	46
Figure 3-5. M-SONAH total reconstructed intensity field (top left) and the first five OLVR partial fields decomposed from the total field, at 160 Hz and military conditions.	46
Figure 3-6. M-SONAH total reconstructed intensity field (top left) and the first five OLVR partial fields decomposed from the total field, at 200 Hz and military conditions.	47
Figure 3-7. M-SONAH total reconstructed intensity field (top left) and the first five OLVR partial fields decomposed from the total field, at 250 Hz and military conditions.	47
Figure 3-8. M-SONAH total reconstructed intensity field (top left) and the first five OLVR partial fields decomposed from the total field, at 315 Hz and military conditions.	48
Figure 3-9. M-SONAH total reconstructed intensity field (top left) and the first five OLVR partial fields decomposed from the total field, at 400 Hz and military conditions.	48
Figure 3-10. M-SONAH total reconstructed intensity field (top left) and the first five OLVR partial fields decomposed from the total field, at 500 Hz and military conditions.	49
Figure 3-11. M-SONAH total reconstructed intensity field (top left) and the first five OLVR partial fields decomposed from the total field, at 32 Hz and afterburner engine conditions. Sound intensity levels are indicated by the color map and are scaled to reflect a 5.9 Hz bin width. The color scale and vector scaling is consistent between partial fields. Data within the approximate shear layer has been removed.	49
Figure 3-12. M-SONAH total reconstructed intensity field (top left) and the first five OLVR partial fields decomposed from the total field, at 50 Hz and afterburner engine conditions.	50
Figure 3-13. M-SONAH total reconstructed intensity field (top left) and the first five OLVR partial fields decomposed from the total field, at 80 Hz and afterburner engine conditions.	50
Figure 3-14. M-SONAH total reconstructed intensity field (top left) and the first five OLVR partial fields decomposed from the total field, at 100 Hz and afterburner engine conditions.	51
Figure 3-15. M-SONAH total reconstructed intensity field (top left) and the first five OLVR partial fields decomposed from the total field, at 125 Hz and afterburner engine conditions.	51
Figure 3-16. M-SONAH total reconstructed intensity field (top left) and the first five OLVR partial fields decomposed from the total field, at 160 Hz and afterburner engine conditions.	52
Figure 3-17. M-SONAH total reconstructed intensity field (top left) and the first five OLVR partial fields decomposed from the total field, at 200 Hz and afterburner engine conditions.	52
Figure 3-18. M-SONAH total reconstructed intensity field (top left) and the first five OLVR partial fields decomposed from the total field, at 250 Hz and afterburner engine conditions.	53
Figure 3-19. M-SONAH total reconstructed intensity field (top left) and the first five OLVR partial fields decomposed from the total field, at 315 Hz and afterburner engine conditions.	53

Figure 3-20. M-SONAH total reconstructed intensity field (top left) and the first five OLVR partial fields decomposed from the total field, at 400 Hz and afterburner engine conditions. 54

Figure 3-21. M-SONAH total reconstructed intensity field (top left) and the first five OLVR partial fields decomposed from the total field, at 500 Hz and afterburner engine conditions. 54

Figure 3-22. M-SONAH reconstructed intensity at intensity probe locations compared with intensity estimates calculated from intensity probe measurements, at one-third octave band center frequencies and afterburner engine conditions. Internal scaling used by the rendering program to define vector lengths is kept consistent. The color map indicates the difference in sound intensity level between the reconstruction and measurement. Below about 200 Hz, vector directions at the measurement planes differ by up to about 10 degrees, indicative of some phase mismatch in the intensity probe microphones. In addition, some nulls in the reconstructed intensity magnitudes along the measurement planes are not as prominent in the measured intensity, between 160-250 Hz. The intensity reconstruction along the measurement arc follows closely with measurement up to 500 Hz, where the frequency limit of the M-SONAH algorithm is reached. 57

Figure 4-1. First three OLVR partial fields along the F-22 lip line (blue), and the corresponding wavepacket best fits (black), at 40 Hz and afterburner engine conditions. Amplitude is shown by dotted lines, and the real parts of both distributions are given by solid lines. Where all the iterations of the optimization algorithm closely coincided, the resultant best fits lie on top of each other. 66

Figure 4-2. Amplitude of the wavenumber spectra corresponding to the OLVR partial fields at the lip line (solid, black), wavepacket best fits (dotted, black), and the randomized initial conditions given to the optimization algorithm (solid, red) at 40 Hz and afterburner engine conditions. Results for the first three partial fields are shown from left to right. For each partial field, the output from two example optimizations (top and bottom) are tabulated and shown. 66

Figure 4-3. First three OLVR partial fields along the F-22 lip line (blue), and the corresponding wavepacket best fits (black), at 50 Hz and afterburner engine conditions. 67

Figure 4-4. Amplitude of the wavenumber spectra corresponding to the OLVR partial fields at the lip line (solid, black), wavepacket best fits (dotted, black), and the initial conditions given to the optimization algorithm (solid, red) at 50 Hz and afterburner engine conditions. 67

Figure 4-5. First three OLVR partial fields along the F-22 lip line (blue), and the corresponding wavepacket best fits (black), at 63 Hz and afterburner engine conditions. 68

Figure 4-6. Amplitude of the wavenumber spectra corresponding to the OLVR partial fields at the lip line (solid, black), wavepacket best fits (dotted, black), and the initial conditions given to the optimization algorithm (solid, red) at 63 Hz and afterburner engine conditions. 68

Figure 4-7. First three OLVR partial fields along the F-22 lip line (blue), and the corresponding wavepacket best fits (black), at 80 Hz and afterburner engine conditions. 69

Figure 4-8. Amplitude of the wavenumber spectra corresponding to the OLVR partial fields at the lip line (solid, black), wavepacket best fits (dotted, black), and the initial conditions given to the optimization algorithm (solid, red) at 80 Hz and afterburner engine conditions. 69

Figure 4-9. First three OLVR partial fields along the F-22 lip line (blue), and the corresponding wavepacket best fits (black), at 100 Hz and afterburner engine conditions. 70

Figure 4-10. Amplitude of the wavenumber spectra corresponding to the OLVR partial fields at the lip line (solid, black), wavepacket best fits (dotted, black), and the initial conditions given to the optimization algorithm (solid, red) at 100 Hz and afterburner engine conditions..... 70

Figure 4-11. First three OLVR partial fields along the F-22 lip line (blue), and the corresponding wavepacket best fits (black), at 125 Hz and afterburner engine conditions. 71

Figure 4-12. Amplitude of the wavenumber spectra corresponding to the OLVR partial fields at the lip line (solid, black), wavepacket best fits (dotted, black), and the initial conditions given to the optimization algorithm (solid, red) at 125 Hz and afterburner engine conditions..... 71

Figure 4-13. First three OLVR partial fields along the F-22 lip line (blue), and the corresponding wavepacket best fits (black), at 160 Hz and afterburner engine conditions. 72

Figure 4-14. Amplitude of the wavenumber spectra corresponding to the OLVR partial fields at the lip line (solid, black), wavepacket best fits (dotted, black), and the initial conditions given to the optimization algorithm (solid, red) at 160 Hz and afterburner engine conditions..... 72

Figure 4-15. First three OLVR partial fields along the F-22 lip line (blue), and the corresponding wavepacket best fits (black), at 200 Hz and afterburner engine conditions. 73

Figure 4-16. Amplitude of the wavenumber spectra corresponding to the OLVR partial fields at the lip line (solid, black), wavepacket best fits (dotted, black), and the initial conditions given to the optimization algorithm (solid, red) at 200 Hz and afterburner engine conditions..... 73

Figure 4-17. First three OLVR partial fields along the F-22 lip line (blue), and the corresponding wavepacket best fits (black), at 250 Hz and afterburner engine conditions. 74

Figure 4-18. Amplitude of the wavenumber spectra corresponding to the OLVR partial fields at the lip line (solid, black), wavepacket best fits (dotted, black), and the initial conditions given to the optimization algorithm (solid, red) at 250 Hz and afterburner engine conditions..... 74

Figure 4-19. First three OLVR partial fields along the F-22 lip line (blue), and the corresponding wavepacket best fits (black), at 315 Hz and afterburner engine conditions. 75

Figure 4-20. Amplitude of the wavenumber spectra corresponding to the OLVR partial fields at the lip line (solid, black), wavepacket best fits (dotted, black), and the initial conditions given to the optimization algorithm (solid, red) at 315 Hz and afterburner engine conditions..... 75

Figure 4-21. First three OLVR partial fields along the F-22 lip line (blue), and the corresponding wavepacket best fits (black), at 400 Hz and afterburner engine conditions. 76

Figure 4-22. Amplitude of the wavenumber spectra corresponding to the OLVR partial fields at the lip line (solid, black), wavepacket best fits (dotted, black), and the initial conditions given to the optimization algorithm (solid, red) at 400 Hz and afterburner engine conditions..... 76

Figure 4-23. Convective velocity U_c in meters per second as a function of frequency, averaged over iterations of the optimization algorithm. These values are extracted from the parameters corresponding to wavepackets that best fit the OLVR partial fields. Results averaged over

the first three partial fields, with weighting applied corresponding to the total summed energy in each partial field, are shown at the top left.	77
Figure 4-24. Minimum-cost wavepacket convective velocities as a function of wavepacket peak location. The results pertaining to each partial field are distinguished by symbol and color.	77
Figure A-1. (a) F-22 engine firing with rig and probe in place, and (b) close-up of the intensity probe positioned on top of the microphone array. The array and probe took measurements at several locations along guide rails while the engine was cycled through four power conditions.	91
Figure A-2. Top-down schematic of data locations for the F-22 measurements. The red triangles indicate the center of the microphone rig with the intensity probe attached. The mark at 5.5 m downstream describes the estimated source location, set as the center of the 22.9m arc. The blue dots show locations for the ground-based reference array.	92
Figure A-3. One-third octave sound pressure levels measured according to direction from assumed source (5.5 m downstream), for military engine conditions (compare the same for afterburner in Ref. 21).	93
Figure A-4. One-third-octave SPL recorded by the ground microphone array for military engine conditions. Note the two distinct high-level regions centered about 125 Hz and 400 Hz that dominate the radiation from 8m to 24 m downstream.	94
Figure A-5. (a) Coherence between microphones along the ground-based array at 200 Hz. (b) Power spectral density (PSD) values at 200 Hz, along ground-based array. Note the two lobes of high coherence at $z = 9\text{-}16$ m and past $z = 20$ m.	95
Figure A-6. Intensity results (blue arrows) at 800 Hz, including an example 3 dB-down region, shown as a circle on the second measurement plane. The intensity vectors are traced backwards to the jet centerline (red lines) to give an estimated source region at this frequency.	96
Figure A-7. (a) Height-averaged one-third-octave spectra as measured on the 90-microphone rig at 4.1 m from the shear layer (plane 1), and (b) generalized source location region vs frequency based on intensity results for military engine conditions. Error bars in (a) indicate regions within 3 dB of the spectral maximum, which is indicated as a white dot. At about 11 m downstream, the peak frequency jumps from 250 to 125 Hz. Left and right bounds in (b) describe the edges of the generalized source region estimated from tracing the intensity vectors within 3dB of the maximum; note how the source contracts and moves upstream rapidly after 200 Hz.	97
Figure A-8. (a) Height-averaged one-third-octave spectra as measured on the 90-microphone rig at 4.1 m from the shear layer (plane 1) and (b) generalized source location region vs frequency based on intensity results for afterburner engine conditions. As in Fig. A-7, error bars in (a) indicate regions within 3 dB of the spectral maximum, which is indicated as a white dot. At about 10.5 m downstream, the peak frequency jumps from 250 to 125 Hz. Left and right bounds in (b) describe the edges of the generalized source region; note how the source	

contracts and moves upstream rapidly after about 200 Hz. However, the source region remains broader and extends farther downstream than in Fig. A-7(b). 98

Figure A-9. Intensity measurements (blue arrows) at 136 Hz, military condition on plane 2 and the arc at 23 m. The red lines indicate 120 and 140 degrees relative to the engine inlet. The radiation at this frequency is dominated by one intensity maximum at $z = 20$ m. 99

Figure A-10. Similar to Fig. A-9. Intensity measurements at 232 Hz, military condition. Note how the radiation at this frequency produces two distinct maxima, seen spatially at about $z = 10$ m and $z = 20$ m. 100

Figure A-11. Similar to Fig. A-9. Intensity measurements at 316 Hz, military condition. The radiation at this frequency is dominated by one intensity maximum at $z = 10$ m. 100

Figure A-12. (a) Location-dependent amplitude weightings of the monopole arrays, and (b) spectral response of filters applied to the noise from both correlated arrays. Coloring for each array is consistent between (a) and (b). The locations were chosen based on intensity measurement results, with centers at $z = 5$ m and $z = 10.5$ m downstream. 102

Figure A-13. Intensity simulated at the first measurement plane due to the two correlated line arrays, for 160 Hz (top) and 200 Hz (bottom). The simulation is overlaid onto measurements at 160 Hz and 200 Hz for military engine condition (blue arrows). 103

Chapter 1

Introduction

1.1 Background

With each advance in military air power, the jet engines used to propel fighter aircraft may provide more thrust, but they potentially produce more noise than the less powerful engines that came before them. Technicians, aircraft carrier personnel, and others who are exposed to these loud sound levels incur hearing loss¹, even with earplugs and muffs. To combat this, the Office of Naval Research has funded projects with the eventual goal of reducing jet noise. However, making military jets quieter without loss of thrust is a difficult task.

One difficulty faced in working towards jet noise reduction is a lack of understanding of the noise source. While it is true that the engine itself produces some noise, the bulk of the sound actually originates from behind the engine, in the plume of air that the engine propels behind the aircraft.^{2,3} This quickly-moving air mixes with the ambient air, creating turbulence, which is the main source of the noise coming from the aircraft. In order to understand this noise source,

microphones are typically used to measure sound pressure at multiple points outside of the jet plume.^{4,5} The plume itself is extremely hot and in violent motion, so that placing microphones directly in the plume is impractical.

Vector acoustic intensity, which describes the sound energy flow from an acoustic source, has had little previous application in aeroacoustics. Since it is a vector quantity, acoustic intensity contains information about both the magnitude and direction of energy flow, while measurement of the sound pressure alone only accounts for magnitude. Within this thesis, “intensity” refers to sound power flux density vector, unlike the somewhat common usage denoting overall sound power level or OASPL, which is dependent only on the amplitude of the pressure wave.⁶ The acoustic intensity can help to describe a sound field more completely and, typically, with fewer measurement locations, depending on the measurement standard. Despite its advantages, the microphone arrays used in aeroacoustic studies are usually not chosen or optimized for vector acoustic intensity estimation. In jet noise analysis, intensity data have been used to verify results from other inverse methods (such as beamforming⁷) and to describe sound sources.^{2, 8} Until recently, the most in-depth example of analyzing intensity from jet noise sources were two-dimensional intensity measurements by Jaeger and Allen⁸ of a Mach 0.2-0.6 lab-scale jet. Jaeger and Allen traced intensity vectors directly back to the jet centerline, using the intercepts to describe the source region. Given the low Mach number, the intensity vectors were found to originate from a relatively compact region. More recently, the sound field near a solid rocket motor plume has been sampled using three-dimensional intensity probes.^{9,10} In these analyses, acoustic intensity vectors indicate an extended source region in the jet, consistent with other studies of turbulent flows.¹¹

1.2 Thesis outline

This thesis describes three different approaches toward jet noise source characterization: vector intensity measurements near a military aircraft (Chapter 2), near-field acoustical holography (NAH) to produce energy-flow visualizations (Chapter 3), and NAH-informed wavepacket modeling optimizations (Chapter 4). Chapter 2 has been modified from a manuscript¹² prepared for the Journal of the Acoustical Society of America (“Source characterization of full-scale jet noise using vector intensity”). In addition, a published article in Proceedings of Meetings on Acoustics,¹³ which describes intensity analysis throughout an important frequency range is included as Appendix A. With the exception of Chapter 4, these topics focus directly on the importance of intensity as an acoustic quantity. However, the work presented in Chapter 4 is foundational for future intensity-based wavepacket modeling. The remainder of Chapter 1 will be devoted to a brief description of the primary experiment from which the analyses in this thesis are derived.

1.3 Experiment

The acoustical data presented herein were taken by a team of researchers from Blue Ridge Research and Consulting, LLC, and Brigham Young University in the vicinity of a tethered Lockheed Martin/Boeing F-22A Raptor with one engine operated at multiple conditions while the other engine remained idle. The primary purpose for these measurements was to perform NAH using a point-to-point scan-based approach with a 90-microphone rectangular array and a stationary 50 microphone ground-based reference array. Multiple references describe the experimental setup and data acquisition system developed for this purpose.^{14,15} At afterburner and

military engine conditions, data were acquired at a sampling rate of 48 kHz and 96 kHz, respectively. A significantly better understanding of the turbulent mixing noise in the geometric near field of a high-power military jet aircraft has resulted from the previous analysis of the data, using holography¹⁶ and partial coherence decomposition,^{17,18} correlation and coherence analysis,¹⁹ multiple beamforming methods,²⁰ similarity spectra analysis,^{21,22} and equivalent source modeling.²³ Attached to the top of the 90 microphone array was a custom three-dimensional intensity probe that was concurrently being developed for rocket noise source measurements. The probe (described below) was used to take measurements at the NAH scan positions (see Fig. 2-1 and the intensity maps in Chapter 2) along two measurement planes, parallel to the estimated shear layer at offset distances of 4.1 m (measurement plane 1) and 5.6 m away (plane 2), as well as on an arc with radius 22.9 m. With the exception of the run-up pad and surrounding ground, scattering bodies were placed far away to have low impact on the geometric near-field measurements. Scattering from the probe body itself precludes analysis of intensity results above about 7 kHz (see Sec. 2.4).

Because the results of this analysis stem from the point-to-point measurements of the intensity vector field made with a single probe over many engine runups, repeatability is crucial. The consistency of the measurements has been previously documented by analyses of the overall and spectral levels using the stationary, ground-based microphone array. For military and afterburner engine conditions, respectively, the standard deviation of the OASPLs across all scans averaged to < 1 dB.¹⁴ Thus, the intensity measurements at each point can be combined to provide a single map of the intensity field near the F-22, within this error.



Figure 1-1. Measurement setup, with F-22 tethered to concrete run-up pad. The rectangular microphone rig is visible on the right, atop an aluminum guide rail.

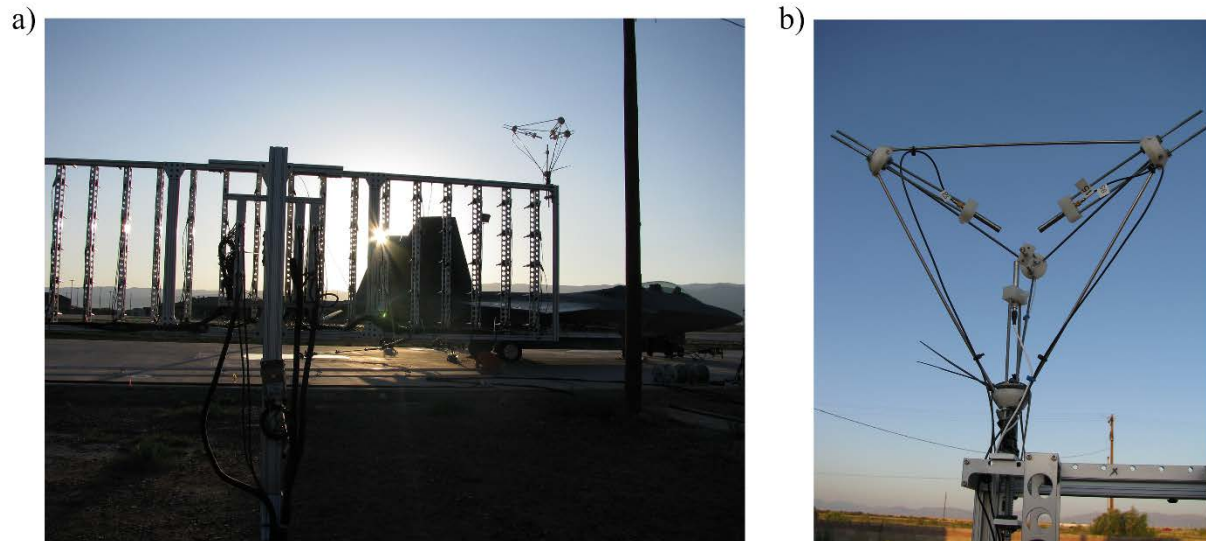


Figure 1-2. View of 90-microphone rig with attached tetrahedral intensity probe (a), and close-up of intensity probe (b). The microphones are attached to the vertices of the tetrahedron, with diaphragms facing inward.

Chapter 2

Intensity measurements

This chapter contains analysis of the measured vector intensity field near an installed, high-powered military jet engine, in an effort to better understand the acoustic source and radiation characteristics and to demonstrate the utility of these measurements in jet aeroacoustic analysis. Implementation of a recently developed intensity calculation method,²⁴ which allows for more accurate intensity estimation over a much broader frequency range when compared with the traditional method, is described. Resultant intensity maps at afterburner and military (full-throttle) engine conditions are displayed at chosen one-third octave band center frequencies. From this, the maximum amplitude intensity region within the measurement aperture is defined to be 3 dB down from the data along a line parallel to the shear layer, and the angles of the intensity vectors contained within are evaluated to gain a better understanding of how the resultant maximum radiation direction compares to far-field directivity. The intensity vectors from the 3 dB-down region vectors are traced back to the centerline to provide an estimate of the maximum source

region, the meaning of which is better understood through an analytical tracing example involving the measurement geometry and a wavepacket-like source model. The results are analyzed as a function of frequency and engine condition (military and afterburner powers).

2.1 Intensity methodology

The time-averaged acoustic vector intensity at a single point is obtained as the time-integrated product of the collocated acoustic particle velocity, a vector, and pressure, a scalar. The acoustic particle velocity, which is the more challenging to obtain, can be measured directly using, e.g., commercially available, specialized sensors involving a pair of heated wires.²⁵ However, these sensors are sensitive to nonacoustic velocity fluctuations, such as wind or entrained flow, which exist around a rocket or jet aircraft plume.²⁶ The acoustic particle velocity can instead be approximated via the pressure gradient in Euler's equation using a multi-microphone probe that simultaneously gives the pressure using the same microphones. This approach is commonly used and has been successfully applied to the near-field characterization of solid rocket motor plumes.^{10,27-28} The traditional calculation scheme is the finite difference (FD), or p-p method,²⁹ which estimates the active component of the intensity component between two microphones by approximating the spatial gradient of the pressure. This estimation method suffers from frequency-dependent bias, underestimating the intensity magnitude and yielding errors in the direction as frequency increases, even when well below the spatial Nyquist limit. However, the phase and amplitude gradient estimator (PAGE)²⁴ method developed recently at Brigham Young University generally yields more accurate intensity estimates over a broader frequency range. Applied to the F-22 intensity estimations, the PAGE method extends the useable frequency limit from about 2

kHz to roughly 6 kHz. The PAGE method is used to produce the vector maps below (excepting Fig. 2-4, which is included to demonstrate the advantages of the PAGE method).

2.2 Tetrahedral intensity probe

This tetrahedral intensity probe design was developed for the rocket motor studies described in Ref. 9 and 10 (see Fig. 1-2(b)). The external frame held four low-sensitivity GRAS 40BD prepolarized microphones with 26CB preamplifiers at the tetrahedron vertices, facing inward. The microphone diaphragms were positioned such that they could be circumscribed by a 1-1/2" diameter sphere. Laboratory testing of this probe configuration in anechoic conditions up to 2 kHz showed <1 dB maximum error in magnitude and <10° direction error.³⁰ The intensity probe was placed at approximately 2.54 m above the ground for the subset of the data presented in this thesis. Figure 2-1 details the orientation of the probe microphones.

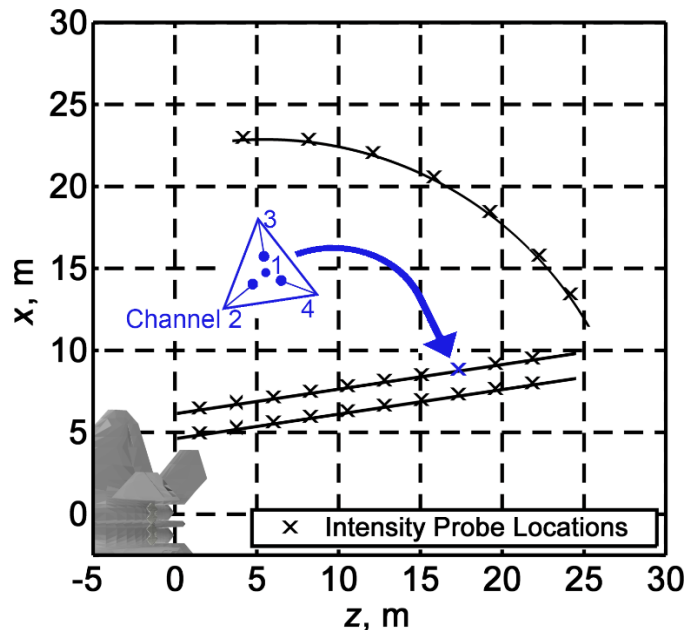


Figure 2-1. Top-down schematic of intensity probe data locations along the measurement planes and arc, (black). A schematic of the probe microphone orientation indicating channel number is superimposed, not to scale, (blue). Compare with Fig. 1-2.

To illustrate the functionality of the intensity probe, recorded sample waveforms on all four microphones are shown below in Fig. 2-2, for two different measurement locations. Differences in the signal's apparent time of arrival at each microphone are visible, especially at the pressure increases that occur just before 1 ms in the time records. Near $z = 8$ m downstream, channel 4 received information well before channel 3, but this order is reversed near $z = 17$ m downstream. This ordering makes intuitive sense in light of the probe orientation detailed in Fig. 2-1, and assuming a peak source location near 5-6 m downstream. In the time domain, time of arrival analysis can estimate the apparent direction of signal propagation, or the overall intensity vector direction, not unlike beamforming¹⁹ or phase speed characterizations²⁰. In the frequency domain, this time of arrival difference presents itself as differences in the complex pressures themselves, resulting in a nonzero imaginary part of the cross spectrum between microphone pairs. Traditional intensity estimation analysis finds that the imaginary part of the cross spectrum is directly proportional to the magnitude of the intensity component collinear with each microphone pair. In addition, time-of-arrival information is found in the phase of the transfer function between microphone pairs. The transfer functions between all four microphones may then be used (instead of the cross spectrum) to estimate the vector acoustic intensity as a function of frequency according to the new intensity estimation technique described below.

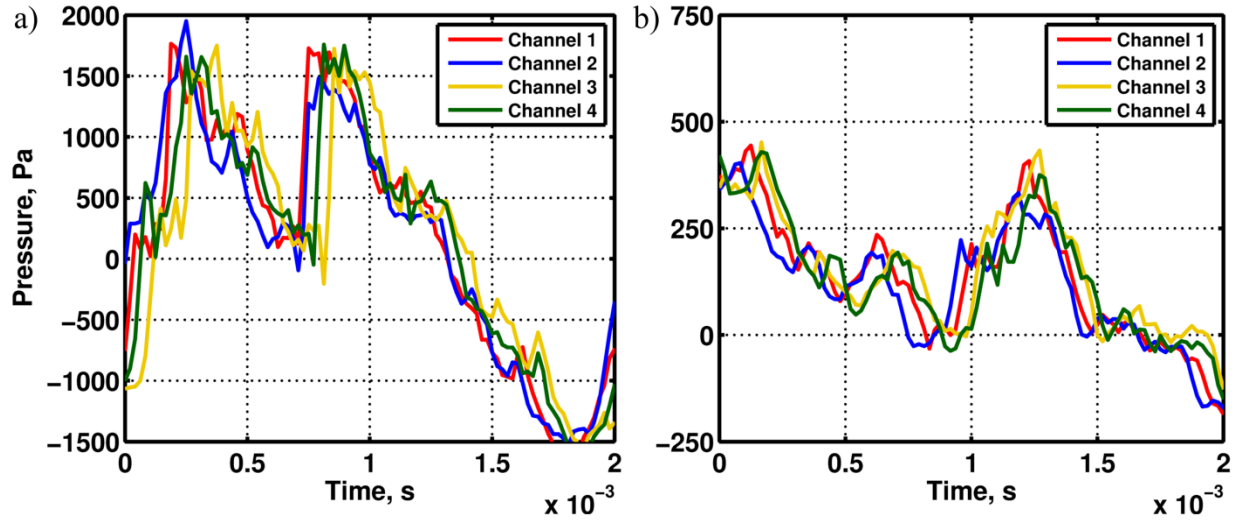


Figure 2-2. Waveforms as recorded by the four intensity probe microphones at two different locations, near $z = 8$ meters (a), and near $z = 17$ m downstream (b). Note the apparent arrival time at each microphone differs between the two locations.

2.3 PAGE methodology

Both FD and PAGE methods find the particle velocity by estimating the spatial gradient of the pressure and applying the Euler's equation,

$$j\omega\rho_0\mathbf{u} = -\nabla p,$$

where j is the unit imaginary number, ω is the angular frequency, ρ_0 is the ambient density, \mathbf{u} is the frequency-dependent (complex) vector particle velocity, and ∇p is the gradient of the complex pressure. The particle velocity is found by rearranging and integrating over a suitable averaging time.

In one dimension, with two microphones (A and B), the FD method uses a direct linear fit to calculate the pressure gradient as

$$(\nabla p)_x \approx \frac{p_B - p_A}{d_{AB}},$$

where d_{AB} is the distance between the two microphones. The pressure is approximated as the average value across the two microphones. In the frequency domain, the commonly used method for calculating acoustic vector intensity is based on the imaginary part of the cross spectrum. The single-sided active intensity is calculated as

$$I_{x,FD}(\omega) = \frac{-1}{\omega \rho_0 d_{AB}} \text{Im}\{S_{AB}(\omega)\},$$

where S_{AB} is the single-sided, time-averaged cross-spectrum between the two microphones, a function of angular frequency.

The PAGE method instead splits the complex pressure into amplitude and phase components, P and φ , respectively, as $p = P e^{-j\varphi}$. The gradient of the pressure is found to be

$$\nabla p = (\nabla P - jP \nabla \varphi) e^{-j\varphi},$$

and the active intensity is calculated as

$$\mathbf{I} = \frac{1}{\omega \rho_0} P^2 \nabla \varphi,$$

which in one dimension, with two microphones, is simplified to the estimate

$$I_{x,\text{PAGE}} = \frac{\varphi_B - \varphi_A}{\omega\rho_0 d_{AB}} \left(\frac{|P_A| + |P_B|}{2} \right)^2 = -\frac{\arg\{H_{AB}\}}{\omega\rho_0 d_{AB}} \left(\frac{|P_A| + |P_B|}{2} \right)^2,$$

where H_{AB} is the time-averaged transfer function between the two microphones, and $|P_A|$ and $|P_B|$ are the time-averaged complex pressure amplitudes. Details of this derivation are found in Ref. 24.

The above formulation estimates the active intensity in one dimension, at a point centered between two microphones, and collinear with the axis connecting the two microphones. To calculate the intensity in three dimensions using a tetrahedral intensity probe (such as that used in the F-22 measurements), the intensity components between the four microphones must be weighted and summed. Using an extension of the finite-difference method, the three-dimensional intensity can be found by weighting and summing the cross-spectra between the four microphones according to a least-squares method developed by Pascal and Li³¹ and recently implemented by Wiederhold *et al.*³² This process is mathematically equivalent for the PAGE method in three dimensions, except that the transfer function phases are weighted and summed instead of the cross spectra.

2.4 Performance of PAGE vs FD

In general, acoustic intensity estimates based on averaging the phase and amplitude differences, as in the PAGE method, are more stable and provide more accurate results over a

larger range of frequencies than use of the complex pressure average inherent in the imaginary part of the cross spectrum, $\text{Im}\{S_{AB}(\omega)\}$, used in FD estimation. The FD pressure gradient estimation (found from the imaginary part of the cross spectrum) inaccurately estimates intensity vector directions and underestimates the intensity magnitude even well below the spatial Nyquist limit, where the wavelength of the incident pressure wave is twice the probe separation distance. At just half the Nyquist frequency, this systematic error in estimated intensity magnitude approaches 2 dB for a plane progressive wave.²⁹ However, the PAGE method removes this upper limit, providing accurate estimates wherever the transfer function H_{AB} is well-behaved, within hardware limitations.

The magnitudes of the F-22 intensity estimates using FD and PAGE methods can be compared to the sound pressure levels as a benchmark for accuracy. In a traveling wave, the sound intensity level (SIL) and sound pressure level (SPL) are by definition approximately equivalent in dB. Above 100 Hz and for the data locations in the F-22 measurement, the intensity is expected to be dominated by the propagating acoustic wave; thus, the SIL and SPL are expected to be approximately equal as a function of frequency. The points at which the estimated SIL and the measured SPL diverge indicate the upper limit of the usable frequency bandwidth for accurate intensity estimation by each method. Figure 2-3 shows the SIL from the PAGE and FD methods versus SPL, averaged over the four intensity probe microphones, at one location along measurement plane 2. The FD results begin to diverge starting at about 2 kHz, while the SIL from the PAGE results follow the SPL until about 8 kHz. The spacing between microphones on the intensity probe corresponds to a spatial Nyquist frequency of about 5 kHz, so this amplitude-based measure of performance largely follows and confirms theoretical prediction. The slight disagreement between SIL from both methods and the measured SPL near 100 Hz is likely due to

error in the phase calibrations between the probe microphones. For this figure and all successive results, the SIL is referenced to one picowatt per square meter (10^{-12} W/m²).

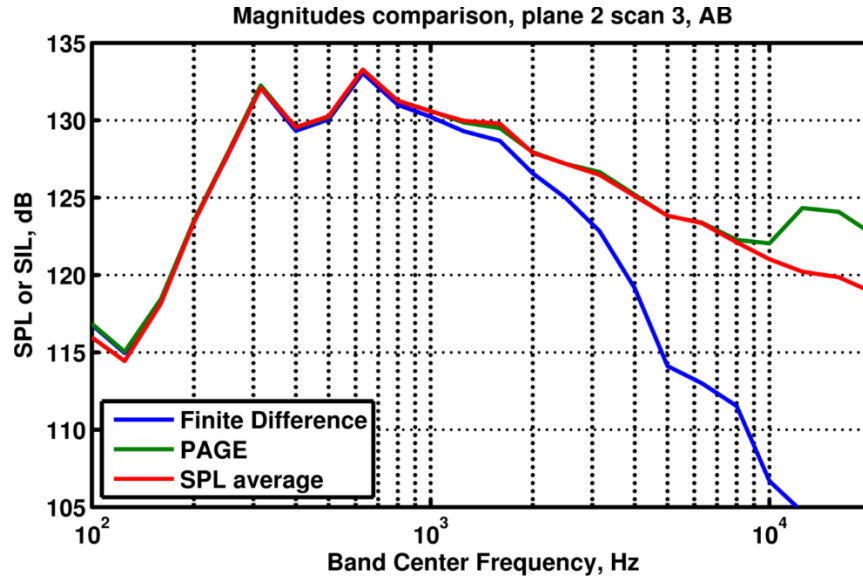


Figure 2-3. One-third octave sound pressure levels (SPL) averaged over the four intensity microphones, compared with the sound intensity levels (SIL) estimated using the finite difference (FD) and the PAGE method. The FD method underpredicts the intensity level beginning at 1 kHz, while the PAGE method SIL matches the SPL up to about 8 kHz. The disagreement between both SIL estimates and measured SPL near 100 Hz is likely due to error in the relative phase calibration between the four microphones on the intensity probe.

To directly demonstrate the advantage of the PAGE method over FD, example acoustic vector intensity maps of the F-22 sound field for 1.25 and 5.0 kHz at afterburner are shown in Fig. 2-4, estimated using both methods. A more complete collection of intensity vector maps using the PAGE method is given in Sec. 2.5. Both methods provide the same results at 1.25 kHz, well below the spatial Nyquist frequency of the intensity probe. However, at 5 kHz, the vectors given by the

FD method are clearly nonphysical, and significantly underpredict the intensity magnitudes given by the PAGE method.

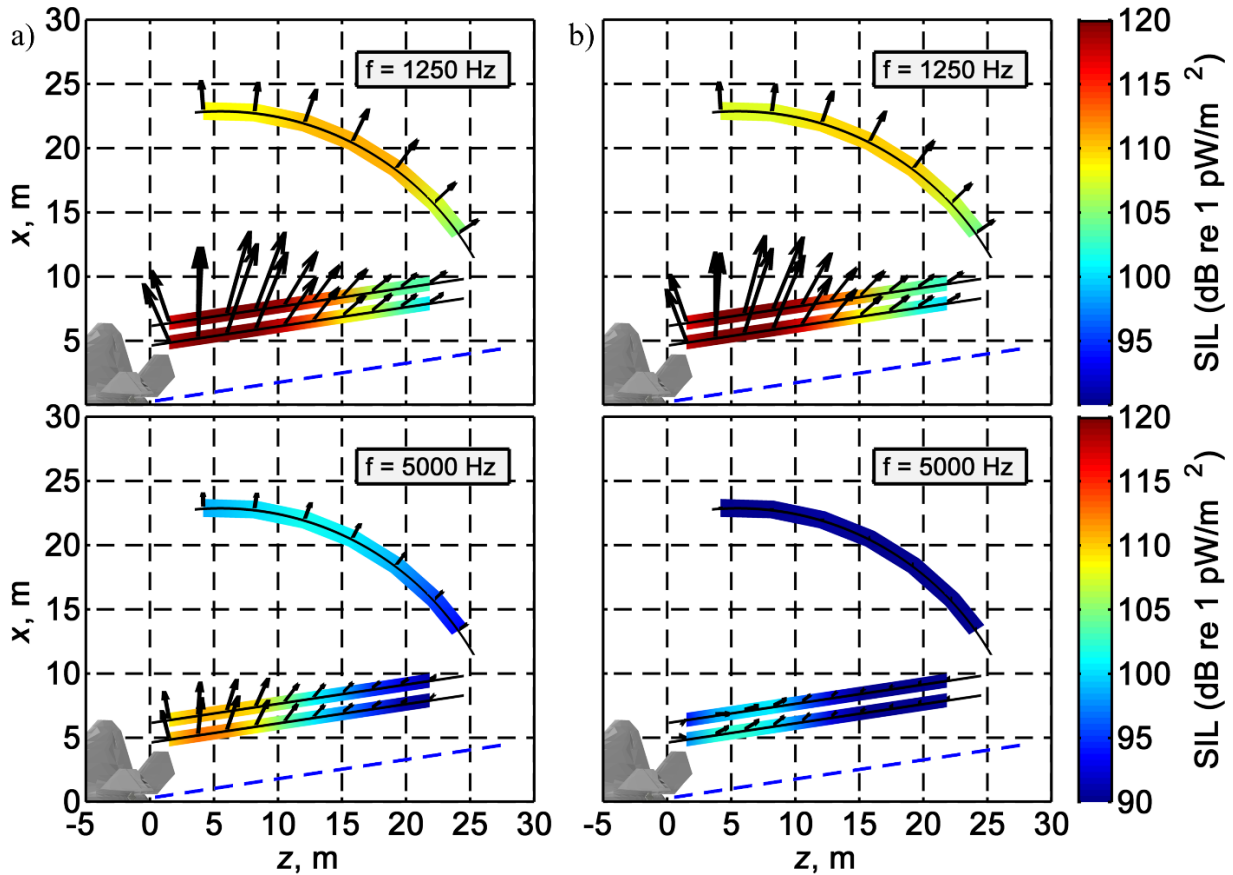


Figure 2-4. Acoustic vector intensity maps of the F-22 sound field at 1250 (top) and 5000 Hz (bottom) at afterburner, estimated using the PAGE method (a, left) and the FD method (b, right). The estimated shear layer of the jet exhaust is indicated by a blue dashed line. Though both methods agree at 1.25 kHz, for 5 kHz the PAGE method gives physically reasonable intensity directions and magnitudes, while the vector directions predicted by the FD method are clearly nonphysical, and the magnitudes are much lower compared to PAGE estimations.

2.5 Vector intensity maps

Estimated intensity vectors at one-third-octave band center frequencies of 125, 160, 200, 250, 315, and 500 Hz are shown in Fig. 2-5 at afterburner, and in Fig. 2-7 for military engine conditions. Higher-frequency results at 800 Hz, and 1.25, 2.5, and 5.0 kHz are shown in Figs. 2-6 and 2-8. The PAGE method is used for these calculations, so that accurate results above 2 kHz are possible. Only the horizontal (x - z) intensity components are displayed. For Figs. 2-5 and 2-7, and Figs. 2-6 and 2-8, respectively, linear internal scaling used by the rendering program to define vector lengths is kept consistent for comparison purposes. The lengths of the intensity vectors are cube-root scaled for purposes of illustration. The actual sound intensity levels (SIL) are indicated by the color bars and include energy within the 5.9 Hz frequency bin used in the calculation. The data were time-averaged over the full length of each static engine firing, about 25 seconds.

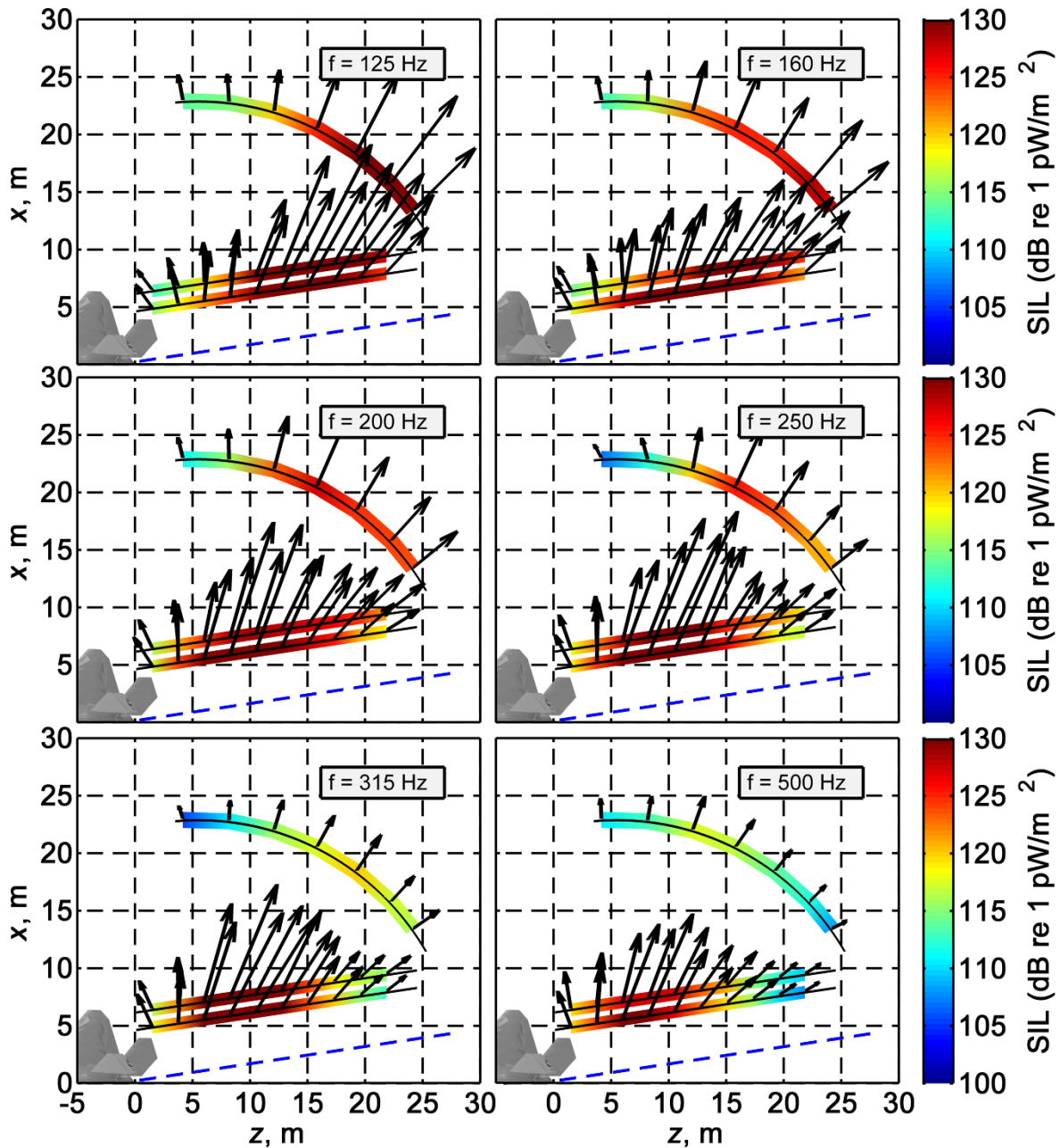


Figure 2-5. Acoustic intensity at afterburner engine conditions for select one-third octave band center frequencies. The intensity probe was located at the base of each vector arrow. The estimated shear layer is indicated by a blue dashed line. Vector length scaling used by the rendering program is kept consistent between this figure and Fig. 2-7. Note how the region of maximum intensity shifts upstream with increasing frequency, while the overall sound intensity level decreases. Maximum intensity magnitude levels are higher at afterburner than at military engine conditions by up to 5 dB.

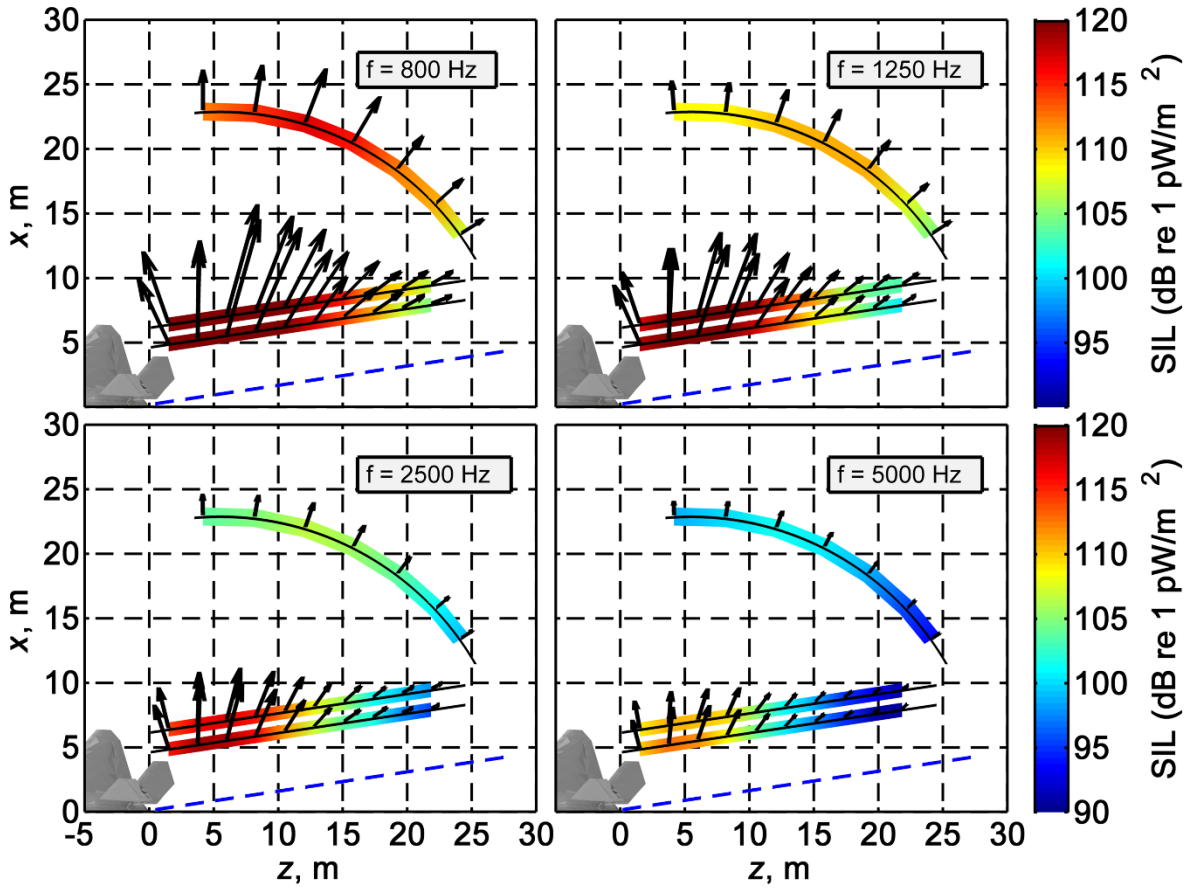


Figure 2-6. Acoustic intensity at afterburner engine conditions for select one-third octave band center frequencies. The intensity probe was located at the base of each vector arrow. The estimated shear layer is indicated by a blue dashed line. Vector length scaling used by the rendering program is kept consistent between this figure and Fig. 2-8. Note how the maximum intensity region location is generally consistent at these frequencies, while the overall sound intensity level decreases at higher frequencies.

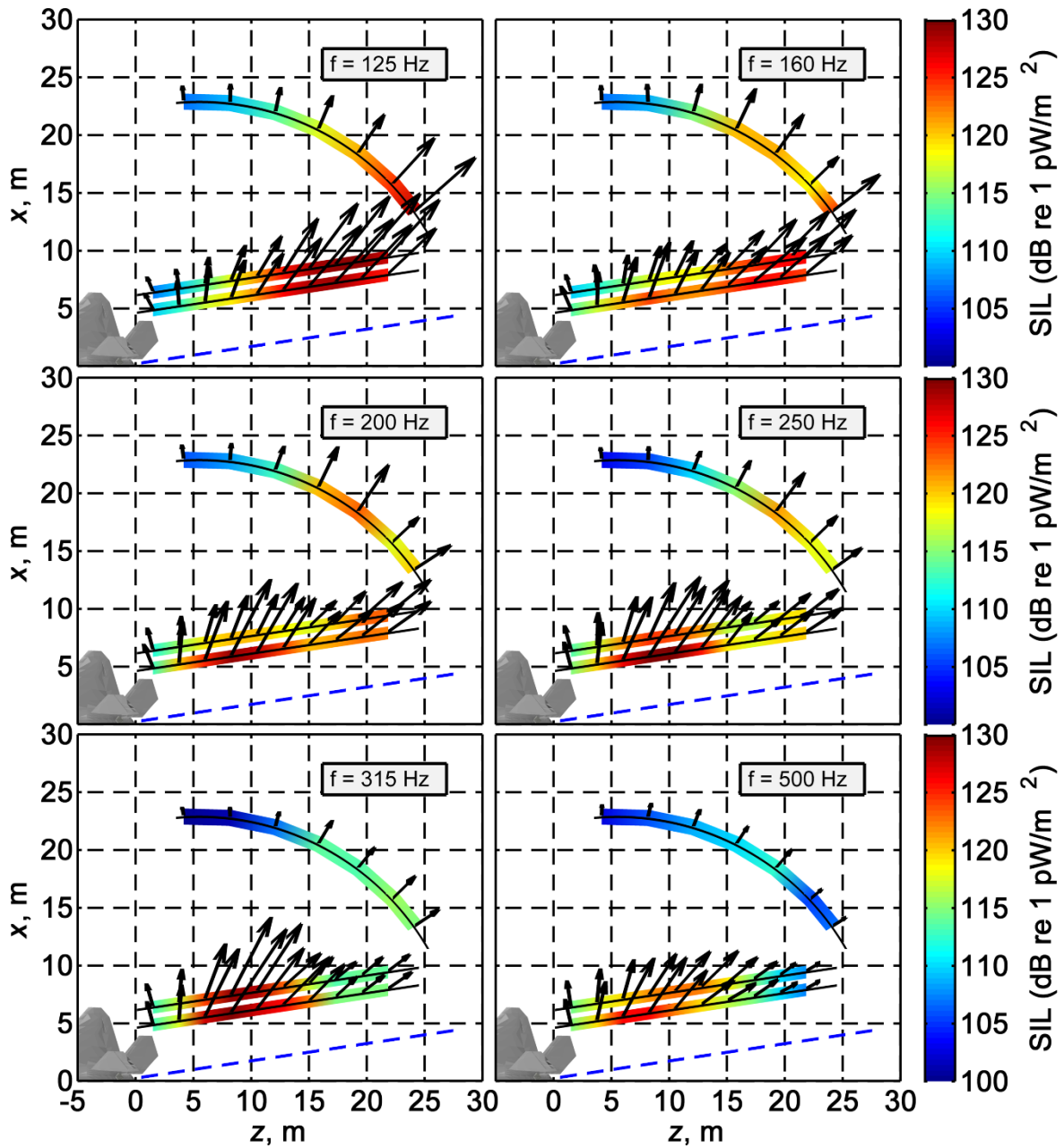


Figure 2-7. Similar to Fig. 2-5 except at military power. Vector scaling is kept consistent between this figure and Fig. 2-5.

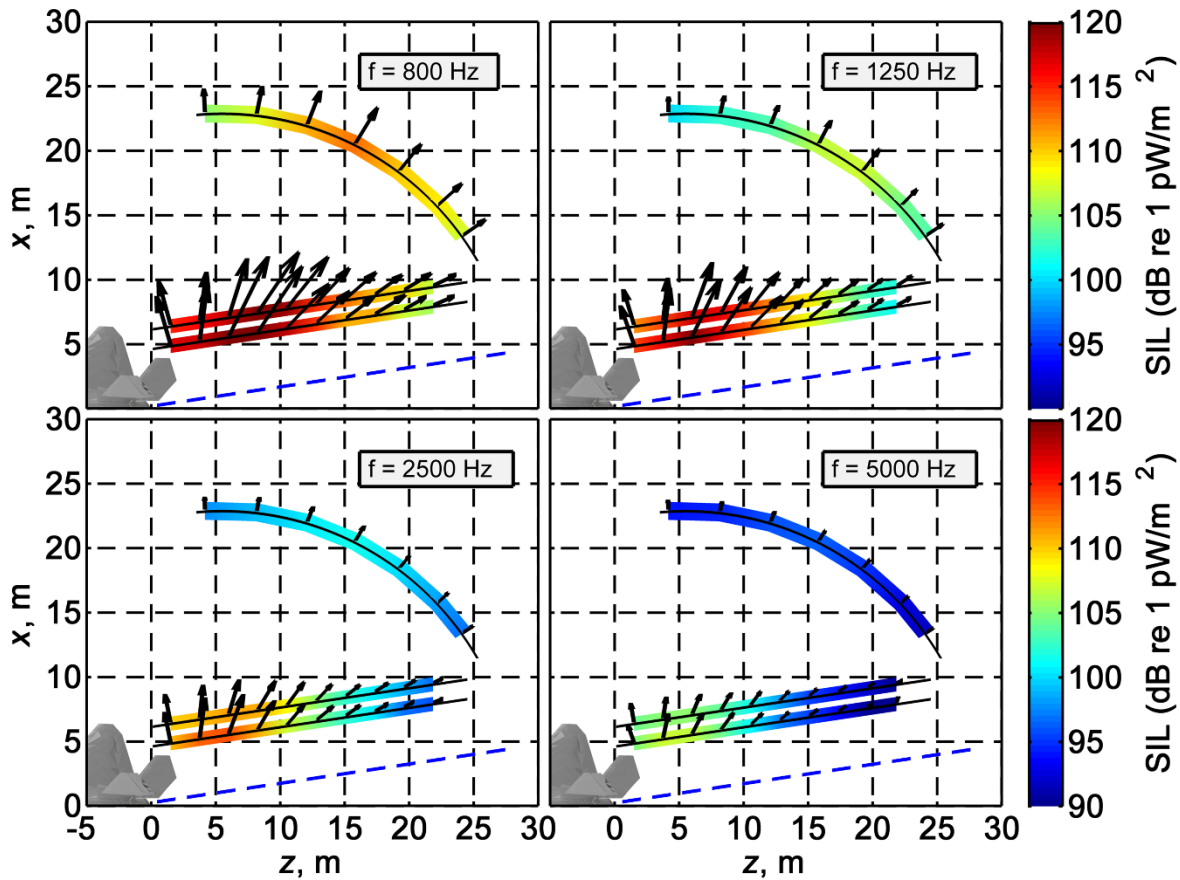


Figure 2-8. Similar to Fig. 2-6 except at military power. Vector scaling is kept consistent between this figure and 2-6. Maximum intensity magnitude levels are lower at military than at afterburner engine conditions by up to 5-7 dB.

Study of the intensity vector estimates in Figs. 2-5 to 2-8 elucidates the frequency-dependent nature of the F-22 sound field. The region of maximum intensity moves upstream with increasing frequency up to about 800 Hz, above which the location of the maximum intensity region stays fairly consistent, while the overall intensity magnitude decreases as expected from a typical jet noise power spectrum. The largest magnitude intensity vectors are unidirectional at low frequencies. For example, compare the smaller directional variation in the largest intensity vectors at 125 Hz (near $z = 20$ m), to the wider spread of vector directions at 1250 Hz, with maximum intensity near $z = 5$ m. At the higher frequencies, the rapid change in the vector directions as the

probe position goes from zero to 10 m downstream suggests an omnidirectional source component close to the nozzle, which becomes more prominent as frequency increases.

Another interesting feature seen at some of the low frequencies is an apparent dual intensity maxima along the measurement plane. In Fig. 2-7 at 125 Hz, one region of maximum intensity is observed, centered near $z = 18$ m downstream along measurement planes 1 and 2. At 160 Hz, the intensity vectors remain large around $z = 18$ m but another group of intensity vectors rise in magnitude, near $z = 8$ m that point in a different direction than those farther downstream. By 200 Hz, the vectors in the second region ($z = 8$ m) have increased in magnitude over the region farther downstream, and continue to increase somewhat at 250 Hz. Similar behavior is observed for afterburner in Fig. 2-5. This 125 - 250 Hz band corresponds to the same frequency region over which there is a dual peak in the spectral shapes, as identified by Neilsen *et al.*^{21-22, 33} and further investigated by Tam and Parrish.³⁴ Acoustical holography results¹⁸ show two prominent lobes of radiation at these frequencies, with low coherence between the lobes, giving further credence to the presence of independent source mechanisms (also, see Chapter 3). In addition, an intensity-based equivalent source model using two analytical, mutually incoherent steered line array sources has produced features consistent with these measurements, with greater success than the use of a single steered line array.¹³

Some initial qualitative comparisons between engine conditions can be made from the intensity maps. At all frequencies, the maximum intensity magnitudes at afterburner exceed those at military by up to 5-7 dB, and maximum intensity vectors at afterburner can be observed to point slightly farther to the fore. From 125-160 Hz, more sound energy is shifted downstream at afterburner than at military. These observations are quantified below in Sec. 2.6.

The presence of ground reflections from the concrete pad and rain-packed dirt has a noticeable effect on the acoustic vector intensity. At 125 Hz, as seen in Figs. 2-5 and 2-7, intensity vectors in the maximum intensity region along measurement plane 2 near $z = 20$ m have magnitudes about 1.5 dB higher than those along plane 1. This is contrary to expectation based on geometric spreading and is due to the interference of direct and reflected signals. For example, the intensity from a monopole at $z = 10$ m along the jet axis, with the same measurement geometry, produces constructive interference resulting in a relative + 2dB magnitude near $z = 20$ m along plane 2. The presence of ground reflection interference is readily observed in planar measurements from the 90-microphone array.²³

2.6 Analysis

2.6.1 Maximum intensity directions

The intensity maps shown above clearly illustrate the presence of a spatially extended source, with frequency-dependent characteristics. To better describe the most dominant portion of the sound field, at each frequency, a “3 dB-down” region is defined to include all intensity vectors with magnitudes within 3 dB of the maximum at that frequency. The source characterization in this section is based on analysis of these 3 dB-down regions along measurement plane 2 only.

Figure 2-9 displays the range of angles corresponding to intensity vectors contained within the 3 dB-down regions as a function of frequency. Specifically, the results are shown at one-third octave band center frequencies, but narrowband intensity vectors have been integrated over the one-third octave band. Key features of the sound field are illustrated here that have ties to source features. First, the variability of the vector directions increases with increasing frequency, most

notably at frequencies approaching 1 kHz. Below this frequency, the energy flow is much more unidirectional, indicative of the dominance of a directional, low-frequency source. At higher frequencies, a more omnidirectional source appears to rise in prominence. This rather rapid change in directionality at high frequencies is reminiscent of the Tam two-source model,³⁵ where noise at the sideline is dominated by high-characteristic-frequency, omnidirectional radiators due to fine-scale turbulence, whereas the unidirectional downstream noise is the result of large-scale turbulent structures with lower characteristic frequencies. It is perhaps not coincidental that the 1 kHz frequency transition in behavior is similar to the 1-2 kHz peak frequencies of the fine-scale similarity spectra used by Neilsen *et al.*²¹ to match the measured spectra at the sideline.

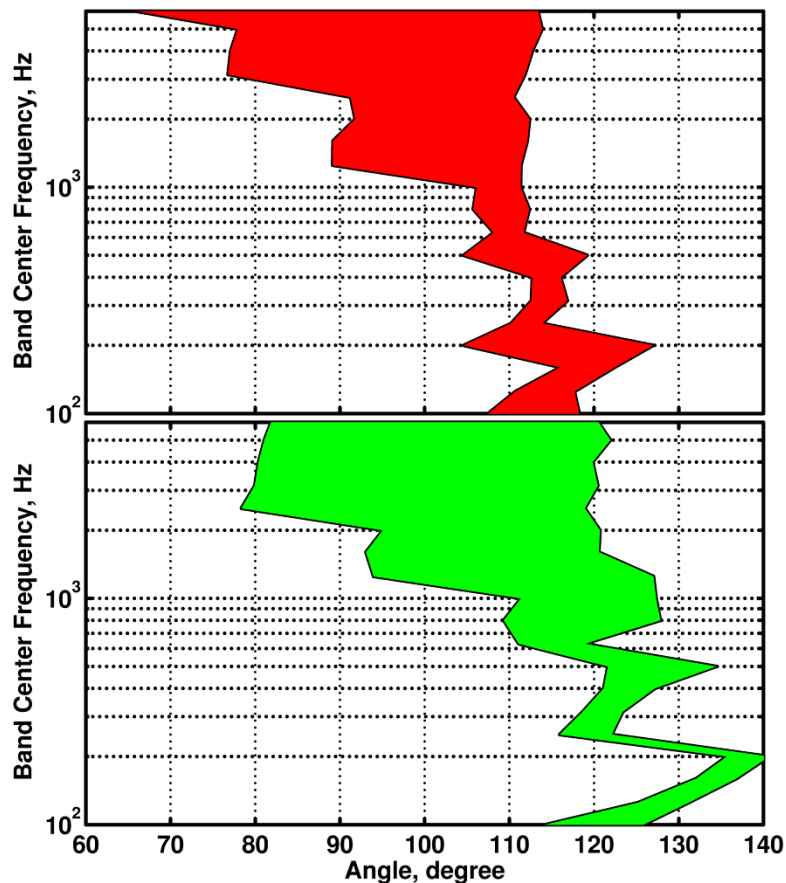


Figure 2-9. Angular span of the acoustic intensity vectors contained within the 3dB-down regions along plane 2 at one-third octave band center frequencies, after intensity vectors are integrated over one-third octave

bands, at afterburner (top) and for military engine conditions (bottom). Angles are measured from the engine inlet. For both conditions, the range of vector directions increases in width for frequencies about 1000 Hz for afterburner and 600 Hz for military, indicating the prominence of a more omnidirectional source. The rapid change at 200-250 Hz is an effect of the transition between two maximum intensity locations with discrete directionalities in that frequency range and is more apparent at military engine conditions. The forward shift at 100 Hz may be due to error in phase calibration within the intensity probe. Also, note how angles at afterburner are up to 10° farther forward than for military conditions.

Though the general trend is for the maximum intensity vectors to shift forward 10-15° as frequency increases, large variations in their direction are evident before 1 kHz, most notably for military engine conditions. A study of the vector maps in Figs. 2-5 and 2-7 explains the rapid transition between directions around 200 Hz. As noted above, between about 160-250 Hz, two discrete regions of maximum intensity are evident at measurement planes 1 and 2, which shift in prominence. Note how the most pronounced vector directions differ between these two regions; thus, the vector directions corresponding to vectors that are within 3 dB-down of the maximum one at each frequency, along plane 2, shift discretely between 160-250 Hz. This effect is most notable at military engine conditions; the directions shift from 135-140° at 200 Hz to 117-122° in the 250 Hz third-octave band. Comparison with Fig. 2-7 at 200 and 250 Hz (along measurement plane 2) illustrates directly the shift in prominence between the 3 dB-down region centered around $z = 20$ m downstream, to a region centered around $z = 10$ m, with these differing directionalities.

In addition, there is an abrupt difference in the direction of the largest intensity vectors at 100 Hz compared to those at 125 Hz. Such an upstream shift in direction as frequency decreases is not expected. Thus, the 100 Hz vector directions of 110° and 120° at afterburner and military, respectively, are likely due to error in the relative phase calibrations between probe microphones, which introduces error in vector intensity estimation at low frequencies. As evidence of this, the

SPL values averaged over the microphones differs slightly from the SIL estimate at 100 Hz (see Fig. 2-3). Furthermore, at 100 Hz, intensity reconstructions from near-field acoustical holography using data from the 90-microphone rig (see Chapter 3) predicts intensity vectors which point farther downstream from these estimations by about 10° .

Comparisons can be drawn between the vector directions in the 3-dB down regions at afterburner, and the measured far-field directivity of the F-22. The directivity of the F-22 at afterburner was previously measured with 10 degree resolution between $115\text{-}145^\circ$ at distances of 61 m and 305 m.³⁶ At 100-160 Hz, radiation from the F-22 was most prominent between $125\text{-}135^\circ$, while at or above 200 Hz, a measured directivity of 115° dominated (the measurements did not extend farther forward). The maximum OASPL directivity angle was 125° .²³ The vector directions in Fig. 2-9, however, show dominant radiation at $105\text{-}125^\circ$ from 100-200 Hz, then $105\text{-}120^\circ$ between 200-1000 Hz, and even farther forward above 1000 Hz. Thus, it is likely important to consider that directions farther forward than the maximum far-field directivity angle become prominent above about 200 Hz in geometric near- and mid-field energy flow. The calculated intensity vectors in the 3 dB-down regions only align with the maximum directivity angle for the 200 Hz one-third octave band. As noted above, though, calculated intensity angles at or below 160 Hz were likely influenced by errors in the relative phase calibration.

The most notable difference between the two engine conditions is that the intensity vector angles at afterburner are directed up to ten degrees farther forward on average than for military engine conditions. For example, at 1 kHz, the vectors at afterburner point at $98\text{-}112^\circ$ relative to the engine inlet, but at $112\text{-}122^\circ$ for military power. The difference is evident across all frequencies. In addition, the vector directions at military are more unidirectional up to about 600 Hz, shifting to a more omnidirectional trend thereafter; interestingly, this shift occurs closer to 1

kHz at afterburner. The delay in omnidirectionality at afterburner may be explained by further reference to the similarity spectra analysis by Neilsen *et al.*²¹ according to the Tam two-source model, as a function of engine condition. At a look direction of 90°, for military engine conditions, the contributions from both similarity spectra needed to match the measured spectrum are approximately equal by about 600-800 Hz, with the more omnidirectional fine-scale structures dominating at higher frequencies. At afterburner, and again at a 90° look direction, a similar mixed spectrum is shown, but the crossing point of the two similarity spectra occurs instead at 1 kHz. For locations where a combination of both similarity spectra is needed to match the measured spectra, frequencies at which the fine-scale contribution exceeds the large-scale correspond to the shifts towards omnidirectionality shown in Fig. 2-9.

2.6.2 Ray-tracing

As a straightforward method to approximate the frequency-dependent source region, intensity vectors along measurement plane 2, located 5.6 m to the side of the shear layer, are traced back to the jet centerline. This technique is prompted by the methods of Jaeger and Allen⁸ in studying subsonic jets and has been applied previously to a 12.7 cm-diameter and 1.1 m-diameter rocket motor.³⁰ Narrowband intensity calculations are integrated within a given one-third-octave band, and a 3 dB-down region is defined from the resultant intensity vectors, representing the dominant energy in that band. Vectors in the region are traced backwards, so that the left-most and right-most intercepts along the jet centerline define an approximate equivalent noise source location and indicate the extent of the source. Similar results up to 3 kHz, using intensity calculated with the finite-difference method, have been reported previously at narrowband frequencies only.³⁷

The equivalent source reconstruction results from 80 Hz to 6 kHz are shown in Fig. 2-10. For both military and afterburner conditions, the ray-traced peak source location moves upstream and its extent contracts with increasing frequency. The comparison between the estimated source regions for the two engine powers shows that above about 300 Hz, the source region for afterburner is about 1 m farther downstream than at military power, and is somewhat broader by up to 1 m in width above 200 Hz. As expected from comparison with jets of other scales, the extended source region shown in Fig. 2-10 is more compact than the source region found in a higher-thrust jet plume such as that emanating from a GEM-60 solid rocket motor¹⁰ and is more extended spatially than a subsonic, unheated jet⁸.

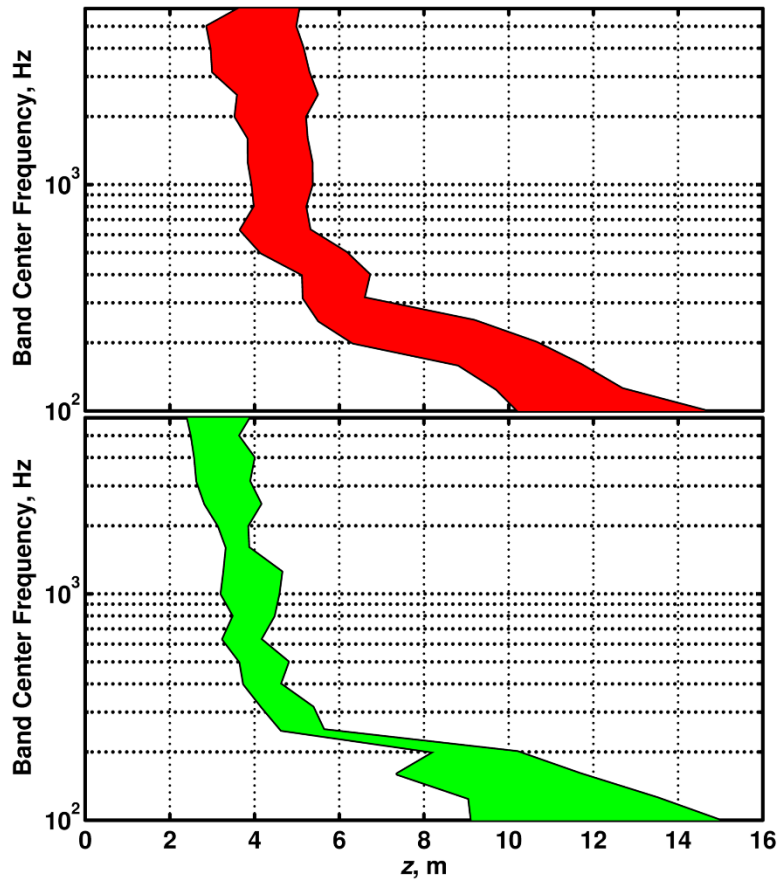


Figure 2-10. Generalized equivalent source locations as a function of frequency found from intensity ray-tracing, at afterburner (top) and military engine conditions (bottom). Ray-tracing results are presented at one-third octave band center frequencies, from intensity vectors integrated over each band. The rapid transition region around 200 Hz corresponds to the switch in dominant intensity regions seen in Figs. 2-5 and 2-7, and is more apparent at military engine conditions. At all frequencies, results at afterburner are about 1 m farther downstream than for military.

Though the ray-tracing method from intensity estimates requires much simpler processing compared with other techniques such as beamforming or holography, quantitatively similar results are obtained for the full-scale F-22 sound field. Beamforming^{20, 38-40} and holography¹⁶⁻¹⁸ also indicate that the extended source region from full- and lab-scale jets contracts and moves upstream

with increasing frequency. Some equivalent source models such as wavepackets^{41, 42} predict the same trend in source behavior.

Although the frequency-dependent estimated source location trend in Fig. 2-10 agrees with previous studies on laboratory-scale jet noise, the transition in source location at low frequency (from 100 to 400 Hz) for the F-22 occurs more rapidly than similar transition regions in laboratory-scale jets. From beamforming analysis, Lee and Bridges found that the transition in source location occurred more smoothly over a broader frequency range in a subsonic, heated jet.³⁸ Increasing the acoustic Mach number caused a sharper transition above a Strouhal number (St) of 0.5. However, the frequency range of the transition was well above the dominant radiation frequencies (from $St = 0.1 - 0.2$). By contrast, the transition region in Fig. 2-10 occurs around the dominant frequencies of the noise from the F-22, about 100-200 Hz in the peak radiation direction.

The significant shift in the locations of the estimated F-22 source region between 100 and 250 Hz, Fig. 2-10, corresponds to the discrete change in maximum intensity regions seen in the vector maps in Figs. 2-5 and 2-7. Recall the presence of the two regions in different locations along measurement plane 2 with large intensity vectors that point in different directions. The 3 dB-down region location shifts between these two regions near 200 Hz, producing the abrupt change in ray-tracing results. This effect is most pronounced at military engine conditions, where the estimated source region covering $z = 9-15$ m at 200 Hz shifts upstream to $z = 4.5-5.5$ at 250 Hz, the next third-octave band. As noted above, the nature of this transition region and the possibility of two discrete source mechanisms are currently being explored (also see Appendix A).^{18, 21-22, 33-34}

2.6.3 Ray-tracing validation

To better evaluate the physical significance of the resulting ray-traced dominant source regions, a numerical case study has been created in which the intensity vectors from a numerically

propagated source are ray-traced back to the source region, similar to what has been done with the F-22 data. The analytical, axial source distribution chosen for the simulated source incorporates the hyperbolic tangent wavepacket model proposed by Papamoschou (see Chapter 4).⁴¹ Two line arrays of closely-spaced monopoles are placed along the jet axis, one at the height of the engine nozzle to simulate the direct source, and the other at the same distance below the ground to simulate the ground reflection. The amplitudes of the monopoles were spatially weighted according to the equation,

$$|p(z)| = \tanh \left[\left(\frac{z}{b_1} \right)^{g_1} \right] \left(1 - \tanh \left(\frac{z}{b_2} \right)^{g_2} \right).$$

where b_1 , b_2 , g_1 , and g_2 are input parameters. Two examples of wavepacket-based amplitude distributions are displayed in Fig. 2-11(b) for 100 Hz and Fig. 2-12(b) for 250 Hz. This amplitude envelope is then applied to the arrays of monopoles.

Intensity vectors are calculated from two amplitude-shaded line arrays of monopoles, one in which the monopoles are uncorrelated, and one in which the monopoles across the entire array are correlated and steered towards one physically-relevant direction. The two types of line sources are of interest because of the partially correlated nature of jet noise. Intensity vectors calculated with each line array are shown in Figs. 2-11(a) and 2-12(a) for 100 and 250 Hz, respectively, where scaling between the two cases is arbitrary. As with the F-22 data, a 3 dB-down region is defined that includes all vectors with magnitudes within 3 dB of the maximum magnitude vector for each source type. The vectors from this region are traced back to the centerline as above. The resulting range of z -intercepts for each source model are shown by shaded regions in Figs. 2-11(b) and 2-12(b).

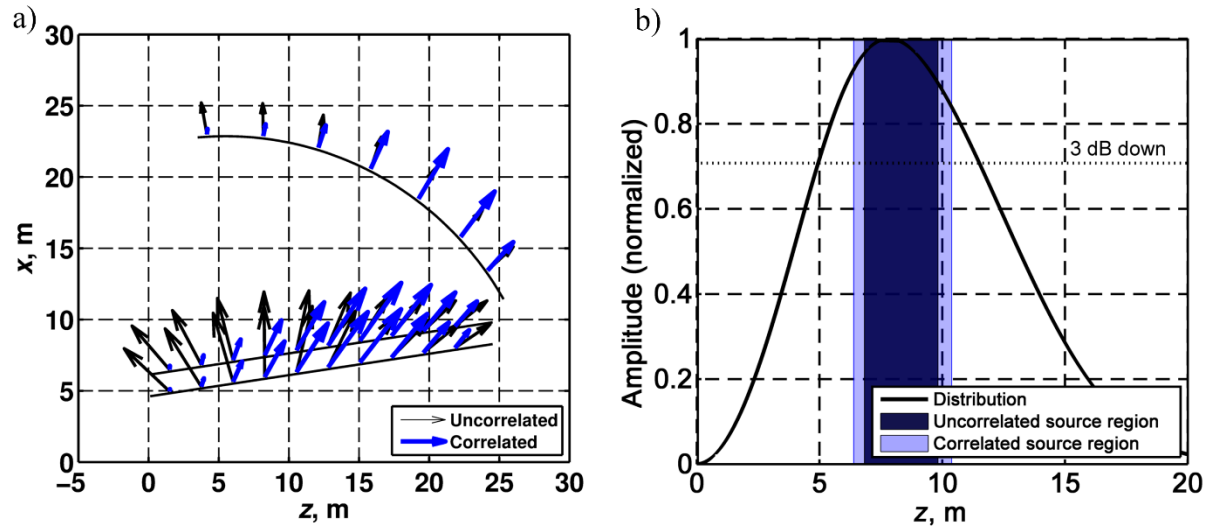


Figure 2-11. Simulated intensity fields at 100 Hz (a), resulting from either a correlated or uncorrelated array of amplitude-shaded monopoles, and ray-tracing results compared to the actual source distribution, (b). In (a), the black vectors represent the acoustic intensity from an uncorrelated distribution of monopoles, and the blue vectors show intensity from a correlated distribution. In (b), the solid black line shows the amplitude shading applied to the line array of monopoles for both cases. The dark blue bar indicates the ray-traced source width from the resultant 3 dB-down region in the uncorrelated case; the light blue indicates the same for the correlated case. A dotted line shows the amplitude that is 3 dB down from the maximum of the source distribution. Note how the ray-tracing method predicts a broader source extent in the correlated case, while approximately the top 1 dB of source energy is represented in the source predictions for both source models.

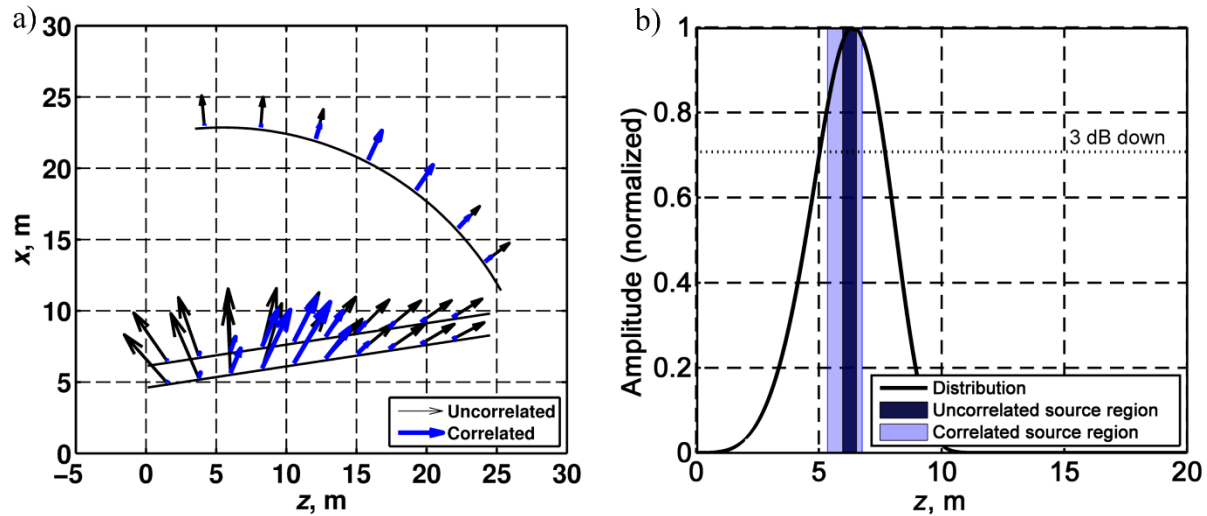


Figure 2-12. Similar to Fig. 2-11 except at 250 Hz.

In simulated results at both frequencies, the predicted source regions accurately capture the peak location, but only span about the top 10% of the pressure distribution, or the top 1 dB of the source energy. The source region width found for the correlated array exceeded that for the uncorrelated array somewhat, though the method performs similarly in both cases. Because jet noise sources are expected to exhibit both correlated and uncorrelated characteristics, with the correlated noise dominating at lower frequencies, this performance is encouraging. However, it should be stressed that ray-tracing results from the 3 dB-down regions in the intensity field will not translate directly to the location of the top 3 dB of the source region.

Chapter 3

Acoustical holography intensity reconstructions

Chapter 2 illustrates the utility of intensity measurements at discrete points near a complex acoustic source. Capturing both the direction and magnitude of sound energy flow allows for ray-tracing and characterization of source location and extent as a function of frequency. To expand on this analysis based on several discrete points, the full range of data is employed in this chapter, taken by the ground reference microphones as well as the 90-microphone array along the measurement planes near the F-22 (see Sec. 1.3). The large coverage of this measurement aperture allows for application of a holography method, which estimates the acoustic vector intensity anywhere in the three-dimensional volume around the jet, up to the shear layer. In addition, contributions from individual, mutually-incoherent sources are isolated by means of an optimized partial field decomposition. While not as straightforward as the method in Chapter 2, the analysis here provides further insight into the nature of the acoustic source and its sound field.

3.1 Introduction

Multiple analysis techniques have been employed to better understand the sound field near jet plumes, as well as infer source characteristics. Statistically-optimized near-field acoustical holography (SONAH)⁴³⁻⁴⁵ is one method which allows for three-dimensional reconstruction and visualization of the sound field. Applied to the jet sound field, SONAH reconstructions can characterize the sound source along the shear layer, as well as the near-field behavior and directivity. The SONAH algorithm is versatile, allowing for application to many different source geometries. For example, SONAH has been used in the analysis of a laboratory-scale jet, representing the sound field using cylindrical basis functions.⁴⁶ Using two sets of cylindrical basis functions to represent a direct and reflected source, SONAH has been applied to full-scale jet data as well.⁴⁷ Heretofore, applications to full-scale jet measurements have reconstructed only the pressure field near to the source and along the shear layer. However, SONAH can also be used to reconstruct the acoustic particle velocity field, so that the intensity field is found as well. This chapter describes the development of a SONAH algorithm for intensity reconstruction and its application to measurements in the near-field of the F-22A Raptor. The formulation of the algorithm, and the reconstructed intensity fields at nozzle height (1.9 m) in the geometric near and mid-fields are detailed in Sections 3.2-3.4. In Section 3.5, SONAH intensity reconstructions at the intensity probe locations are compared with the intensity vectors calculated from the probe as benchmark measurements.

3.2 Theoretical formulation

Like other array-based inverse methods, SONAH involves decomposition of the measured sound field into a linear combination of a set of spatial basis functions, or wave functions, which, when summed with the proper coefficients, reproduce the measurement. The wave functions chosen must obey the Helmholtz equation, i.e. the general homogeneous time-harmonic wave equation. The field is then reconstructed at a new location by summing the weighted wave function values there. SONAH offers an advantage over traditional near-field acoustical holography, because it does not involve a k-space decomposition. Instead, all processing is done spatially. The SONAH algorithm calculates a transfer function matrix between the hologram (measurement) locations and the reconstruction locations, then applies the matrix to the measured sound pressures.

Multiple wave functions can be included in the transfer function matrix, through a straightforward concatenation scheme.⁴⁸ Use of multiple wave function sets is called multisource-type representation SONAH (M-SONAH). In application to the F-22 sound field measurements, incorporation of two sets of cylindrical wave functions with M-SONAH has been shown to produce more accurate reconstructions than models which do not involve ground reflections⁴⁹ and planar NAH⁵⁰. This is because the aircraft was tethered to a highly-reflective concrete run-up pad, and planar wave functions do not incorporate the geometrical spreading of the sound field.

A detailed formulation of the M-SONAH algorithm used to reconstruct the pressure field is provided by Wall⁵¹ and summarized here, and the modifications necessary to reproduce the vector particle velocity field and hence the intensity field are described in this section. First, for a single frequency, a set of complex pressure wave functions, $\psi_n, n = 1, 2, \dots, N$, are chosen which correspond best to source geometries, or best describe known source geometries. The complex

pressures at the hologram locations and at the reconstruction locations will be expressed as linear combinations of these same wave functions. To do this, two matrices are formed, $\mathbf{A}(\mathbf{r}_h)$ and $\boldsymbol{\alpha}(\mathbf{r}_r)$, of the N wave functions evaluated at the measurement or hologram points, \mathbf{r}_h , and reconstruction locations, \mathbf{r}_r , respectively. These matrices are the inputs for the traditional SONAH algorithm,^{44,52}

$$\mathbf{p}(\mathbf{r}_r) \approx \mathbf{p}(\mathbf{r}_h)^T (\mathbf{A}^H \mathbf{A})^{-1} \mathbf{A}^H \boldsymbol{\alpha},$$

where $\mathbf{p}(\mathbf{r}_r)$ is the resultant vector of pressure estimates at the reconstruction locations, $\mathbf{p}(\mathbf{r}_h)^T$ is the transpose of the hologram measurements, and \mathbf{A}^H denotes the Hermitian transpose of the matrix \mathbf{A} . In essence, the algorithm defines a transfer function matrix,

$$\mathbf{a} = (\mathbf{A}^H \mathbf{A})^{-1} \mathbf{A}^H \boldsymbol{\alpha},$$

which represents the pressures at the reconstruction locations as a linear combination of the hologram measurements, that is,

$$\mathbf{p}(\mathbf{r}_r) \approx \mathbf{p}(\mathbf{r}_h)^T \mathbf{a}.$$

Like \mathbf{A} and $\boldsymbol{\alpha}$, \mathbf{a} is dependent only on the choice of wave functions and the geometry of the problem, so that once it is defined the transfer function matrix may be used with any set of measured data $\mathbf{p}(\mathbf{r}_h)$ to compute reconstructed pressures.

To account for spatial noise in $\mathbf{p}(\mathbf{r}_h)^T$ caused by variability in microphone placement and other factors, the inverse of $\mathbf{A}^H \mathbf{A}$ is typically regularized in the above expressions. The necessity for inversion comes about from the expression of the hologram measurements as a linear combination of the wavefunctions,

$$\mathbf{c}^T \mathbf{A} = \mathbf{p}(\mathbf{r}_h)^T,$$

with least-norm solution for \mathbf{c} ,

$$\mathbf{c}^T = \mathbf{p}(\mathbf{r}_h)^T (\mathbf{A}^H \mathbf{A})^{-1} \mathbf{A}^H.$$

As described by Cho *et al.*⁴⁴ and Wall⁵¹, after a singular value decomposition giving,

$$\mathbf{A}^H \mathbf{A} = \mathbf{V} \mathbf{G} \mathbf{V}^H,$$

a modified Tikhonov filter, \mathbf{F}_1^α , may be used to obtain the regularized inverse of $\mathbf{A}^H \mathbf{A}$,

$$\mathbf{R}_{A^H A} = \mathbf{V}(\alpha(\mathbf{F}_1^\alpha) + \mathbf{G}^H \mathbf{G})^{-1} \mathbf{G}^H \mathbf{V}^H,$$

where \mathbf{F}_1^α is given by,

$$\mathbf{F}_1^\alpha = \text{diag} \left[\dots, \alpha / \left[\alpha + |\lambda_i|^2 \left(\frac{\alpha + |\lambda_i|^2}{\alpha} \right)^2 \right], \dots \right],$$

where α is a regularization parameter and λ_i is the i^{th} singular value found along the diagonal of \mathbf{G} . The regularization parameter α is found by minimizing the cost function,

$$J(\alpha) = \frac{\|\mathbf{F}_1^\alpha \mathbf{V}^H \mathbf{p}(\mathbf{r}_h)\|^2}{[\text{trace}(\mathbf{F}_1^\alpha)]^2}.$$

This filters out noise in the wavenumber domain. Including the regularized inverse, the complete SONAH algorithm computes the reconstructed pressures as,

$$\mathbf{p}(\mathbf{r}_r) \approx \mathbf{p}(\mathbf{r}_h)^T \mathbf{R}_{A^H A} \mathbf{A}^H \boldsymbol{\alpha}.$$

For M-SONAH, \mathbf{A} and $\boldsymbol{\alpha}$ are instead formed by vertically concatenating matrices for multiple sets of wave functions, one for each source, evaluated at the measurement and reconstruction locations, respectively. For two sets of wave functions,

$$\mathbf{A} = \begin{bmatrix} \mathbf{B}_1 \\ \mathbf{B}_2 \end{bmatrix}, \boldsymbol{\alpha} = \begin{bmatrix} \boldsymbol{\beta}_1 \\ \boldsymbol{\beta}_2 \end{bmatrix},$$

where \mathbf{B}_1 and $\boldsymbol{\beta}_1$ are the evaluations of the first set of wave functions, and \mathbf{B}_2 and $\boldsymbol{\beta}_2$ of the second set. The SONAH algorithm can then reconstruct the pressure field at the reconstruction locations.

To reconstruct vector particle velocity, $\boldsymbol{\alpha}$ is instead found by calculating the particle velocity wave function corresponding to the chosen pressure wave functions. The magnitude of one component of the wave function's particle velocity vector is then calculated at the

reconstruction locations. In cylindrical coordinates, the particle velocity wave function is evaluated in the r , φ , and z directions, and three matrices are formed,

$$\boldsymbol{\alpha}_r = \begin{bmatrix} \boldsymbol{\beta}_{r_1} \\ \boldsymbol{\beta}_{r_2} \end{bmatrix}, \boldsymbol{\alpha}_\varphi = \begin{bmatrix} \boldsymbol{\beta}_{\varphi_1} \\ \boldsymbol{\beta}_{\varphi_2} \end{bmatrix}, \boldsymbol{\alpha}_z = \begin{bmatrix} \boldsymbol{\beta}_{z_1} \\ \boldsymbol{\beta}_{z_2} \end{bmatrix},$$

where $\boldsymbol{\beta}_{r_1}$, $\boldsymbol{\beta}_{\varphi_1}$, and $\boldsymbol{\beta}_{z_1}$ are the components of the first set of particle velocity wave functions evaluated at the reconstruction locations, and $\boldsymbol{\beta}_{r_2}$, $\boldsymbol{\beta}_{\varphi_2}$, and $\boldsymbol{\beta}_{z_2}$ are the components of the second set. Often, it is computationally efficient to calculate each cylindrical wave function about individual central axes. If the two sets wave functions utilize a different origin or central axis, they must then be rotated so that they share a common axis. More precisely, a change of basis must be applied independently to the real and imaginary parts of either $\boldsymbol{\beta}_{r_1}$ and $\boldsymbol{\beta}_{\varphi_1}$, or to $\boldsymbol{\beta}_{r_2}$ and $\boldsymbol{\beta}_{\varphi_2}$, so that the two pairs of matrix components both reference the same z -axis. The concatenated matrices $\boldsymbol{\alpha}_r$, $\boldsymbol{\alpha}_\varphi$, and $\boldsymbol{\alpha}_z$ are then each input individually, along with the same matrix \mathbf{A} as above, into the SONAH algorithm to reconstruct the components of the particle velocity field. The three-dimensional active intensity vector field is found by appropriate multiplication with the reconstructed pressure field. For example, Hald⁴⁸ applied a one-dimensional Euler's equation to a pressure-based planar SONAH algorithm to find the corresponding particle velocity, and hence, the vector intensity in one direction.

For the present formulation, two sets of cylindrical wave functions were chosen, with central axes corresponding to the physical jet axis, and the image source axis, respectively. Elementary cylindrical wave functions at location (r, φ, z) are given by

$$\psi_{k_z, n}(r, \varphi, z) = \frac{H_n^{(1)}(k_r r)}{H_n^{(1)}(k_r r_s)} e^{in\varphi} e^{ik_z z}, r \geq r_0,$$

where $H_n^{(1)}$ is the n th-order Hankel function of the first kind, r_s is some small reference radius or assumed source radius. The radial wavenumber, k_r , is dependent on the axial wavenumber, k_z , and the wavenumber of interest, $k = \frac{\omega}{c}$, (where ω is the angular frequency and c is the ambient sound speed), by

$$k_r = \begin{cases} \sqrt{k^2 - k_z^2}, & |k| \geq |k_z|, \\ \sqrt{k_z^2 - k^2}, & |k| < |k_z|. \end{cases}$$

Using Hankel functions of order $n = 0$, the two sets of these wave functions are evaluated to form \mathbf{B}_1 and \mathbf{B}_2 , then concatenated into \mathbf{A} , and similarly to form $\boldsymbol{\alpha}$.

The corresponding three-dimensional particle velocity wave function is found to be⁵³,

$$\vec{V}_{k_z, n}(r, \varphi, z) = \frac{1}{\rho_0 c} \left(\frac{-i}{k} \frac{\partial}{\partial r} \hat{e}_r + \frac{n}{kr} \hat{e}_\varphi + \frac{k_z}{k} \hat{e}_z \right) \psi_{k_z, n}(r, \varphi, z),$$

and the r component is computed as,

$$\vec{V}_{k_z, n} \cdot \hat{e}_r = \frac{-ik_r}{\rho_0 c k} \psi_{k_z, n},$$

where ρ_0 is the ambient density. Two complete sets of these wave functions are used to form the matrices $\boldsymbol{\alpha}_r$, $\boldsymbol{\alpha}_\varphi$, and $\boldsymbol{\alpha}_z$.

3.3 OLVR Partial field decomposition

To better make sense of a complicated total field found from application of SONAH, a partial field decomposition may be applied to split the resultant field into orthogonal components. There are multiple decomposition methods which offer complete sets of orthogonal fields which include all the energy in the total field; this problem is not unique. For example, a traditional SVD-based decomposition produces results which are generally not physically meaningful, because the way the algorithm chooses partial fields is arbitrary, primarily influenced by the geometry of the

problem. Applied to the F-22 data along a measurement plane, the SVD-based partial fields resemble the modes of a string. On the other hand, a technique called the optimized-location virtual reference method (OLVR) generates partial fields which are related to independent sound sources. This method is comprehensively described by Kim *et al.*,⁵⁴ who developed it. Its application to the M-SONAH reconstructed F-22 sound fields is detailed by Wall⁵¹ and is briefly described here; modifications necessary to produce OLVR partial intensity fields are also noted.

After SONAH has produced three-dimensional, reconstructed pressure and particle velocity fields near the sound source as described above, virtual reference locations are chosen according to some scheme. The virtual references can be located anywhere within the field reconstructed by SONAH, and should be chosen to best represent individual sources. If a field is produced by multiple source regions, choosing virtual references at the actual source locations would best allow for separation of the contributions from each of these sources, so that OLVR would produce partial fields that are due to each individual source.

One algorithm that may be used to optimize virtual reference locations is called Multiple Signal Classification (MUSIC), which attempts to calculate the degree to which a candidate virtual reference location represents an actual source distribution. For a jet, the sound source is extended in space, so this calculation is nontrivial. The MUSIC algorithm does this by calculating the noise subspace in the reconstructed total field via singular value decomposition of the field. The highest singular values and associated vectors may be thought to correspond to sources, while the lowest singular values and vectors correspond to noise. That is,

$$\mathbf{R}_{\text{noise}} = \sum_n \mathbf{w}_n \mathbf{w}_n^H,$$

where each \mathbf{w}_n is a noise-related vector, with length equal to the total number of sampled points in the field.

Each candidate virtual reference location is represented by a trial vector,

$$\mathbf{u} = [0 \ 0 \ 0 \ \dots \ 1 \ \dots \ 0 \ 0 \ 0]^T,$$

where the “1” corresponds to the source location. The MUSIC power of each candidate location is then calculated by,

$$P_{\text{MUSIC}} = \frac{1}{\mathbf{u}^H \mathbf{R}_{\text{noise}} \mathbf{u}}.$$

The locations with the highest MUSIC power most closely correspond to physical sources. In an extended source, such as with a jet, multiple points in the same region may have relatively high MUSIC power, but these extra points may be discarded. As described by Wall,^{17-18,55,51} high coherence between high MUSIC power locations indicates that only one virtual reference location is necessary.

Once the virtual reference locations are chosen, they are decomposed into a linearly independent basis set. All information coherent with the vector corresponding to the first reference is subtracted from the remaining vectors, and the remaining information coherent with the second is subtracted from all the rest, and so on. The SONAH-reconstructed sound field is then projected onto this basis to produce the individual OLVR partial fields. An energy-based sum of the partial fields results in reconstruction of the total SONAH-reconstructed field.

For the results that follow, virtual reference locations were found in the total pressure field found by M-SONAH, and then applied to both the pressure and particle velocity fields independently, then combined to form intensity partial fields. The scheme described above via the MUSIC algorithm was used to optimize virtual reference locations. It should be noted that other location optimization schemes may also be successful or better-suited to jet noise, and this problem merits further research.

3.4 Results

In order to apply the M-SONAH algorithm, a coherent measurement hologram is needed at each frequency. Thus, an SVD-based partial field decomposition was first applied to the scan-based measurement of the F-22 sound field along measurement plane 2.⁵⁶ Then, the measurement aperture was extended via numerical extrapolation to provide sufficient coverage of the source at low frequencies, below about 200 Hz.⁵⁷ M-SONAH was then applied to the resulting coherent holograms with reconstruction locations in the geometric near-field and at nozzle height of 1.9 m.

M-SONAH intensity reconstructions and the first five OLVR partial fields at one-third octave band center frequencies from 50 Hz to 500 Hz at military engine conditions are shown in Figs. 3-1 to 3-10, and at afterburner from 32 Hz to 500 Hz in Figs. 3-11 to 3-21. At 32 Hz for military conditions, not included here, the regularization process filtered out the majority of energy in the reconstructed sound field, indicating the possibility of high spatial noise levels at that frequency. For these figures, reconstructed data within the assumed shear layer of the jet plume has been discarded, since this holography method is not designed for use in areas where the fluid has mean flow. For purposes of illustration, only a few intensity vectors are shown, although the grid spacing is much finer. The base of each arrow indicates the intensity reconstruction locations, while the color map indicates sound intensity level. To better compare with probe-estimated intensities, the levels indicated are scaled to reflect a 5.9 Hz bin width. Linear scaling of vector lengths used by the rendering program is kept consistent between partial fields at each engine condition.

For both engine conditions, the sound intensity levels in the total reconstructed intensity fields follow the spatial maps of the sound pressure levels,¹⁶ as expected of a field dominated by propagating sound. At each frequency, the field is dominated by one to several spatial lobes of maximum intensity. The number of important radiation lobes increases with increasing frequency

– compare the single lobe at 80 Hz (Figs. 3-2 and 3-13) to the clear dual lobes at 200 Hz (Figs. 3-6 and 3-17). Above about 250 Hz, the lobes become difficult to distinguish in the total field, but the OLVR decomposition method is able to resolve multiple, compact lobes. In general, the maximum intensity direction points farther to the sideline with increasing frequency, while the acoustic source moves farther upstream (see Chapter 2). Above 315 Hz (see Figs. 3-8 to 3-10, 3-19 to 3-21), this source movement and shift in radiation direction creates a null at the shear layer starting at about $z = 15$ m and continuing downstream. Interestingly, the vector intensity directions across each lobe are consistent at farther than 1-2 m from the jet shear layer, so that a ray traced outward from one vector would generally encounter the same direction of energy flow. This consistency seems to give support for use of mid-field intensity measurements to predict far-field directivity patterns (see Sec. 2.6). Because of our choice of two sets of wavefunctions, the interference between the signal reflected off the ground and the direct signal, (near $x = 3-5$ m in Figs. 3-3 to 3-5, 3-14 to 3-16 and also farther to the sideline for higher frequencies), is well captured by the M-SONAH process, seen in the spatial nulls of the intensity magnitude.

Maximum sound intensity levels for military engine conditions are lower in magnitude by up to 5-7 dB compared to those at afterburner. Although the maximum intensity lobes at 160, 200 and 250 Hz are lower in magnitude, a discrete transition in dominance from one high-magnitude radiation lobe to another is more evident at military (see Figs. 3-5 to 3-7). Note the prominent maximum intensity lobe at 160 Hz (Fig. 3-5), which has consistent intensity vector directions. At 200 Hz (Fig. 3-6), a second lobe emerges with different intensity directions, and the second lobe dominates the radiation at 250 Hz (Fig. 3-7). The two lobes not only differ in location, but also contain discrete vector directions (this phenomenon is explored in detail in Appendix A).

Use of OLVR to separate the contributions from individual radiators seems to isolate these radiation lobes from 160-250 Hz, indicating that multiple mutually-incoherent acoustical sources are important in this frequency region. The separation is especially clear between partial fields 1 and 3 at 200 Hz (Figs. 3-6 and 3-17) for both engine conditions, where the primary radiation lobes in the partial fields have clearly different locations and intensity vector directions.

3.4.1 Military reconstructed intensity

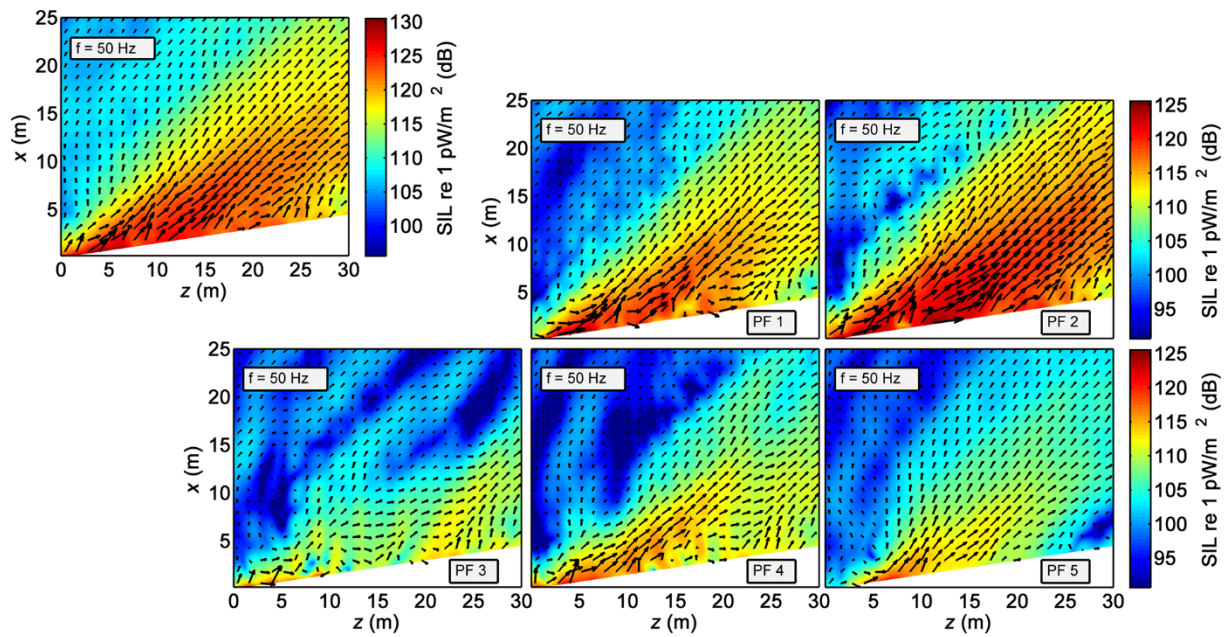


Figure 3-1. M-SONAH total reconstructed intensity field (top left) at nozzle height of $y = 1.9$ m and the first five OLVR partial fields decomposed from the total field, at 50 Hz and military conditions. Sound intensity levels are indicated by the color map and are scaled to reflect a 5.9 Hz bin width. The color scale and vector scaling is consistent between partial fields. Data within the approximate shear layer has been removed.

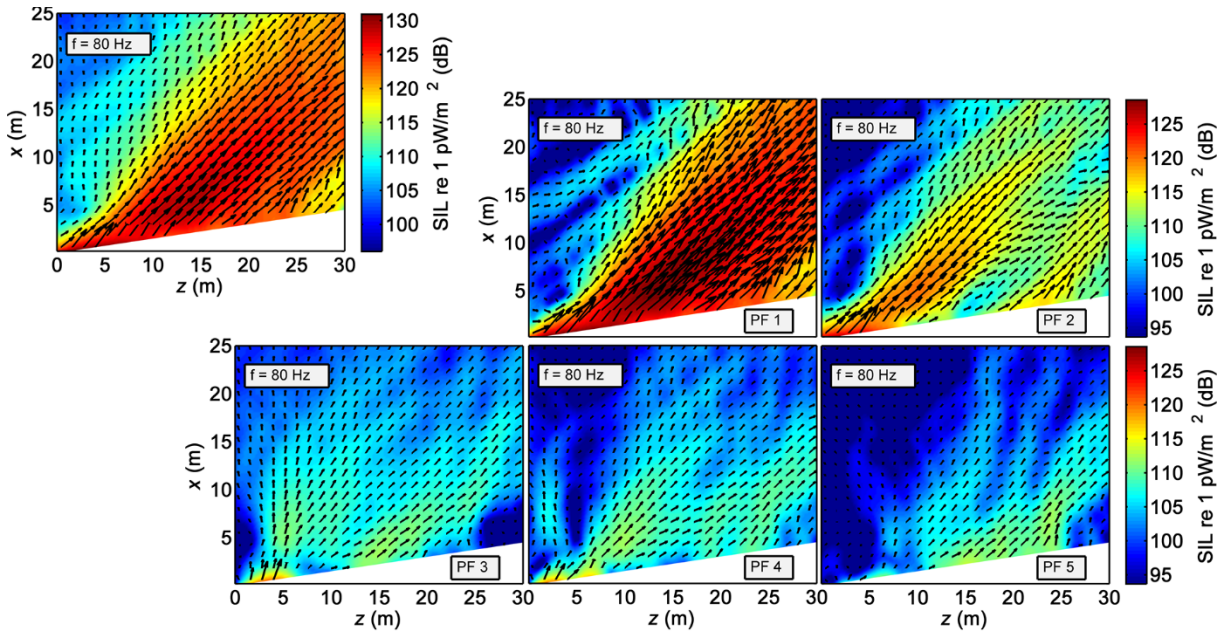


Figure 3-2. M-SONAH total reconstructed intensity field (top left) and the first five OLVR partial fields decomposed from the total field, at 80 Hz and military conditions.

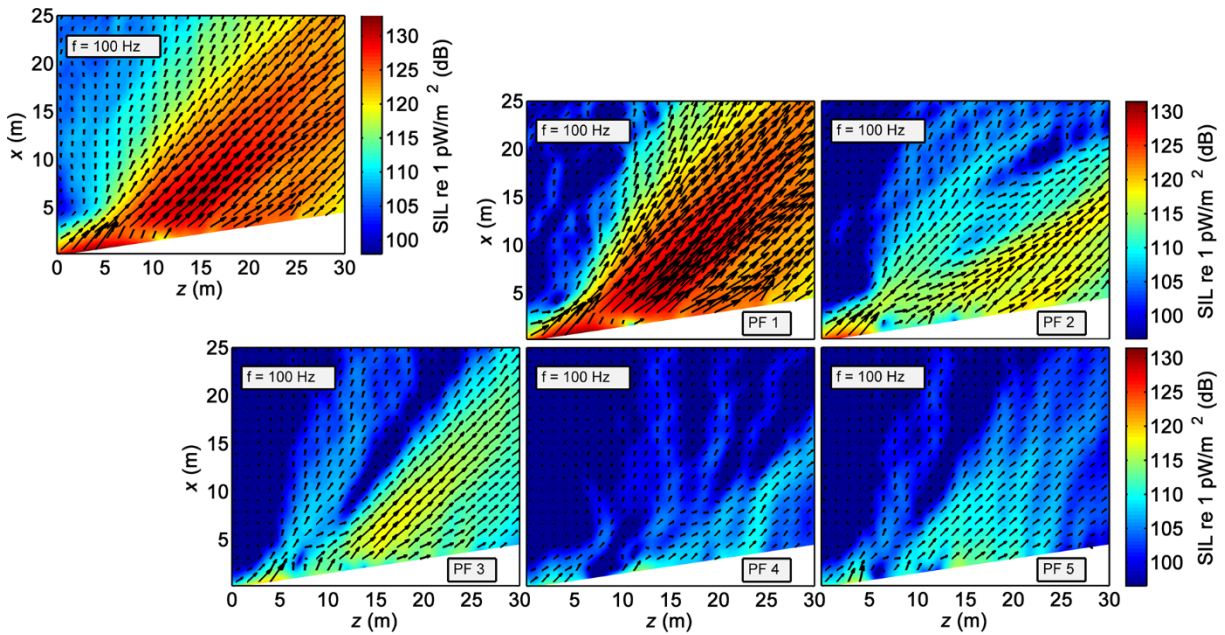


Figure 3-3. M-SONAH total reconstructed intensity field (top left) and the first five OLVR partial fields decomposed from the total field, at 100 Hz and military conditions.

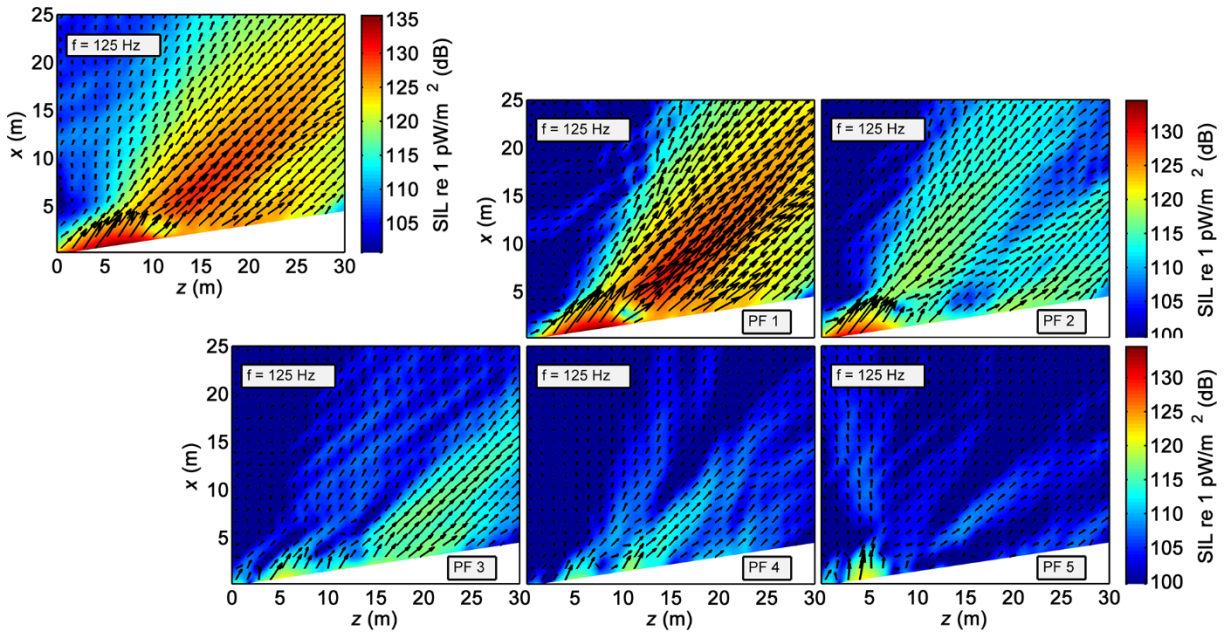


Figure 3-4. M-SONAH total reconstructed intensity field (top left) and the first five OLVR partial fields decomposed from the total field, at 125 Hz and military conditions.

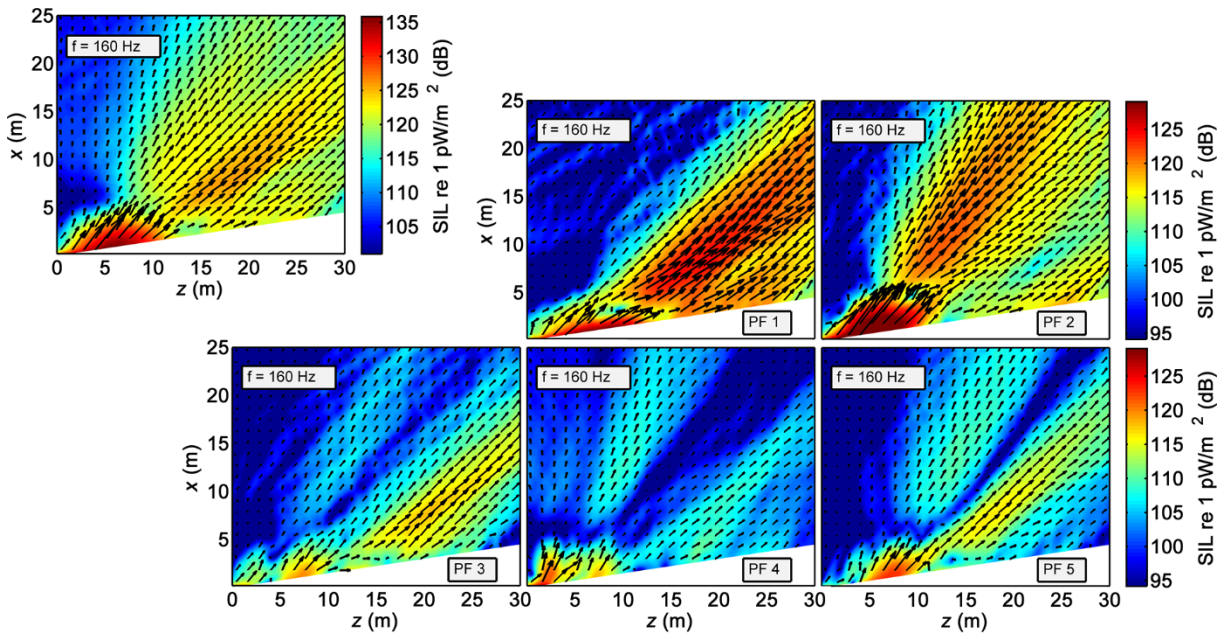


Figure 3-5. M-SONAH total reconstructed intensity field (top left) and the first five OLVR partial fields decomposed from the total field, at 160 Hz and military conditions.

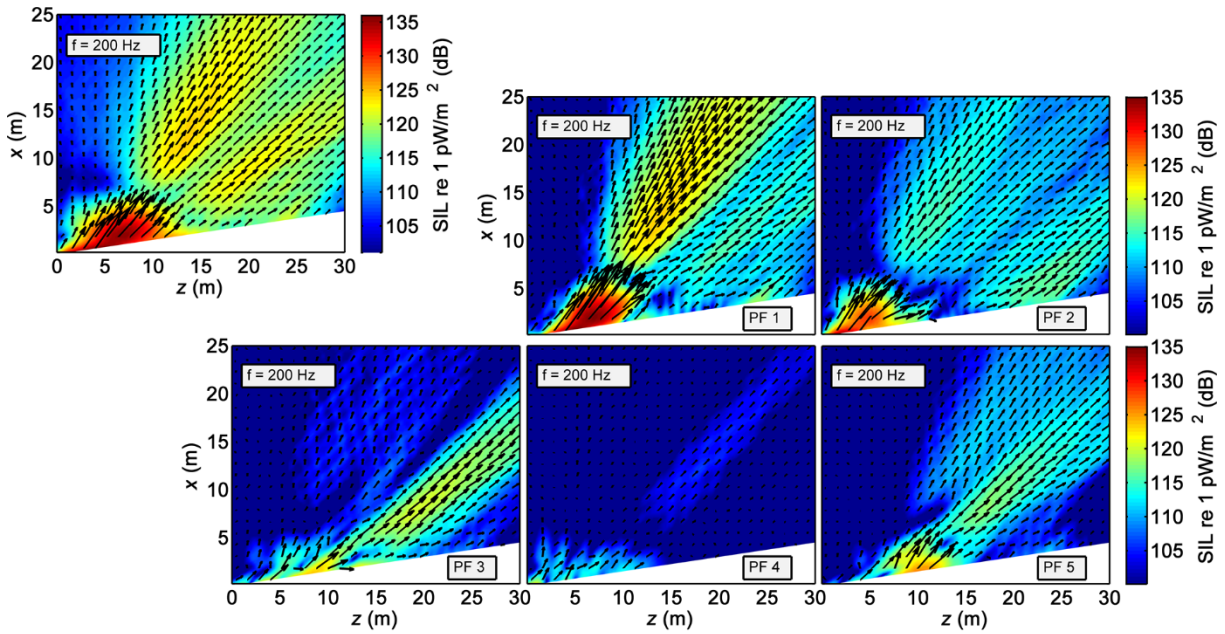


Figure 3-6. M-SONAH total reconstructed intensity field (top left) and the first five OLVF partial fields decomposed from the total field, at 200 Hz and military conditions.

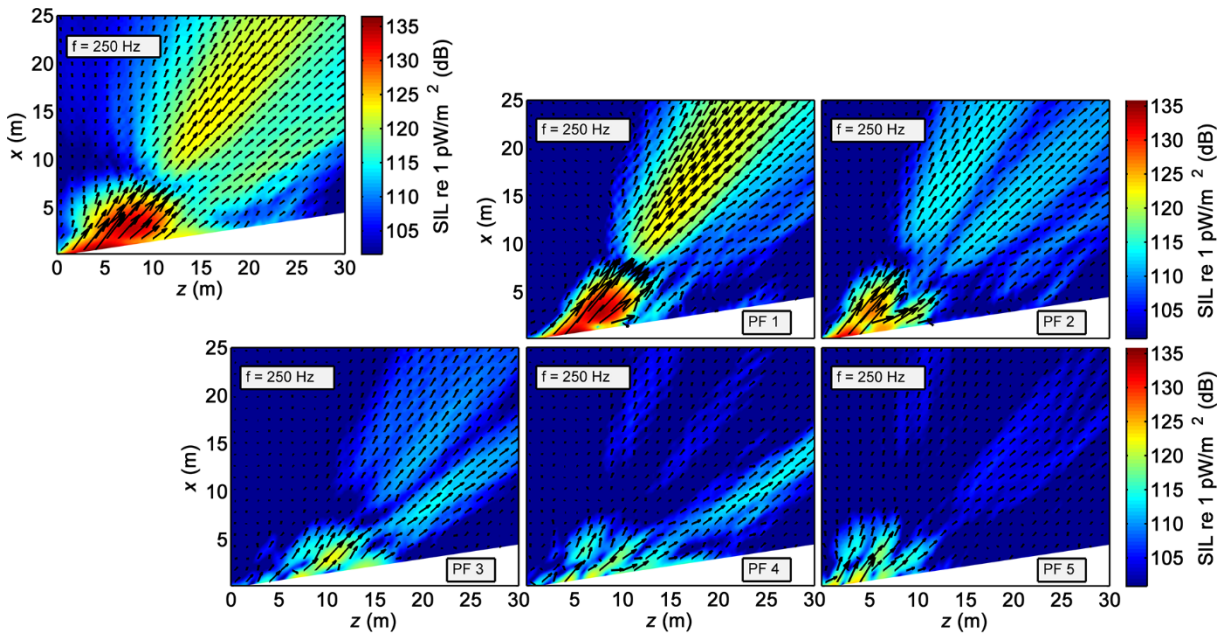


Figure 3-7. M-SONAH total reconstructed intensity field (top left) and the first five OLVF partial fields decomposed from the total field, at 250 Hz and military conditions.

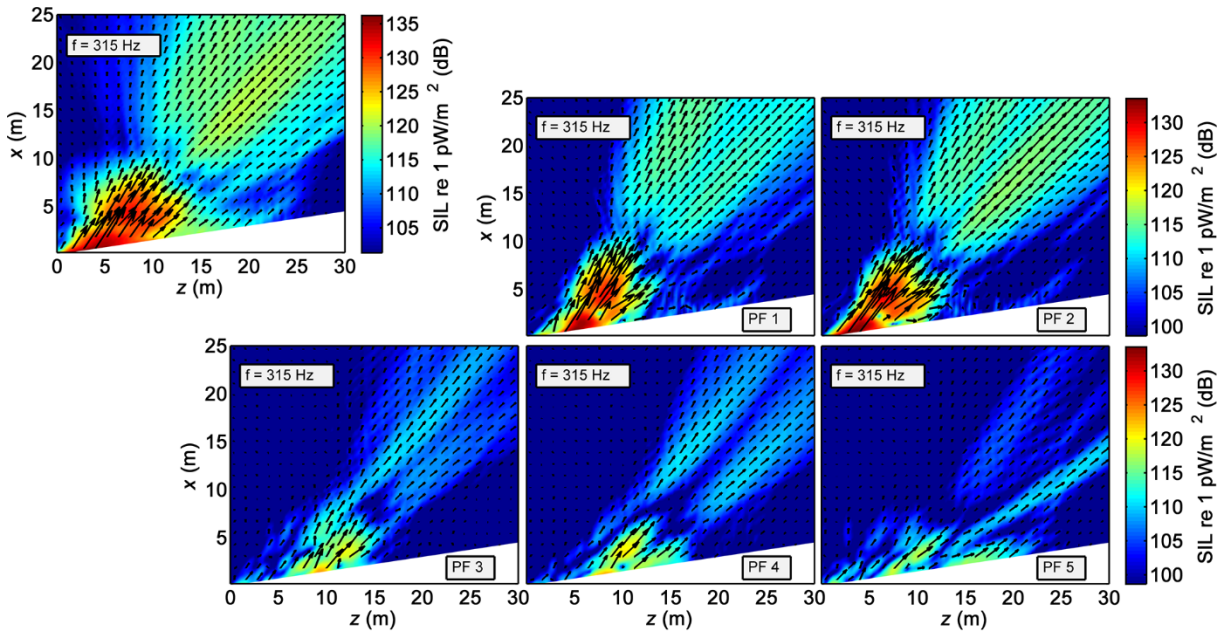


Figure 3-8. M-SONAH total reconstructed intensity field (top left) and the first five OLVR partial fields decomposed from the total field, at 315 Hz and military conditions.

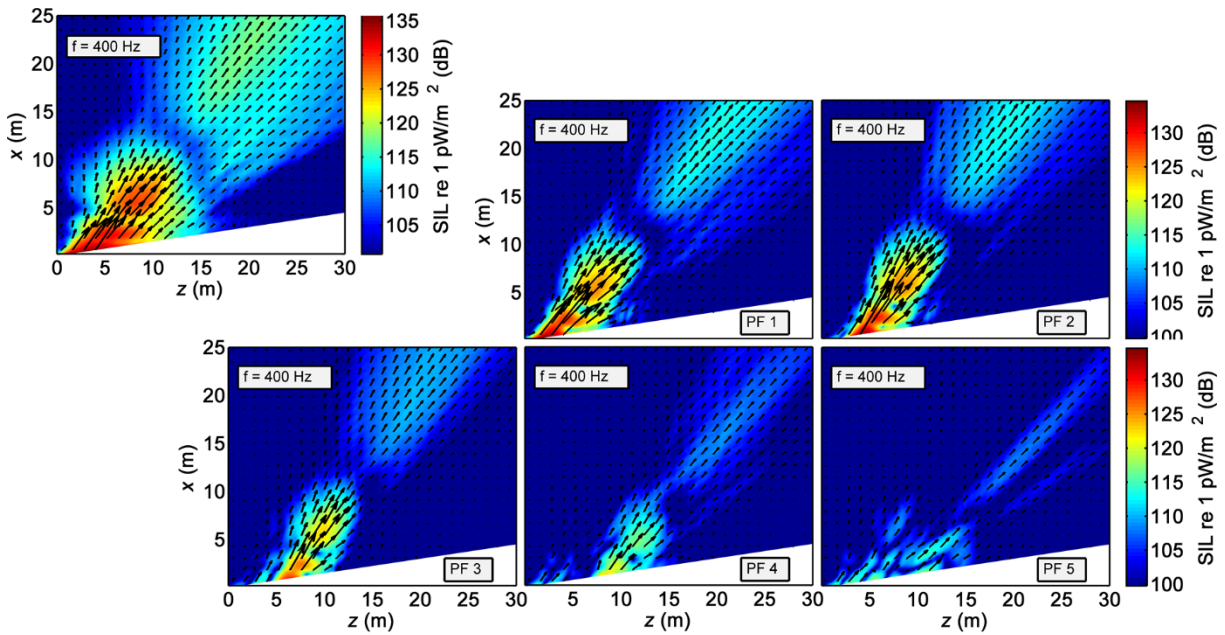


Figure 3-9. M-SONAH total reconstructed intensity field (top left) and the first five OLVR partial fields decomposed from the total field, at 400 Hz and military conditions.

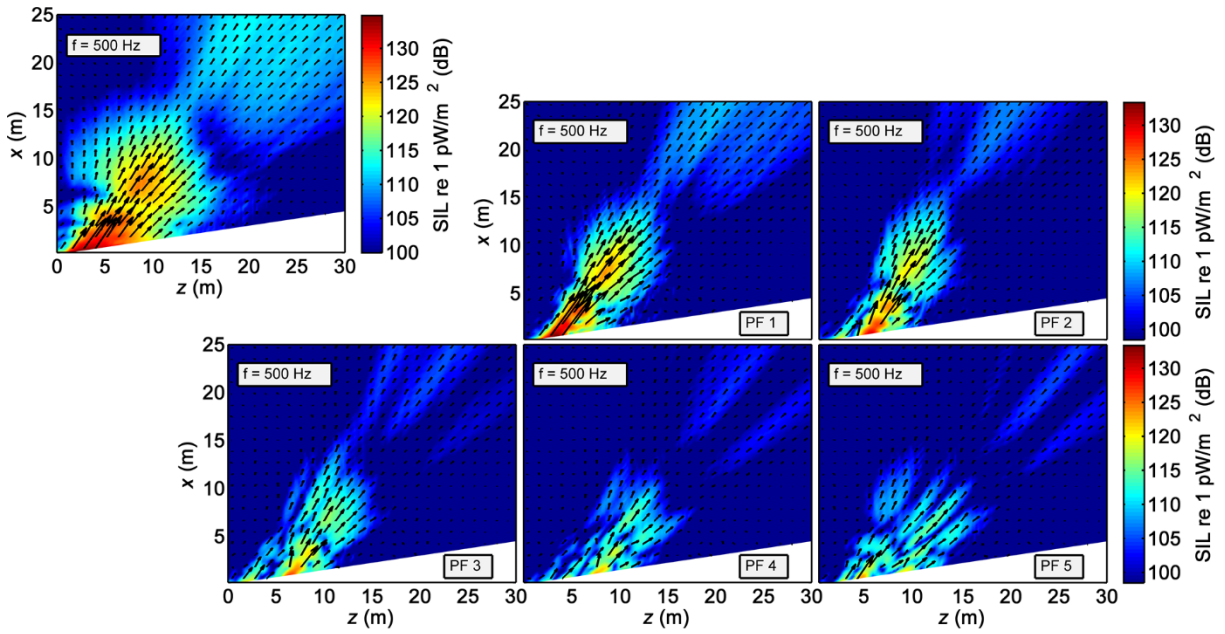


Figure 3-10. M-SONAH total reconstructed intensity field (top left) and the first five OLVR partial fields decomposed from the total field, at 500 Hz and military conditions.

3.4.2 Afterburner reconstructed intensity

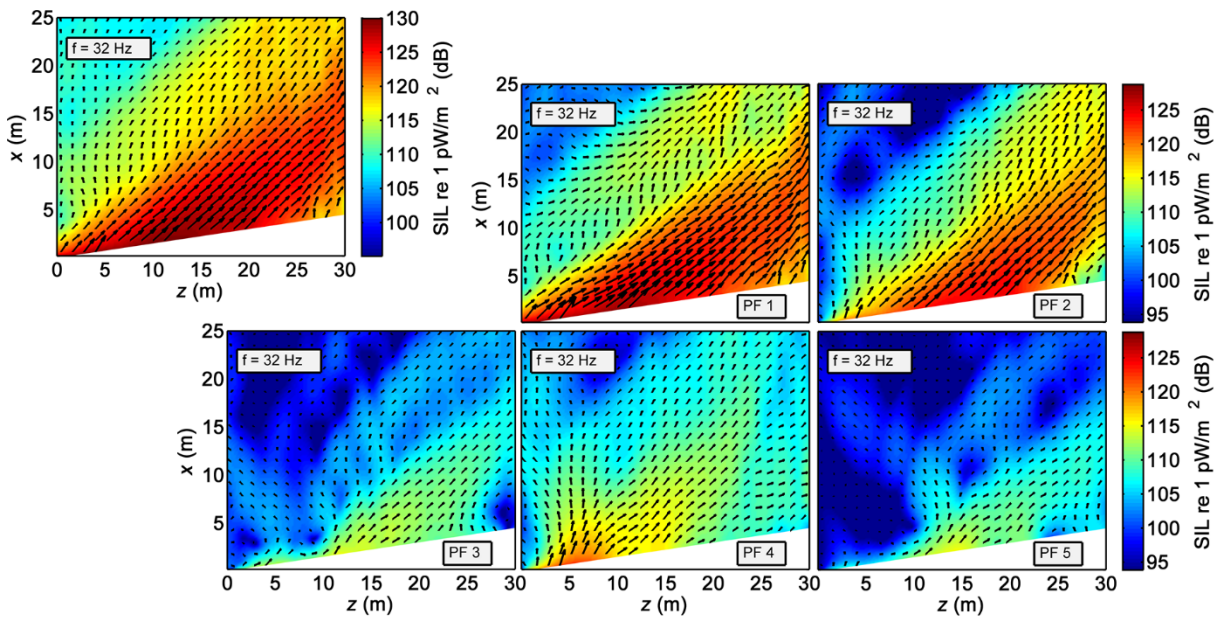


Figure 3-11. M-SONAH total reconstructed intensity field (top left) and the first five OLVR partial fields decomposed from the total field, at 32 Hz and afterburner engine conditions. Sound intensity levels are

indicated by the color map and are scaled to reflect a 5.9 Hz bin width. The color scale and vector scaling is consistent between partial fields. Data within the approximate shear layer has been removed.

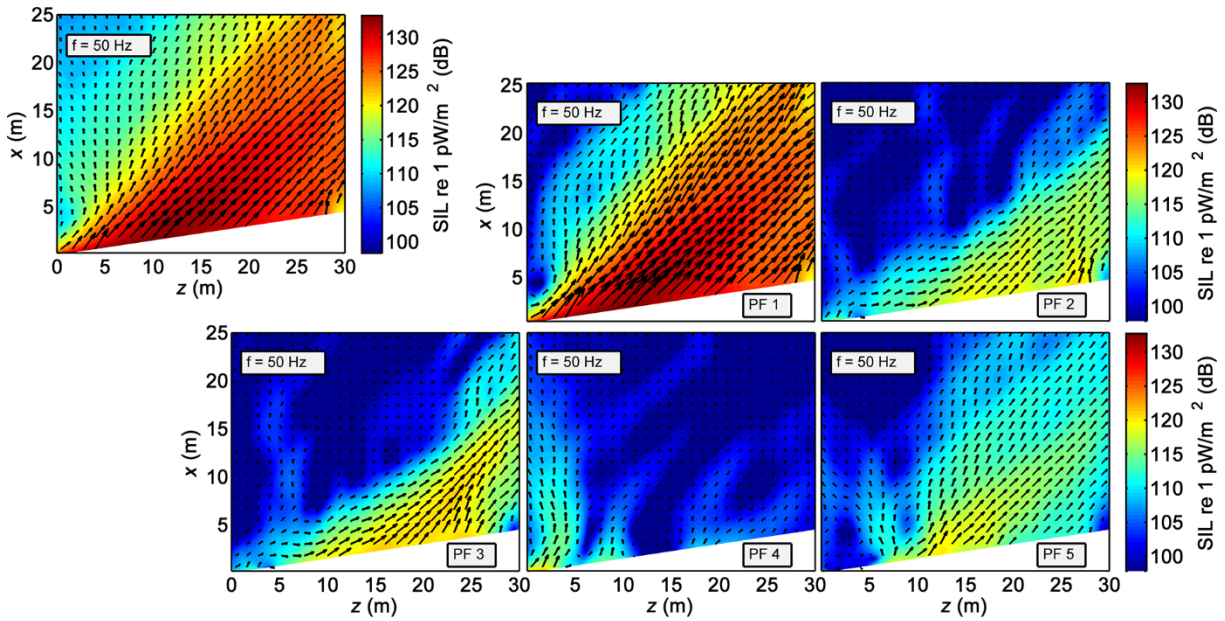


Figure 3-12. M-SONAH total reconstructed intensity field (top left) and the first five OLVR partial fields decomposed from the total field, at 50 Hz and afterburner engine conditions.

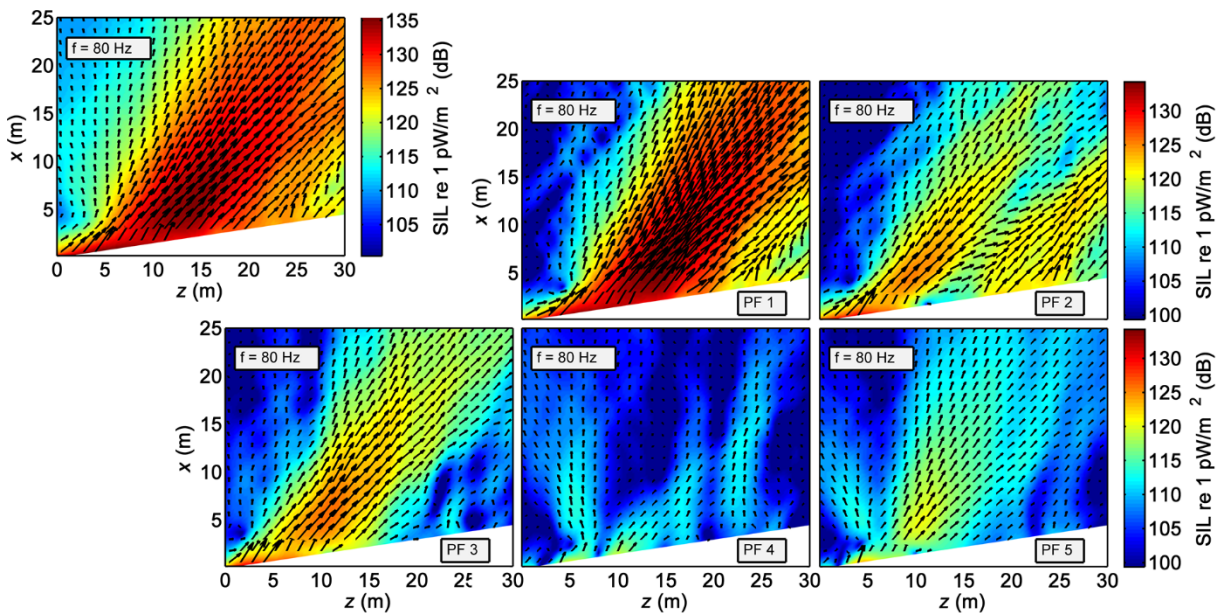


Figure 3-13. M-SONAH total reconstructed intensity field (top left) and the first five OLVR partial fields decomposed from the total field, at 80 Hz and afterburner engine conditions.

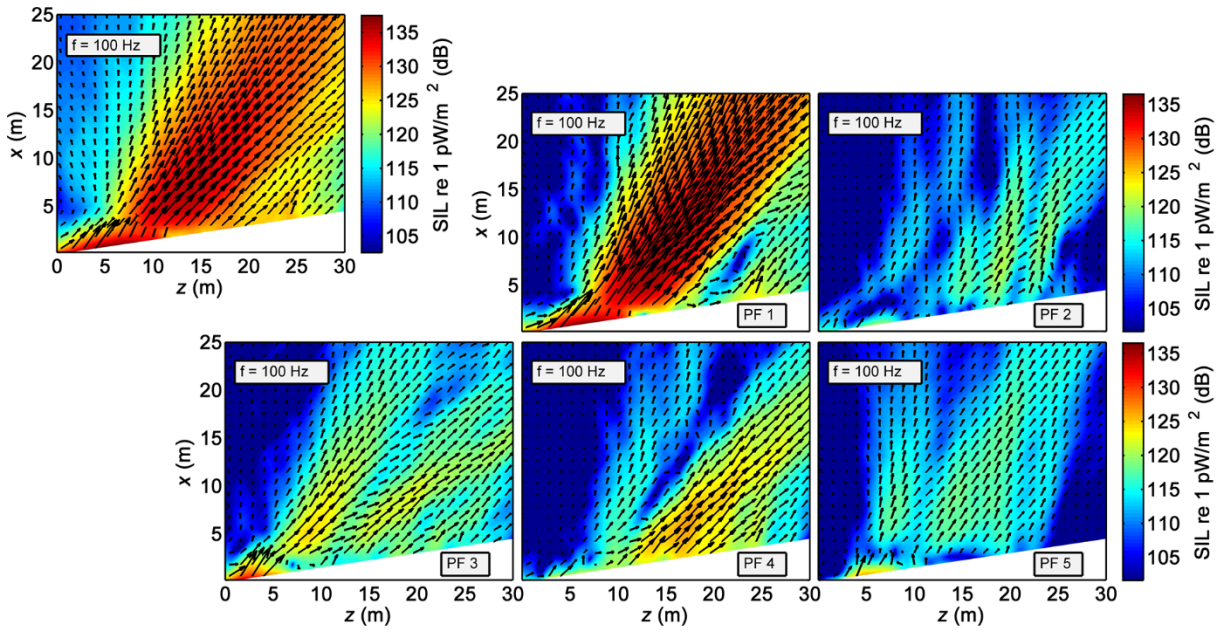


Figure 3-14. M-SONAH total reconstructed intensity field (top left) and the first five OLVR partial fields decomposed from the total field, at 100 Hz and afterburner engine conditions.

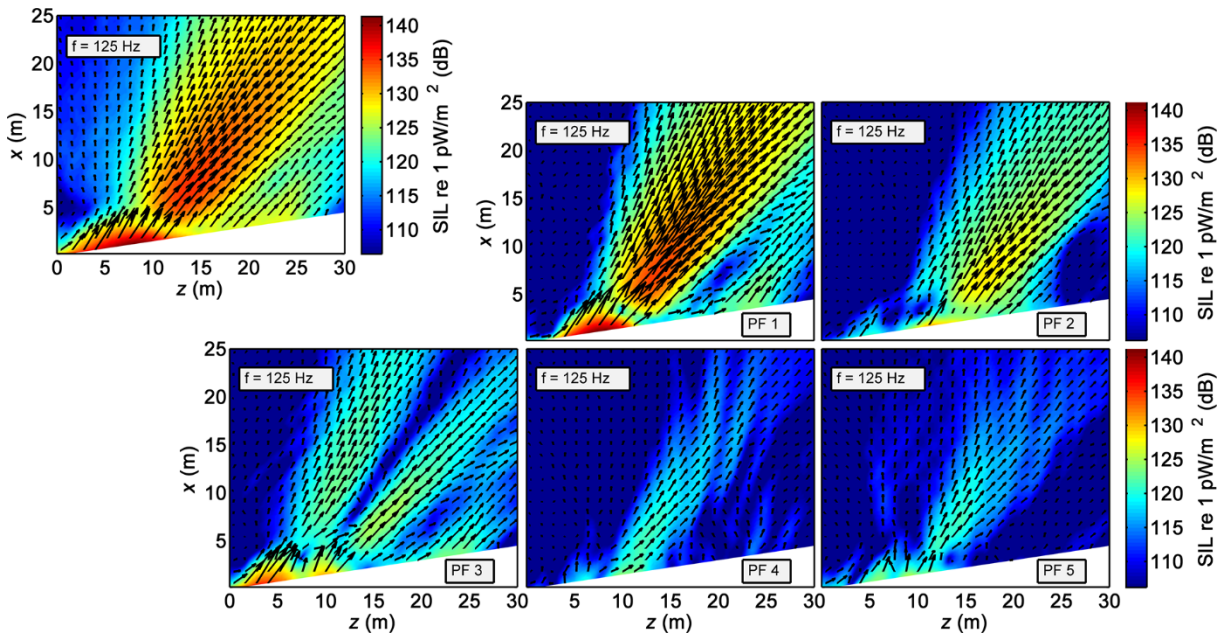


Figure 3-15. M-SONAH total reconstructed intensity field (top left) and the first five OLVR partial fields decomposed from the total field, at 125 Hz and afterburner engine conditions.

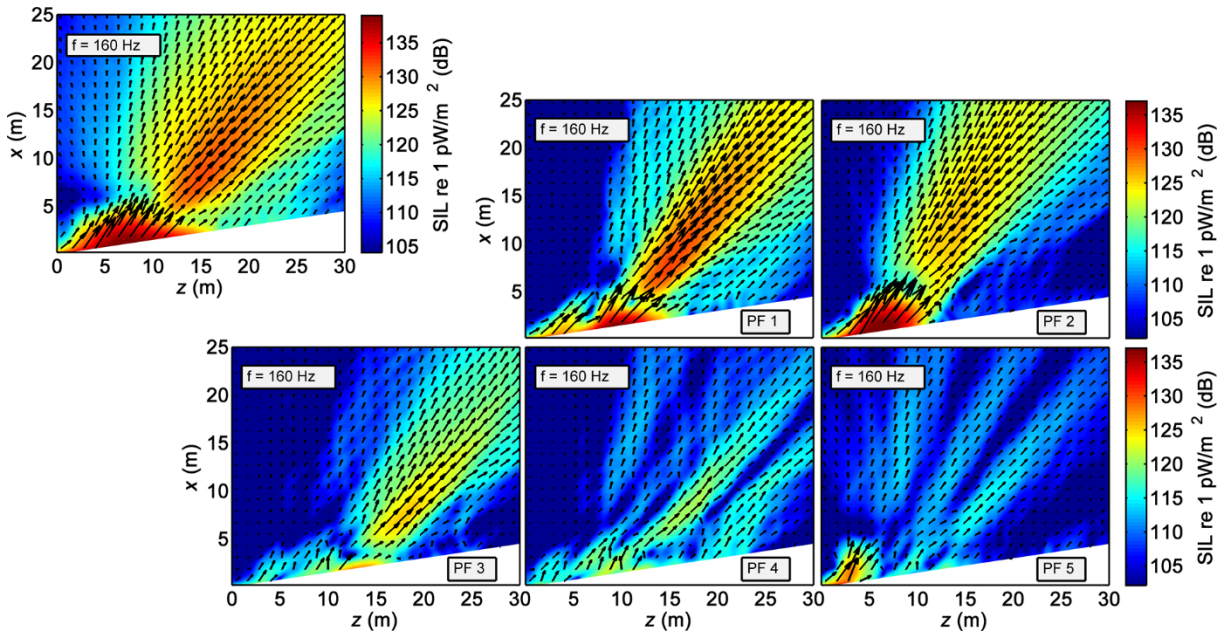


Figure 3-16. M-SONAH total reconstructed intensity field (top left) and the first five OLVR partial fields decomposed from the total field, at 160 Hz and afterburner engine conditions.

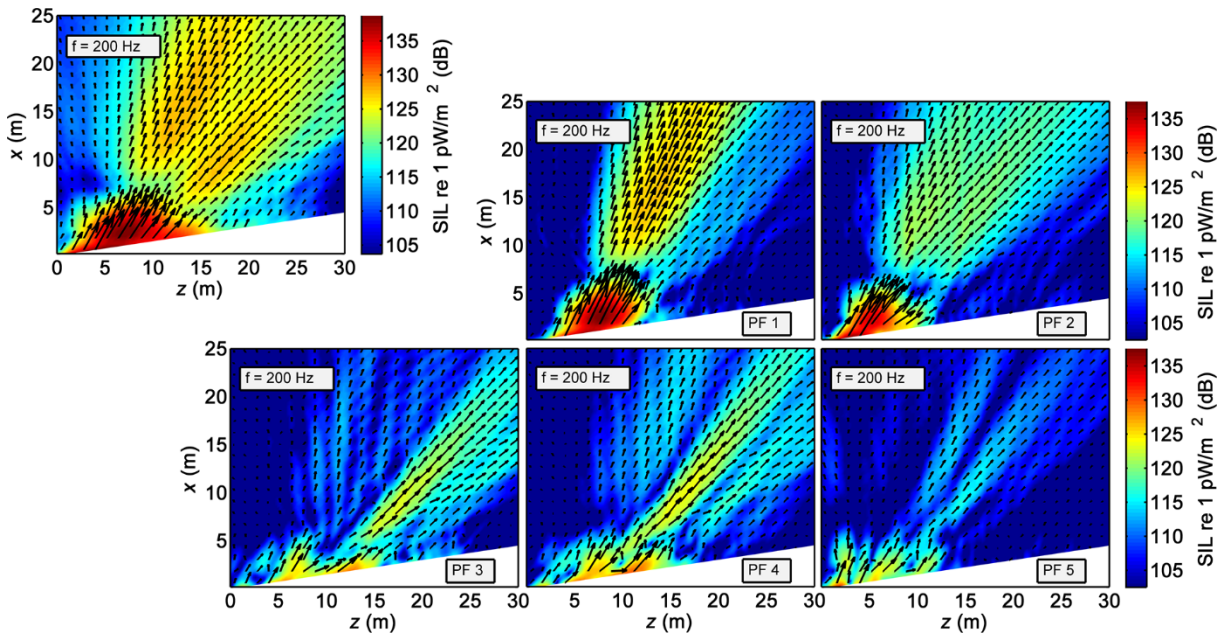


Figure 3-17. M-SONAH total reconstructed intensity field (top left) and the first five OLVR partial fields decomposed from the total field, at 200 Hz and afterburner engine conditions.

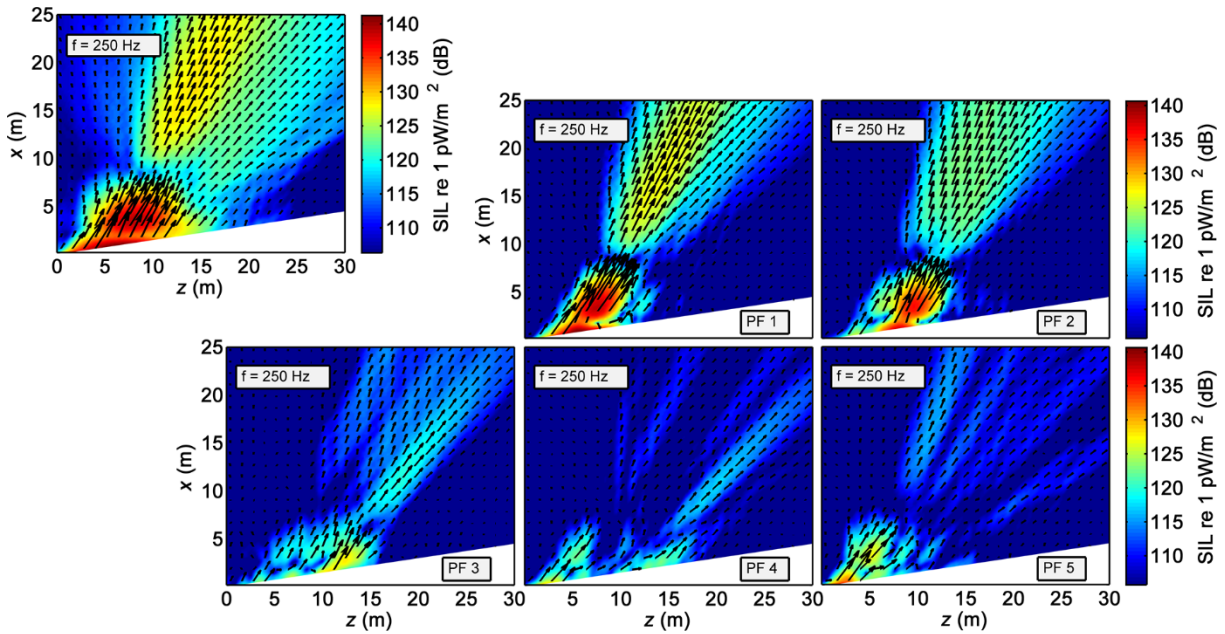


Figure 3-18. M-SONAH total reconstructed intensity field (top left) and the first five OLVR partial fields decomposed from the total field, at 250 Hz and afterburner engine conditions.

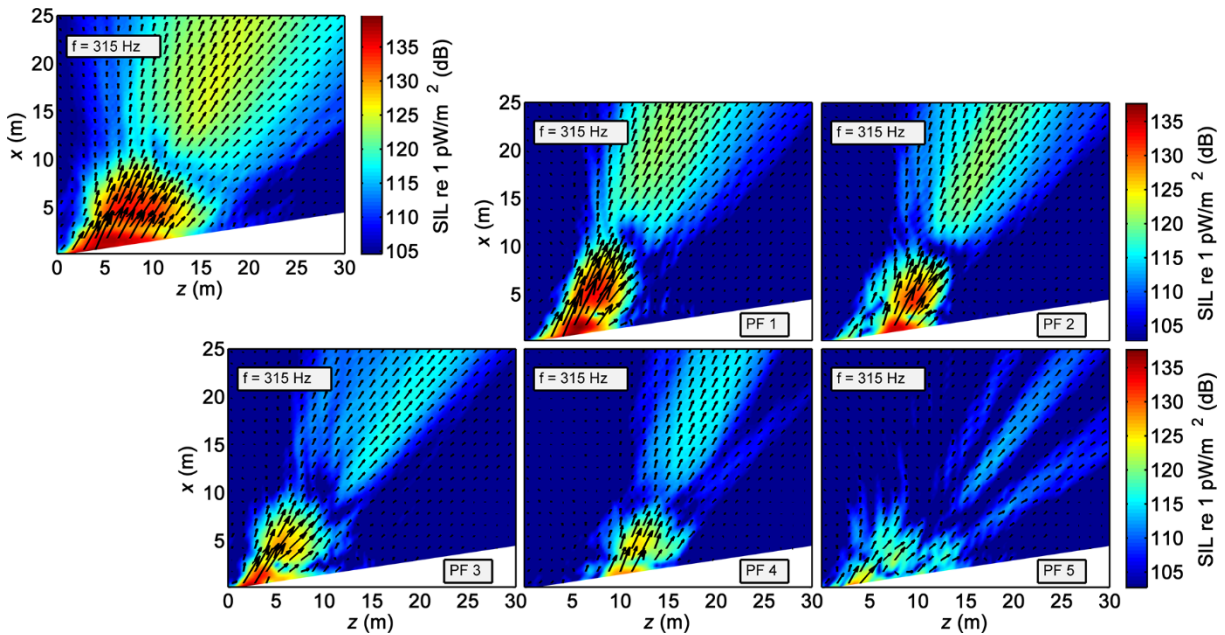


Figure 3-19. M-SONAH total reconstructed intensity field (top left) and the first five OLVR partial fields decomposed from the total field, at 315 Hz and afterburner engine conditions.

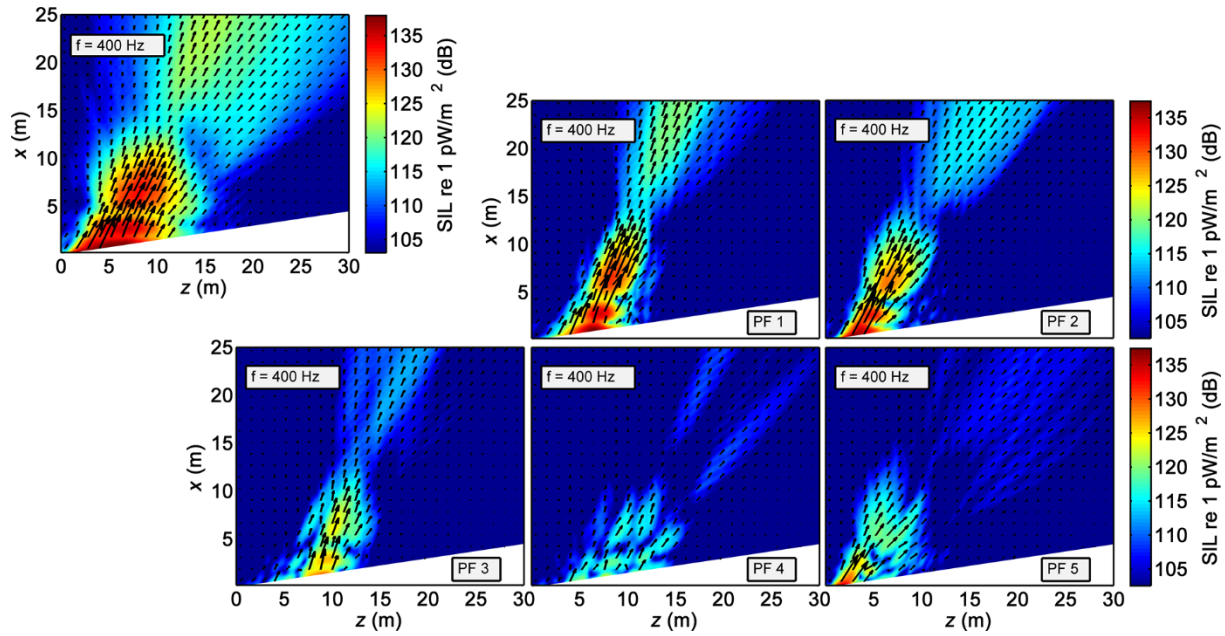


Figure 3-20. M-SONAH total reconstructed intensity field (top left) and the first five OLVR partial fields decomposed from the total field, at 400 Hz and afterburner engine conditions.

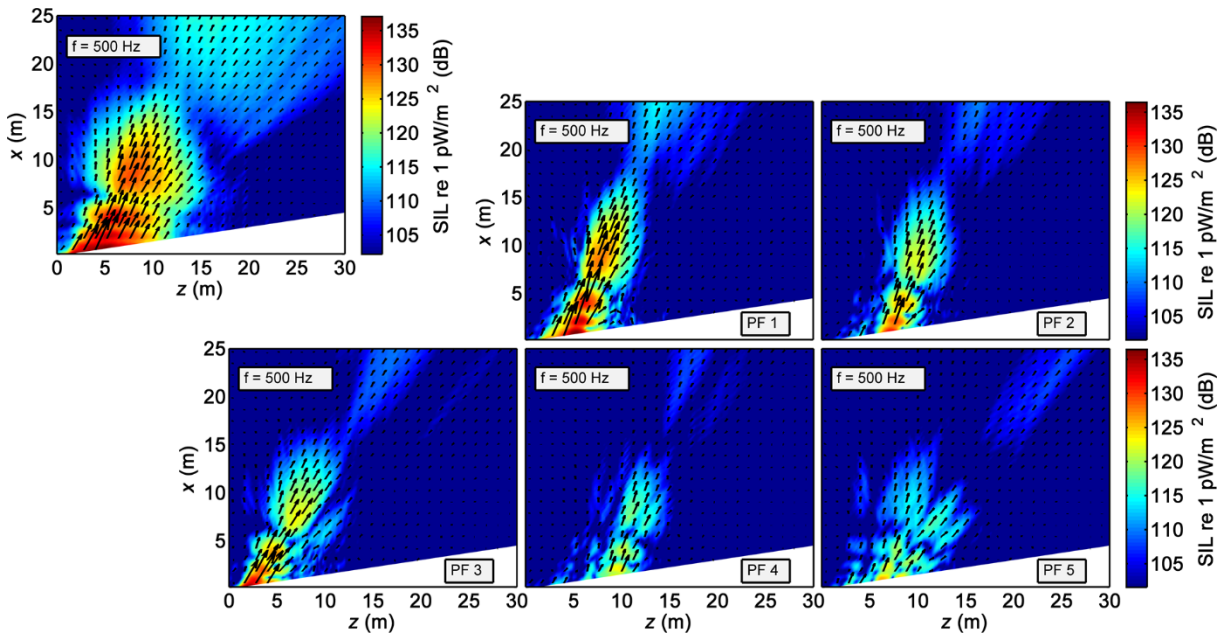


Figure 3-21. M-SONAH total reconstructed intensity field (top left) and the first five OLVR partial fields decomposed from the total field, at 500 Hz and afterburner engine conditions.

3.5 Comparison with probe intensity estimates

As a benchmark measurement for evaluation of the M-SONAH results, total intensity reconstructions at probe height (2.54 m) are compared with intensity estimates calculated from probe measurements. Results at one-third octave frequencies from 100 to 500 Hz, where both methods are expected to produce accurate estimations, are shown in Fig. 3-22. As explained in Sec. 2.4, 100 Hz marks the lower frequency limit of accurate intensity estimation with the current probe design, while an upper frequency limit for M-SONAH of about 500 Hz is dictated by the holography rig microphone spacing. The differing capabilities of the two methods are emphasized in these comparisons. Below about 200 Hz, reconstructed vector directions at the measurement planes point up to about 10 degrees farther aft than the intensity probe estimates. Because M-SONAH reconstructed pressures agree with benchmark measurements at these frequencies at plane 1 and the arc,⁴⁷ the reconstructed intensity directions are likely more accurate. The constant directional bias of the vectors from the intensity probe is indicative of some phase mismatch in the probe microphones. The source region based on ray-tracing (see Sec. 2.6.2) from reconstructed intensities would be located farther upstream by up to 1-2 m at 100-200 Hz. This shift is mitigated by the fact that the measurement planes are close to the jet, and that the intensity magnitudes from both methods correlate somewhat closely. Interestingly, the intensity reconstruction along the measurement arc follows closely with intensity directions and magnitudes from the probe up to 500 Hz, where the frequency limit of holography with this array is reached.

Some nulls in the reconstructed intensity magnitudes along the measurement planes are not as prominent in the measured intensity, at 160-250 Hz. For example, at $z = 11$ and 13 m along plane 1 at 160 and 200 Hz, respectively, the reconstructed magnitude is lower by up to 10 dB. This is because the analytical wave functions used in the SONAH algorithm are allowed to

perfectly interfere, not including the effects of finite ground impedance and phenomena such as turbulence, so the reconstructed magnitude nulls are much deeper. In this case, the intensity probe estimates are likely more accurate.

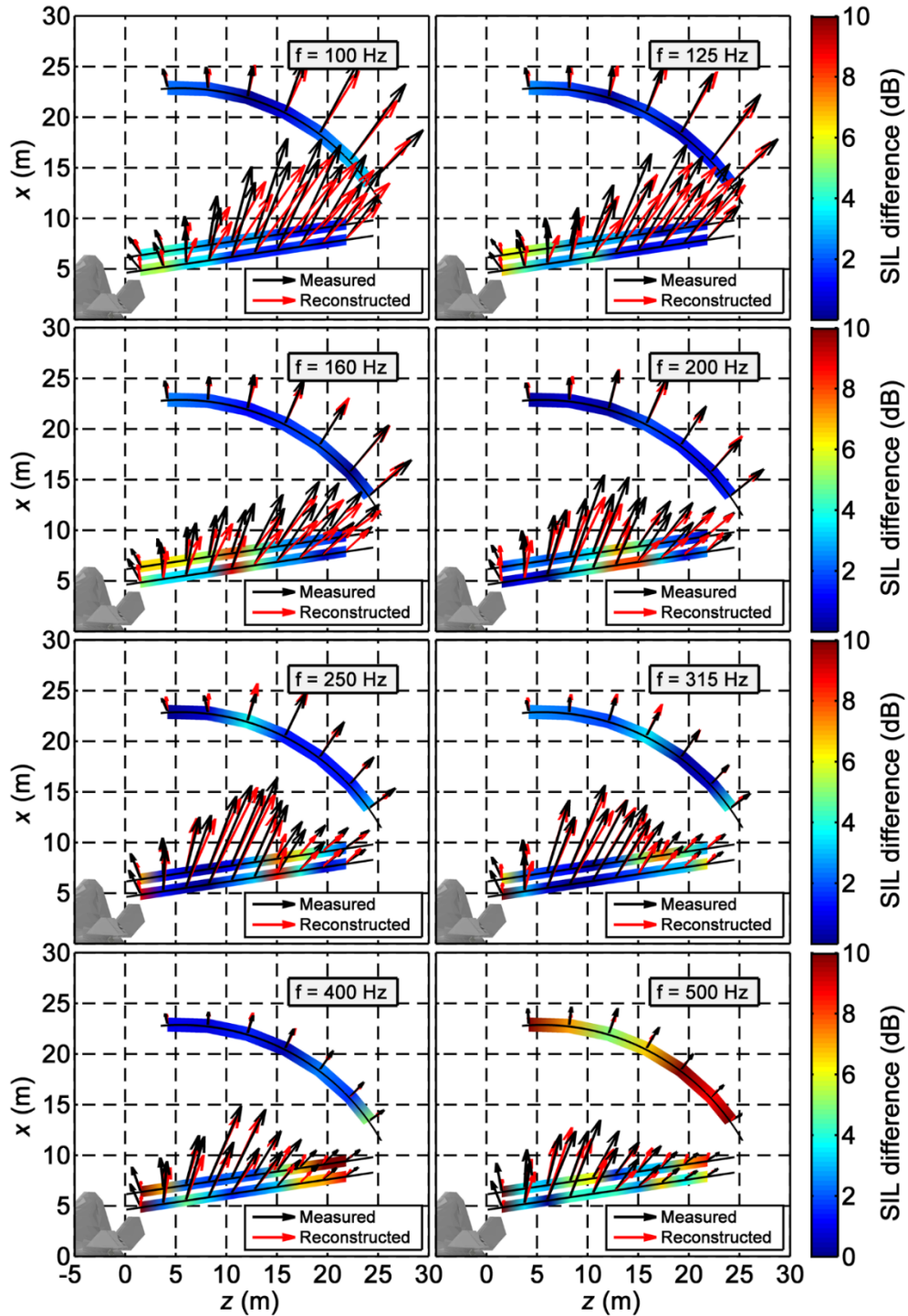


Figure 3-22. M-SONAH reconstructed intensity at intensity probe locations compared with intensity estimates calculated from intensity probe measurements, at one-third octave band center frequencies and afterburner engine conditions. Internal scaling used by the rendering program to define vector lengths is kept consistent. The color map indicates the difference in sound intensity level between the reconstruction and measurement.

Below about 200 Hz, vector directions at the measurement planes differ by up to about 10 degrees, indicative of some phase mismatch in the intensity probe microphones. In addition, some nulls in the reconstructed intensity magnitudes along the measurement planes are not as prominent in the measured intensity, between 160-250 Hz. The intensity reconstruction along the measurement arc follows closely with measurement up to 500 Hz, where the frequency limit of the M-SONAH algorithm is reached.

This application of M-SONAH is part of a limited number of studies employing NAH to visualize a jet sound field. To the author's knowledge, it is the first reconstruction of the energy flow field near a full-scale jet using NAH methods. The total reconstructions indicate that the field is dominated by individual lobes of radiation with discrete directions of energy flow. These lobes are separated by OLVR decomposition, showing that they are created by mutually-incoherent source mechanisms. Finally, in the geometric near-field, the M-SONAH reconstructions agreed well with intensity measurements except at the points where the analytical wavefunctions were allowed to destructively interfere. The M-SONAH reconstructions closely follow intensity measurements along the arc, indicating that this method may provide the most reasonable estimates past the geometric near-field.

Chapter 4

Wavepacket optimization and analysis

The M-SONAH algorithm is able to estimate the pressure and particle velocities at any point in the three-dimensional volume surrounding the jet. However, the algorithm used in Chapter 3 is not designed to accurately predict these quantities once inside the shear layer, because the homogeneous Helmholtz equation is no longer satisfied. Rather, reconstructions inside the jet plume describe equivalent source distributions, which result in the physically-accurate pressure and particle velocity predictions outside of the shear layer. In the search for a mathematical model of jet noise, such an equivalent distribution is valuable information. This chapter focuses on the development of one such model, based on wavepackets, and evaluates its capacity for describing the jet acoustic source. While the full wavepacket model involves consideration of jet fluid dynamics along with the acoustics, only a preliminary, mathematical treatment based on acoustical results from Chapter 3 is presented here, in preparation for future work.

4.1 Introduction

The idea of an equivalent source model (ESM) is to assume knowledge of some source characteristics to create an analytical model of the source that would produce (to some level of agreement) the measured data.⁵⁸ There is no one unique ESM for a given problem, as any model which predicts the measured data can be valuable. For example, Lighthill modeled the source of jet noise as a collection of quadrupoles (an elementary source in sound radiation theory) with some success.^{59, 60} Miller used a similar mathematical “acoustic analogy”, informed by the length scales of the turbulence and other parameters, to correctly model the constructive and destructive interference pattern seen acoustically when a jet is near a rigid surface.⁶¹ Based on the presence of both correlated and uncorrelated jet noise characteristics, Tam developed a “two-source” equivalent source model to represent contributions from fine-scale and large-scale turbulence.³⁵ Based on the two-source model, Morgan *et al.* modeled the jet source as two amplitude-shaped line arrays of monopoles along the jet axis, one correlated and steered, the other uncorrelated, which captured several observed features in the sound field (a similar ESM is explored in Appendix A).²³ In these ESMs and an additional one explored in this chapter, the parameters that define the model, e. g., source strength, placement, and phase, are important. The way that these parameters affect or do not affect how well a model matches data can point to further refinement of the model, or to development of better models and better understanding of the source.

One ESM applied to jet noise which has risen in interest recently is that of the wavepacket ansatz.⁴¹ The model is based on the presence of coherent structures in turbulent jet flow, which were discovered as early as the 1960’s.⁴² In essence, the wavepacket can be thought of as a shaped wave traveling along the jet direction. This traveling disturbance can be correlated over a large portion of the jet, not unlike the correlated line array of monopoles used in the ESM described in

Appendix A. As in Appendix A, because of the correlation, radiation from such a wavepacket is strongly directional, in keeping with observed jet noise characteristics. One goal of wavepacket modeling efforts is an attempt to marry jet fluid dynamics with observed acoustics.^{62, 63} However, because of the scope of such an attempt and the lack of appropriate measurement, the equivalent source wavepackets found herein are based solely on the acoustical data, with no attempt to explain the actual fluid mechanics.

There are multiple analytical functions that may describe the amplitude shaping of a wavepacket. In this chapter, the hyperbolic tangent function proposed by Papamoschou⁴¹ is used, which differs slightly from the Rayleigh distributions in Appendix A, however, there are other possible functions that can be applied in a similar manner.⁶⁴ The Rayleigh distribution was chosen previously to account for the spatial asymmetry in previous jet source descriptions,⁶⁵ having a steep rise and smoother decay in its amplitude along the jet axis. While both the Rayleigh distribution and the hyperbolic tangent distribution allow for an asymmetric spatial amplitude, the hyperbolic tangent model is more flexible and is able to accommodate both steep and slow rises and falls. In particular, the axial distribution is,

$$p(z) = \tanh \left[\left(\frac{z}{b_1} \right)^{g_1} \right] \left(1 - \tanh \left(\frac{z}{b_2} \right)^{g_2} \right) \exp(-i\alpha z),$$

where z is the downstream distance along the jet axis, b_1, g_1 , are input parameters related to the rising portion of the function, b_2, g_2 , are input parameters related to the decay, and α is related to the dominant spatial wavenumber of the wavepacket given by,

$$\alpha = \frac{\omega}{U_c},$$

where ω is the angular frequency of interest, and U_c is the convective velocity, or the speed at which the wavepacket disturbance advects downstream. Thus, estimates of U_c , a physical parameter of interest, may be found from a wavepacket analysis.

Azimuthal variations within the wavepacket model are also of interest,^{41-42, 66} but because of the small azimuthal aperture of the F-22 measurements, the wavepackets are assumed to be azimuthally symmetric for the remainder of this chapter. This choice reduces the problem to one dimension – a line source along the lip line (the line parallel to the jet centerline and intercepting the physical edge of the nozzle) is sufficient to describe one wavepacket. In general, the distribution will change as a function of frequency.

4.2 SONAH wavepacket optimization

In Chapter 3, application of acoustical holography provided reconstructions of the sound field in three dimensions near the F-22 jet plume, by projecting the data from measurement plane 2. To formulate a wavepacket model in the context of these reconstructions, the field reconstructions are extended up to the nozzle lip line, where the wavepackets are typically modeled. While the total reconstructed fields at the lip line are illuminating, applying an optimized partial field decomposition can reveal more about the individual, mutually incoherent sources by splitting the field into the isolated contributions from these sources.

The OLVR method creates partial fields out of the F-22 holography results up to the lip line. Interestingly, many of the individual partial fields along the lip line have amplitude envelopes and phasing which strongly resemble the hyperbolic tangent wavepacket distribution (See Figs. 4-1 through 4-22). This result seems to support the use of the wavepacket model to describe these mutually incoherent sources.

To compare OLVR partial fields with the wavepacket ESM, multiple optimizations are performed to find the best fit wavepacket parameters for the first several partial fields at each

frequency of interest. In particular, because the partial fields provide complex data, it is possible to optimize by matching the real and imaginary parts of the wavenumber spectra. The wavenumber spectrum of the wavepacket is closely tied with its associated convective velocity U_c , so that optimizing in the wavenumber spectrum allows for careful modeling of this important quantity. The cost function to be minimized is given by,

$$C = \left(\int |P_{0,OLVR}(k_z) - P_{0,test}(b_1, b_2, g_1, g_2, \alpha, k_z)|^2 dk_z \right)^{1/2},$$

where C is the numeric value of the cost function, $P_{0,OLVR}(k_z)$ is the complex wavenumber spectrum of the OLVR partial field as a function of wavenumber k_z , and $P_{0,test}(b_1, b_2, g_1, g_2, \alpha, k_z)$ is the complex wavenumber spectrum of a test wavepacket distribution as a function of wavenumber and wavepacket parameters. For these results, the OLVR partial fields were calculated out to $z = 30$ m downstream, then both the field and the test wavepacket distributions were zero-padded to provide smooth wavenumber spectra with the same spacing.

Previous work has led to the conclusion that the parameter space over this cost function is relatively flat, so that a single, long, optimization search with strict convergence criteria may not converge. Instead, randomly-initialized iterations of a simulated annealing algorithm⁶⁷ have so far proven successful in optimizing wavepacket parameters to fit the OLVR partial fields, giving bounds on the insensitive parameters. Previously, a Levenberg-Marquardt algorithm⁶⁸ was used to find optimized parameters for input into Rayleigh equivalent source distributions (see Appendix A for another treatment of these distributions). However, a simulated annealing algorithm is used in the present work. The algorithm attempts to overcome the possibility of becoming trapped in local minima by initially allowing for large random jumps in parameter space. The allowed jump “length” in parameter space is governed by a temperature-like quantity, which is lowered as the algorithm progresses, so that the algorithm converges to one answer. For each iteration of the

entire algorithm, an initial condition in the parameter space is randomly selected. If the answer is similar across a sufficient number of iterations, one can be reasonably confident that the answer is optimized across the parameter space. It is foreseeable that an inversion involving Bayesian statistics would provide a more rigorous treatment of the parameter space, and is a possibility for future research.

4.3 Optimization results

After running multiple iterations of the wavepacket optimization algorithm with the OLVR partial fields at afterburner, multiple sets of parameters are found which perform similarly, with relatively the same error. However, these iterations usually produce wavenumber spectra and associated wavepacket shapes that lie on top of each other, despite the differing sets of wavepacket parameters.

As with most inverse methods, the wavepacket parameters are nonunique, although, for the most part, the optimization converges to a similar wavenumber spectrum and corresponding wavepacket shape for a given partial field. That is, the parameters b_1 , g_1 , b_2 , and g_2 by themselves do not uniquely determine the wavepacket shape and spectrum, so associating these parameters with source characteristics is difficult and would require further research. Each optimization iteration does, however, return roughly equivalent convective velocities, however, because this quantity is closely tied to the peak wavenumber.

The number of OLVR partial fields with significant amplitudes varies as a function of frequency. At low frequencies, below about 125 Hz, the first partial field alone contains the majority of the energy along the lip line. In general, for the frequencies of interest here, the first two or three fields describe the majority of the energy in the field, though the fraction of energy in

the first three decreases as frequency increases. For the figures below, the first three partial fields (including the amplitude envelope and the real part) at the lip line are shown, along with their wavenumber spectrum amplitudes. The resultant wavepacket parameters and the value of the cost function are also tabulated.

Generally, the optimization finds reasonable fits for the first partial field, where the partial field wavenumber spectrum is dominated by a single peak because the analytical wavepacket wavenumber spectrum is also dominated by a single peak. Up to 315 Hz, the wavenumber spectra of the second or third partial fields contain multiple prominent spectral peaks, and the resultant match between the wavepacket shape and the partial field is therefore worse. However, choices in virtual reference locations differing from those proscribed by the OLVR algorithm (see Sec. 3.3) may result in partial fields that are better described by the single-peaked wavepacket spectrum of the hyperbolic tangent analytical wavepacket model.^{18, 55}

Below about 50 Hz, the partial fields are not as well described by wavepackets using the current choice of virtual reference locations (see Fig. 4-1). However, above this frequency, use of the complex wavenumber spectrum in the optimization seems to preserve important features in the wavepacket best fit, such as peak location and width. In addition, the real part of the wavepacket best fits contain the correct number of oscillations, and where the cost function is minimized well, the spatial phasing matches that of the OLVR partial field.

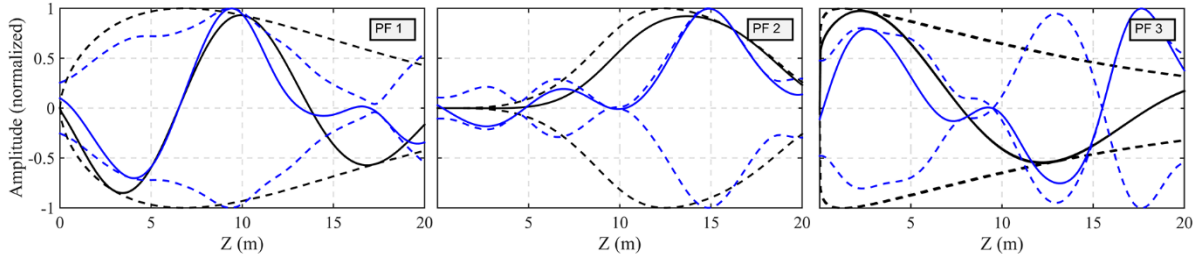


Figure 4-1. First three OLVR partial fields along the F-22 lip line (blue), and the corresponding wavepacket best fits (black), at 40 Hz and afterburner engine conditions. Amplitude is shown by dotted lines, and the real parts of both distributions are given by solid lines. Where all the iterations of the optimization algorithm closely coincided, the resultant best fits lie on top of each other.

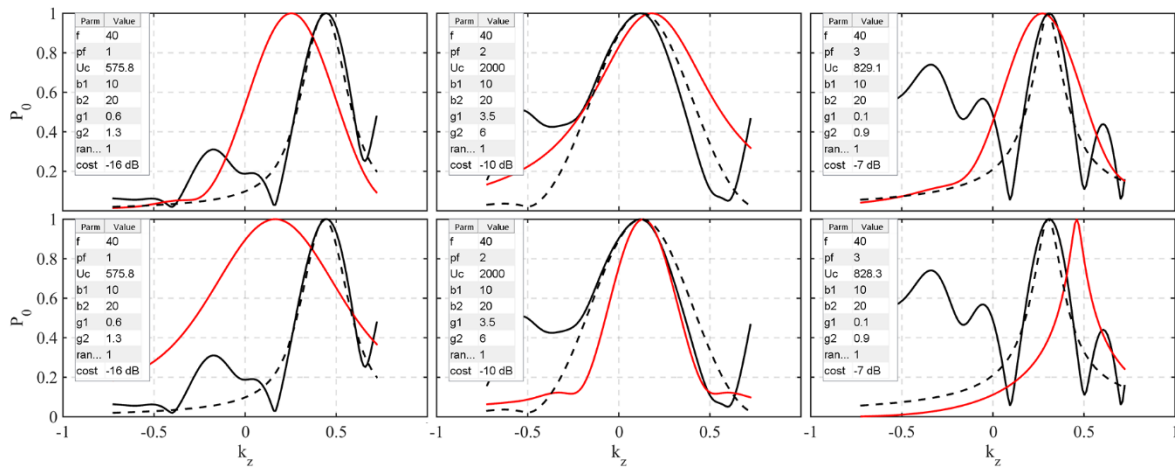


Figure 4-2. Amplitude of the wavenumber spectra corresponding to the OLVR partial fields at the lip line (solid, black), wavepacket best fits (dotted, black), and the randomized initial conditions given to the optimization algorithm (solid, red) at 40 Hz and afterburner engine conditions. Results for the first three partial fields are shown from left to right. For each partial field, the output from two example optimizations (top and bottom) are tabulated and shown.

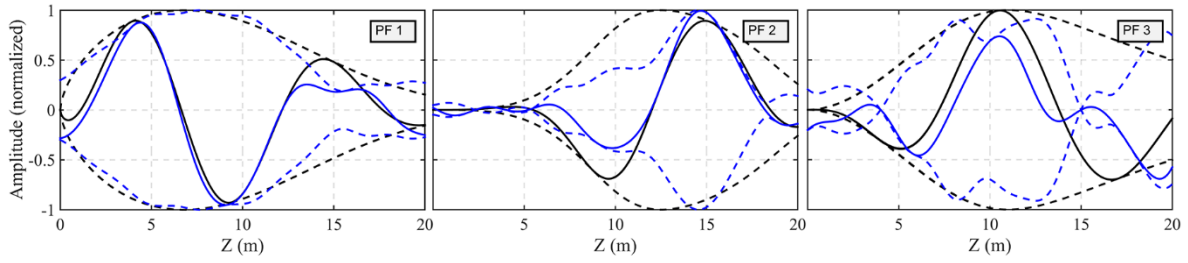


Figure 4-3. First three OLVR partial fields along the F-22 lip line (blue), and the corresponding wavepacket best fits (black), at 50 Hz and afterburner engine conditions.

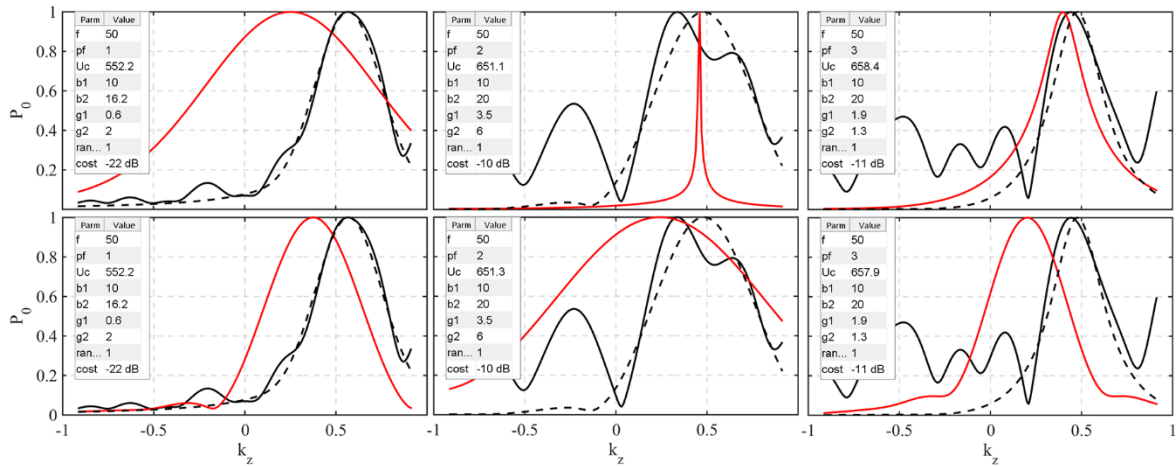


Figure 4-4. Amplitude of the wavenumber spectra corresponding to the OLVR partial fields at the lip line (solid, black), wavepacket best fits (dotted, black), and the initial conditions given to the optimization algorithm (solid, red) at 50 Hz and afterburner engine conditions.

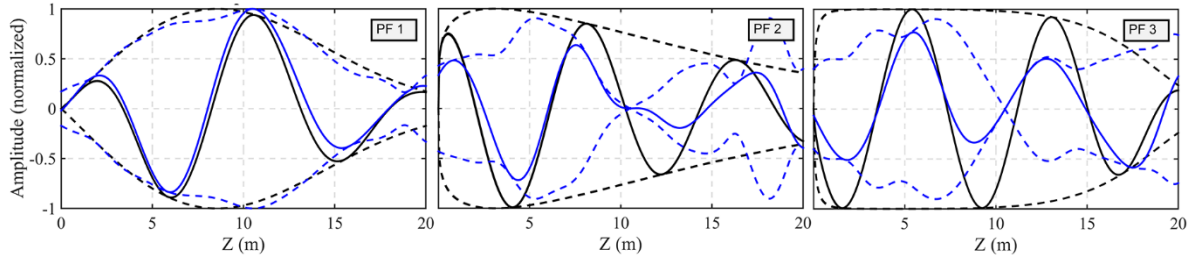


Figure 4-5. First three OLVF partial fields along the F-22 lip line (blue), and the corresponding wavepacket best fits (black), at 63 Hz and afterburner engine conditions.

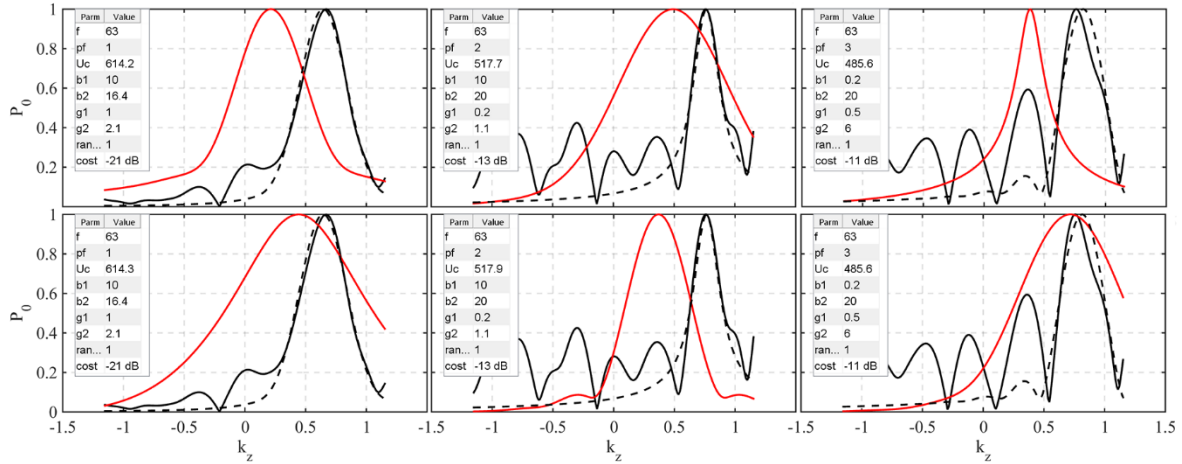


Figure 4-6. Amplitude of the wavenumber spectra corresponding to the OLVF partial fields at the lip line (solid, black), wavepacket best fits (dotted, black), and the initial conditions given to the optimization algorithm (solid, red) at 63 Hz and afterburner engine conditions.

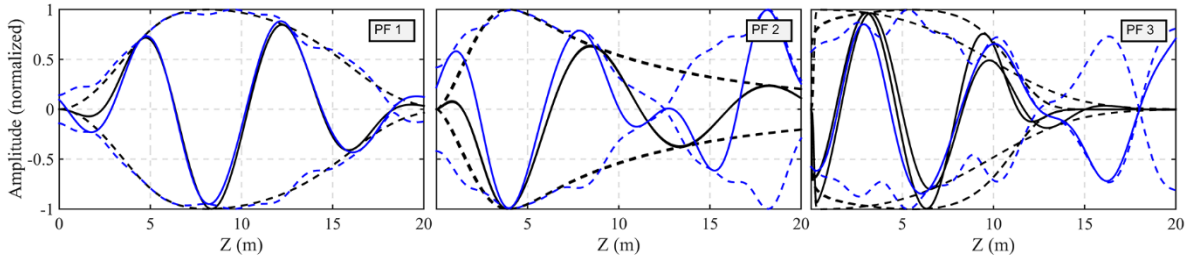


Figure 4-7. First three OLVR partial fields along the F-22 lip line (blue), and the corresponding wavepacket best fits (black), at 80 Hz and afterburner engine conditions.

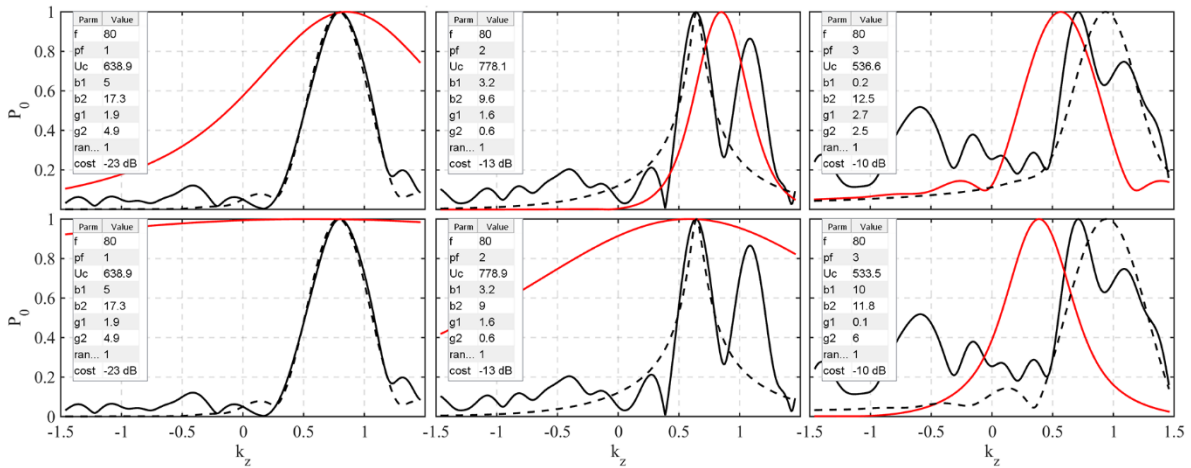


Figure 4-8. Amplitude of the wavenumber spectra corresponding to the OLVR partial fields at the lip line (solid, black), wavepacket best fits (dotted, black), and the initial conditions given to the optimization algorithm (solid, red) at 80 Hz and afterburner engine conditions.

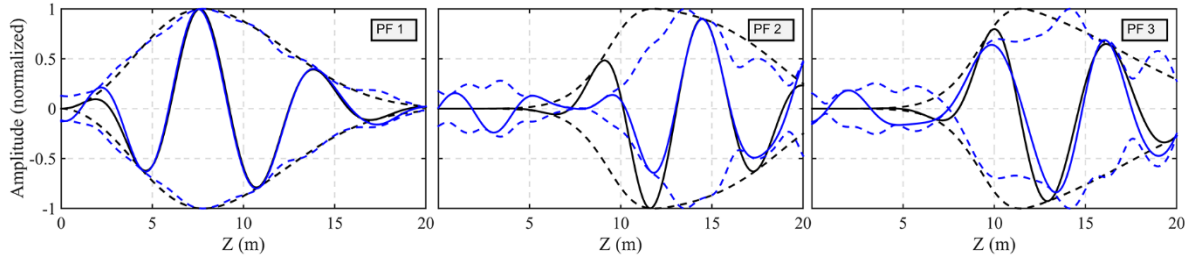


Figure 4-9. First three OLVR partial fields along the F-22 lip line (blue), and the corresponding wavepacket best fits (black), at 100 Hz and afterburner engine conditions.

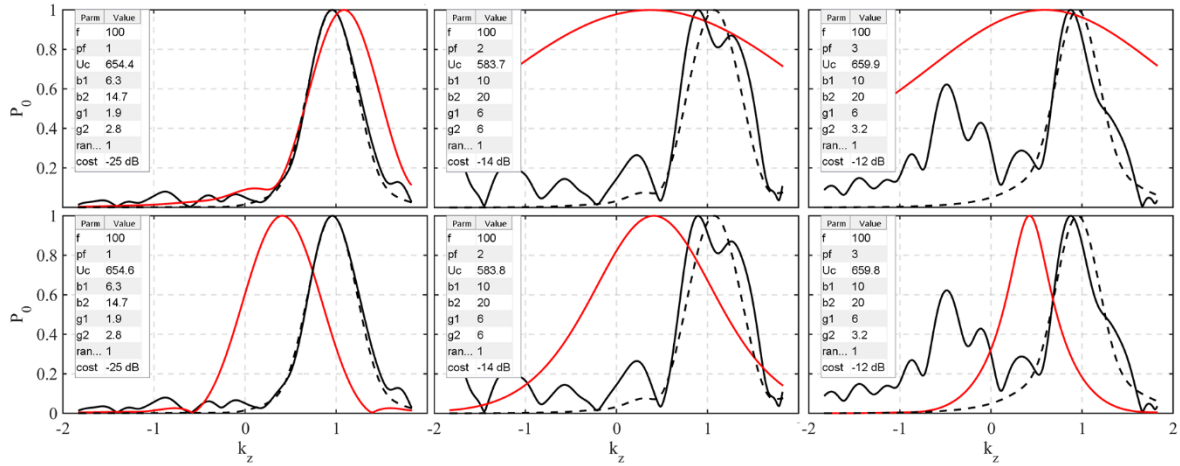


Figure 4-10. Amplitude of the wavenumber spectra corresponding to the OLVR partial fields at the lip line (solid, black), wavepacket best fits (dotted, black), and the initial conditions given to the optimization algorithm (solid, red) at 100 Hz and afterburner engine conditions.

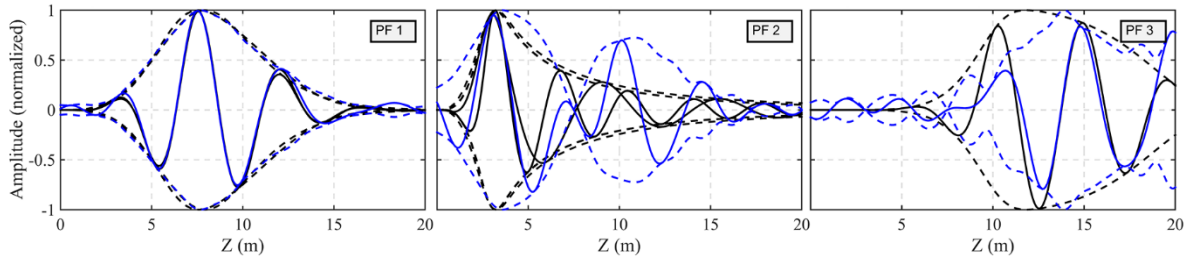


Figure 4-11. First three OLVR partial fields along the F-22 lip line (blue), and the corresponding wavepacket best fits (black), at 125 Hz and afterburner engine conditions.

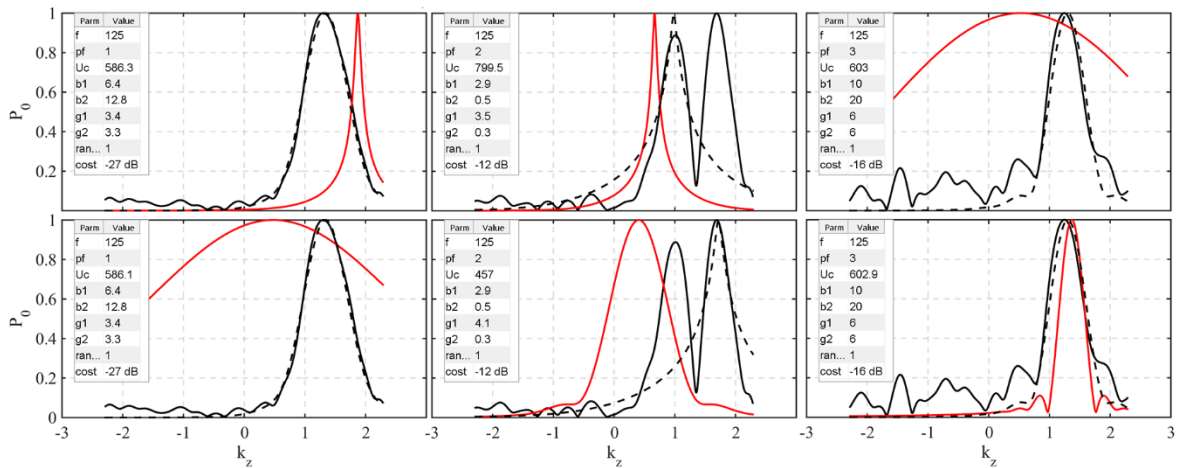


Figure 4-12. Amplitude of the wavenumber spectra corresponding to the OLVR partial fields at the lip line (solid, black), wavepacket best fits (dotted, black), and the initial conditions given to the optimization algorithm (solid, red) at 125 Hz and afterburner engine conditions.

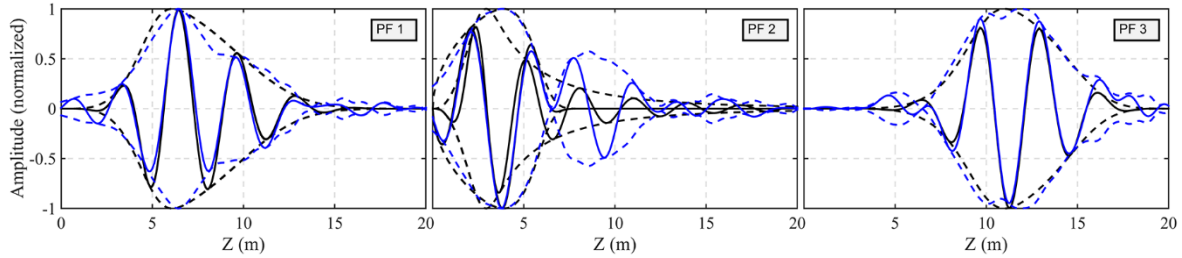


Figure 4-13. First three OLVR partial fields along the F-22 lip line (blue), and the corresponding wavepacket best fits (black), at 160 Hz and afterburner engine conditions.

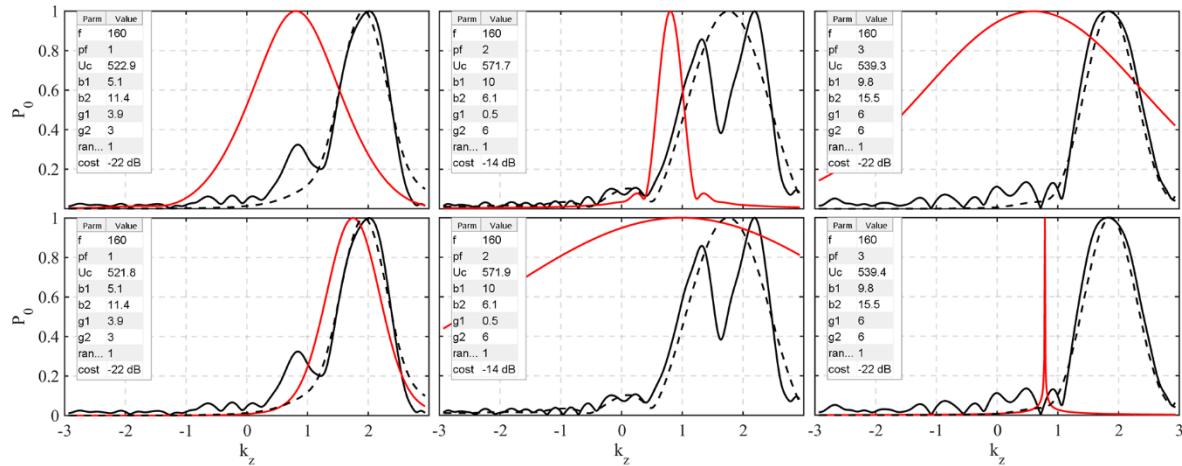


Figure 4-14. Amplitude of the wavenumber spectra corresponding to the OLVR partial fields at the lip line (solid, black), wavepacket best fits (dotted, black), and the initial conditions given to the optimization algorithm (solid, red) at 160 Hz and afterburner engine conditions.

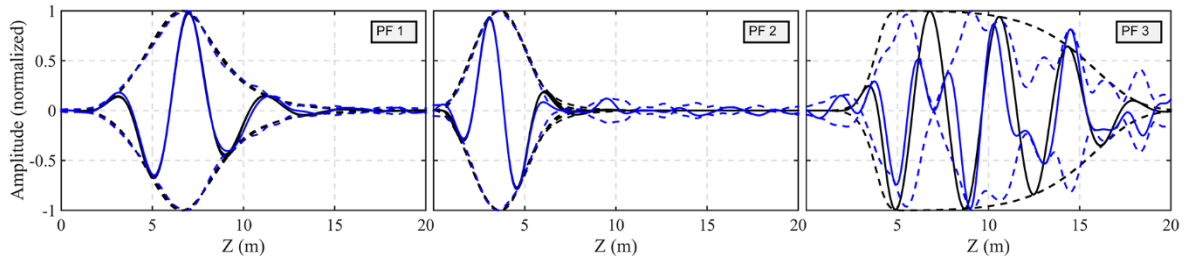


Figure 4-15. First three OLVR partial fields along the F-22 lip line (blue), and the corresponding wavepacket best fits (black), at 200 Hz and afterburner engine conditions.

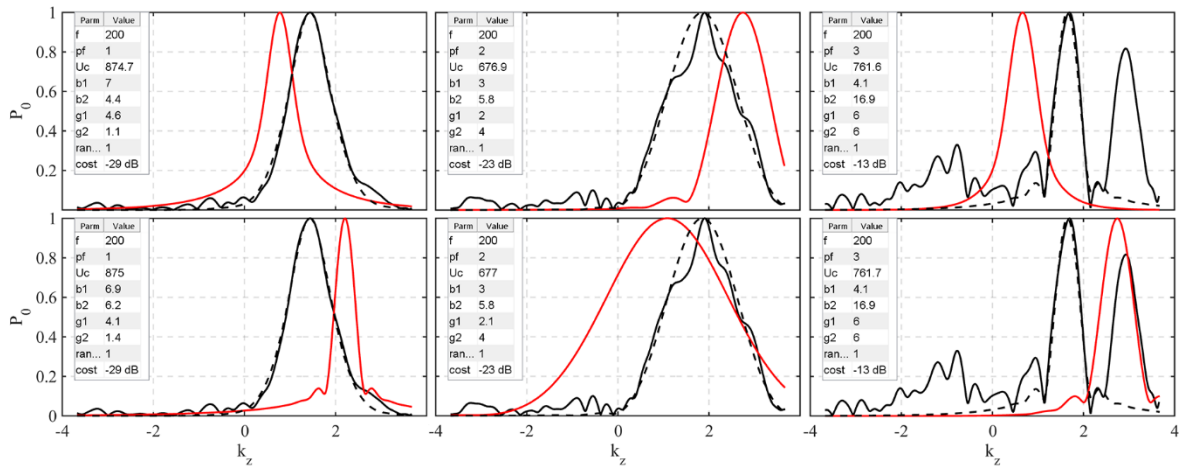


Figure 4-16. Amplitude of the wavenumber spectra corresponding to the OLVR partial fields at the lip line (solid, black), wavepacket best fits (dotted, black), and the initial conditions given to the optimization algorithm (solid, red) at 200 Hz and afterburner engine conditions.

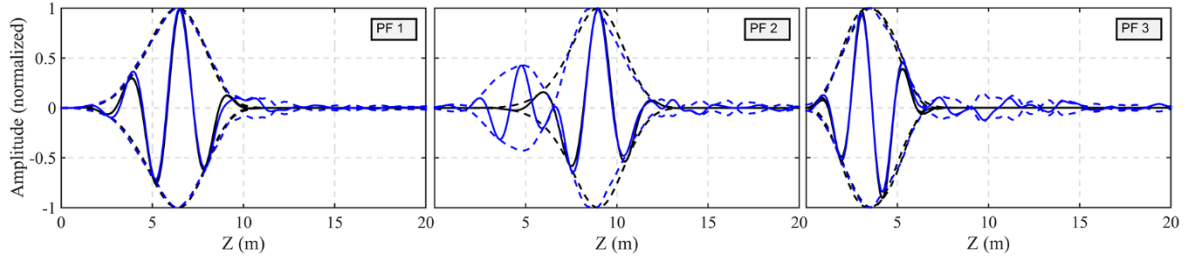


Figure 4-17. First three OLVR partial fields along the F-22 lip line (blue), and the corresponding wavepacket best fits (black), at 250 Hz and afterburner engine conditions.

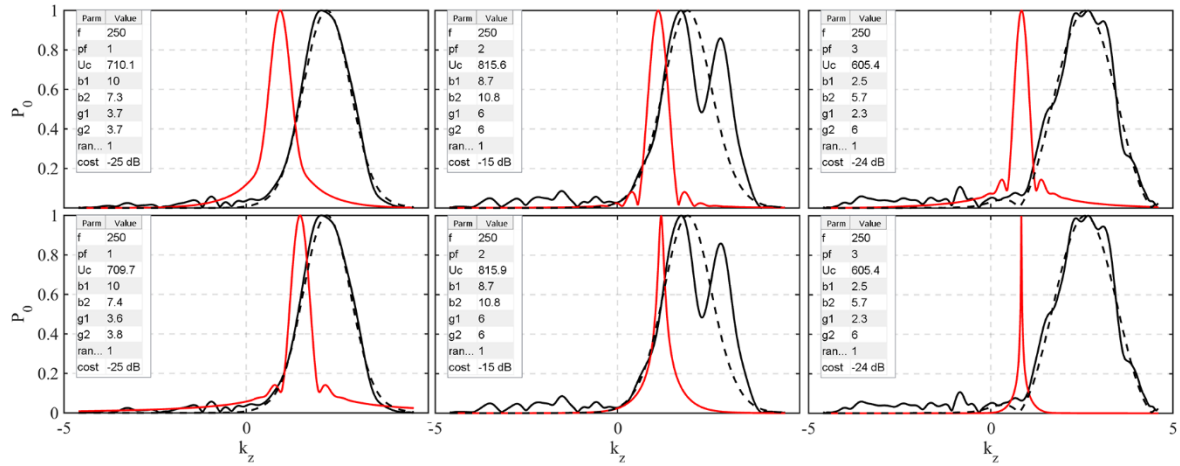


Figure 4-18. Amplitude of the wavenumber spectra corresponding to the OLVR partial fields at the lip line (solid, black), wavepacket best fits (dotted, black), and the initial conditions given to the optimization algorithm (solid, red) at 250 Hz and afterburner engine conditions.

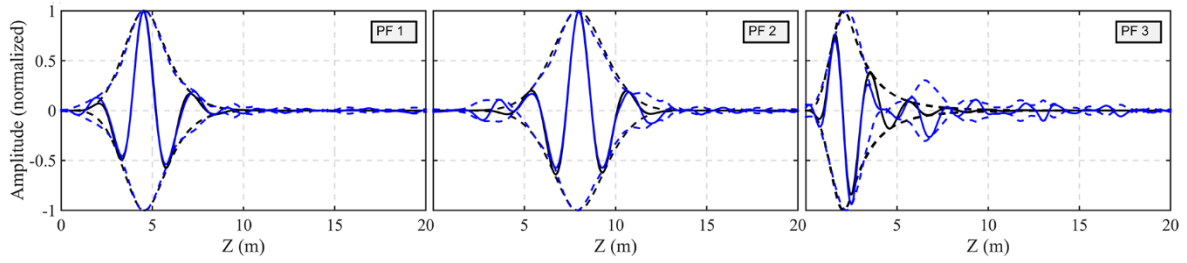


Figure 4-19. First three OLVR partial fields along the F-22 lip line (blue), and the corresponding wavepacket best fits (black), at 315 Hz and afterburner engine conditions.

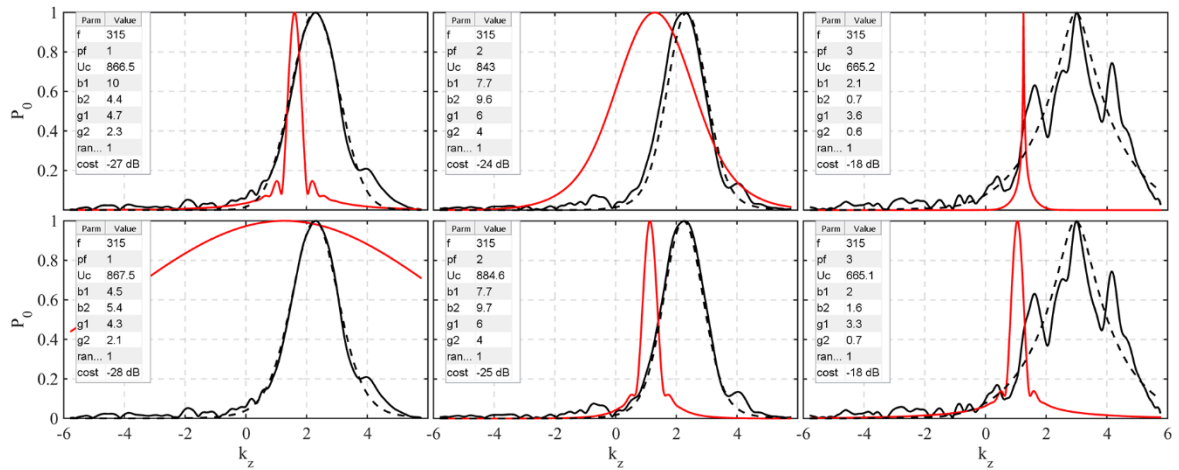


Figure 4-20. Amplitude of the wavenumber spectra corresponding to the OLVR partial fields at the lip line (solid, black), wavepacket best fits (dotted, black), and the initial conditions given to the optimization algorithm (solid, red) at 315 Hz and afterburner engine conditions.

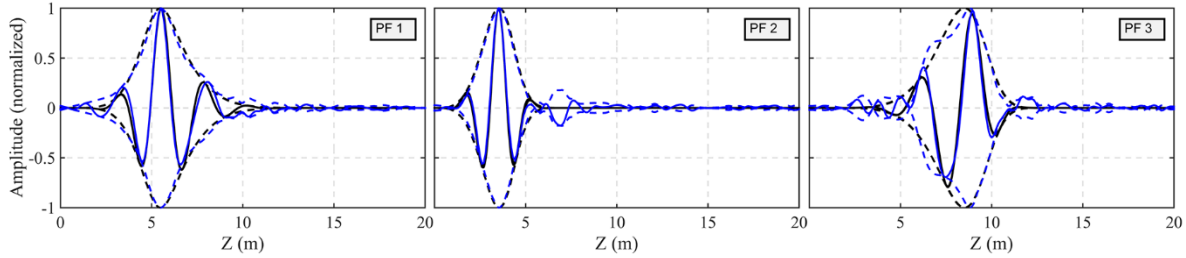


Figure 4-21. First three OLVR partial fields along the F-22 lip line (blue), and the corresponding wavepacket best fits (black), at 400 Hz and afterburner engine conditions.

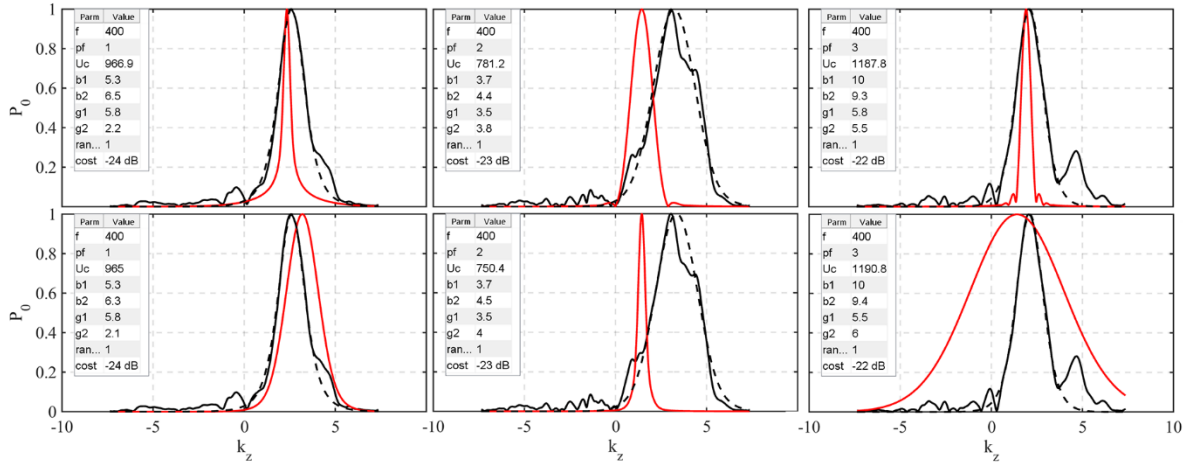


Figure 4-22. Amplitude of the wavenumber spectra corresponding to the OLVR partial fields at the lip line (solid, black), wavepacket best fits (dotted, black), and the initial conditions given to the optimization algorithm (solid, red) at 400 Hz and afterburner engine conditions.

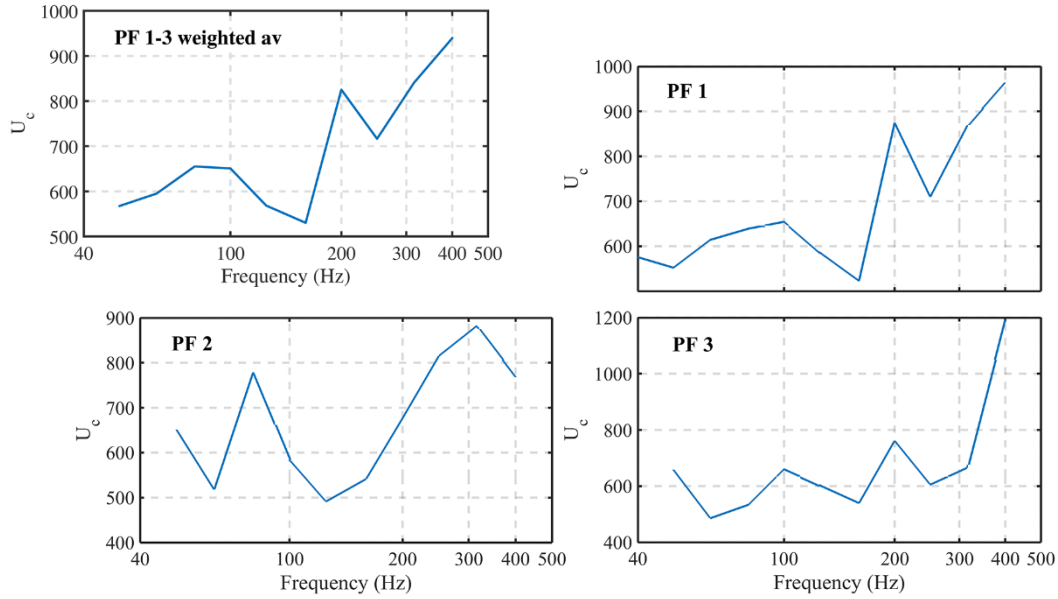


Figure 4-23. Convective velocity U_c in meters per second as a function of frequency, averaged over iterations of the optimization algorithm. These values are extracted from the parameters corresponding to wavepackets that best fit the OLVR partial fields. Results averaged over the first three partial fields, with weighting applied corresponding to the total summed energy in each partial field, are shown at the top left.

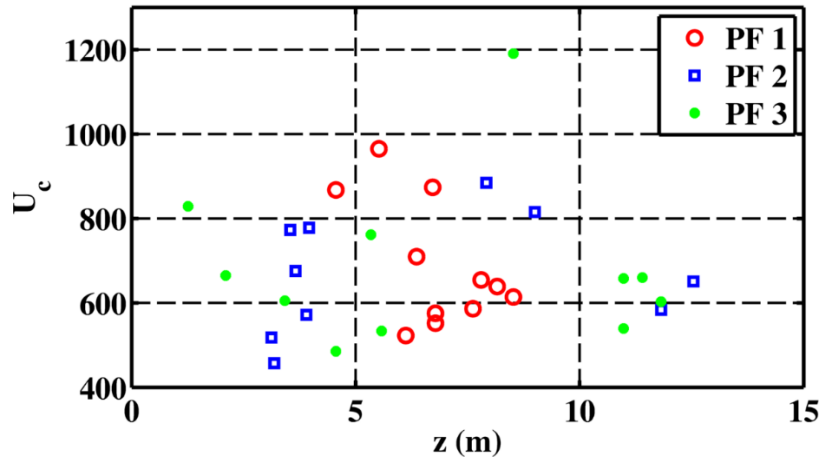


Figure 4-24. Minimum-cost wavepacket convective velocities as a function of wavepacket peak location. The results pertaining to each partial field are distinguished by symbol and color.

Plots of the apparent wavepacket convective velocity as a function of frequency are also included below, for individual partial field number, and averaged between the first three partial

fields (Fig. 4-23). In the average between the three partial fields, weighting is given to each corresponding to its total summed energy along the lip line. The evident trend is that convective velocities increase as a function of frequency, from about 550 to 1000 meters per second for 50-400 Hz, with a dramatic jump in velocity at 200 Hz from about 550 to 750 meters per second.

In addition, to test any connection between the optimized wavepacket peak locations and the peak wave the convective velocity from the optimization with the lowest cost function is plotted as a function of wavepacket peak location and partial field (Fig. 4-24). Interestingly, the first partial field tends to correlate with wavepackets that peak between about 4.5 and 8 m downstream, while those associated with the second and third partial fields tend to peak outside of that range. However, the slightly downward trend of velocity with peak location is not as apparent as the upward trend in frequency (see Fig. 4-23). This trend is expected because the overall fluid velocity should decrease as a function of downstream distance. Again, the relationship may possibly be made clearer by a different method^{18,55} of selection for virtual reference locations (see Chapter 3), a topic which merits further research. Chapter 4 summary

This study is among the first applications of the wavepacket model to military-scale jet noise, and is the first attempt to match partial fields from the full-scale jet NAH sound field reconstructions to wavepacket shapes. These results are largely promising in that the first partial field is well-matched by the hyperbolic tangent wavepacket shape above 40 Hz, and the agreement with other partial fields also increases with increasing frequency. Though the parameter space is largely flat, a simulated annealing algorithm converges well to a similar wavepacket shape and associated convective velocity. More rigorous optimization methods may improve this convergence.

Chapter 5

5.1 Conclusion

Using a three-dimensional vector acoustic intensity probe and a novel processing method (PAGE²⁴), maps of the measured sound energy flow near a static F-22 Raptor have been created and analyzed as a function of frequency and engine condition. Next, leveraging the full host of acoustical measurements from the experiment, a modified SONAH algorithm has produced full three-dimensional visualizations of the energy flow near the F-22, in a much finer resolution and closer to the shear layer than allowed by physical hardware limitations. In addition, the full SONAH⁴³⁻⁴⁵ field reconstructions have been deconstructed into physically relevant partial fields via an OLVR⁵⁴ algorithm. These partial fields, which describe the contributions from independent radiators, were extended to the lip line of the F-22 jet nozzle, where wavepackets (an equivalent source model) are typically modeled. Wavepacket parameters were optimized to best match the OLVR partial fields, revealing both the utility of the wavepacket model and important physical characteristics of the acoustical source.

The most important results of these individual methods pertaining to source characterization are summarized in the following paragraphs. In general, straightforward measurement of the acoustic intensity at a limited number of data locations has been shown capable of characterizing the location and directivity of a complicated acoustic source. This thesis also presents the first intensity reconstructions from holography applied to a full-scale jet plume, resulting in complete visualizations of the sound energy flow near the aircraft.

Maps of the energy flow near the F-22 jet plume give the expected result that peak source location moves upstream and its extent contracts with increasing frequency. Above about 300 Hz, the source region for afterburner is about 1 m farther downstream than at military power, and is somewhat broader by up to 1 m in width above 200 Hz. Intensity vector angles at afterburner are directed up to ten degrees farther forward on average than for military engine conditions. Also, the transition in source location at low frequency (from 100 to 400 Hz) for the F-22 occurs more rapidly than similar transition regions in laboratory-scale jets.

After NAH reconstruction at all points near the jet, the energy flow field is shown to be dominated by one radiation lobe at low frequencies, increasing to two at about 160 Hz. Vector intensity directions across each radiation lobe are consistent at farther than 1-2 m from the jet shear layer. Use of OLVR separates individual radiation lobes from 160-250 Hz, indicating that multiple mutually incoherent acoustical sources are important in this frequency region.

Finally, optimization results indicate that the hyperbolic tangent wavepacket model can successfully model partial fields above about 50 Hz, using multiple wavepackets at each frequency. Modeled convective velocity, deduced from the wavepacket parameters, increases as a function of frequency, from about 550 to 1000 meters per second at 50-400 Hz, with a dramatic jump in velocity at 200 Hz from about 550 to 750 meters per second.

5.2 Contributions

This research has been collaborative in nature, and would not have been possible without the work of many other students and faculty at Brigham Young University, and results from other studies in the literature. Specific contributions from the author include calculation and verification of intensity measurements, creation of the vector maps in Chapter 2, development and implementation of the ray-tracing method in Sec. 2.6 and subsequent simulation and analysis, modification and implementation of M-SONAH and OLVR to produce and analyze vector intensity field reconstructions and partial fields in Chapter 3, and implementation of an optimization algorithm to fit wavepacket parameters to partial fields in Chapter 4.

5.3 Future work

Some topics that merit further research have been pointed out by this thesis. To better separate contributions from individual radiators to the total intensity field, alternative methods of selecting virtual reference locations should be investigated for use in the OLVR algorithm (Chapter 3). These new partial fields should also be investigated for improvement to the wavepacket shape optimizations in Chapter 4. In addition, the intensity field produced by the analytical wavepacket model should be considered, and compared with the measured intensity field. In future work, comparison with results of these methods using intensity data from other scales of jet plumes would also be beneficial.

References

- ¹ P. Kuronen, E. Toppila, J. Starck, R. Paakkonen, and M. J. Sorri, “Modelling the risk of noise-induced hearing loss among military pilots,” *Int. J. Audiology* **43**, 79-84 (2004).
- ² J. Laufer, R. Schlinker, and R. E. Kaplan, “Experiments on supersonic jet noise,” *AIAA J.* **14**(4), 489-497 (1976).
- ³ C. K. W. Tam, K. Viswanathan, K. K. Ahuja, and J. Panda, “The sources of jet noise: experimental evidence,” *J. Fluid Mech.* **615**, 253-292 (2008).
- ⁴ J. Panda, and R. Mosher, “Use of a microphone phased array to determine noise sources in a rocket plume,” 49th Aerospace Sci. Mtg., AIAA 2011-974 (2011).
- ⁵ S. Dumbacher, J. Blough, D. Hallman, and P. Wang, *Source identification using acoustic array techniques*, SAE Technical Paper, No. 951360, (1995).
- ⁶ B. J. Greska, *Supersonic jet noise and its reduction using microjet injection*, (Ph. D. Dissertation, Florida State University, Tallahassee, FL, 2005).
- ⁷ S. R. Ventakesh, D. R. Poak, and S. Narayana, “Beamforming algorithm for distributed source localization and its application to jet noise,” *AIAA J.* **41**, 1238–1246 (2003).
- ⁸ S. M. Jaeger and C. S. Allen, “Two-dimensional sound intensity analysis of jet noise,” AIAA paper 93-4342 (1993).

- ⁹ K. L. Gee, J. H. Giraud, J. D. Blotter, and S. D. Sommerfeldt, "Near-field vector intensity measurements of a small solid rocket motor," *J. Acoust. Soc. Am.* **128**, EL69–EL74 (2010).
- ¹⁰ K. L. Gee, J. H. Giraud, J. D. Blotter, and S. D. Sommerfeldt, "Energy-based acoustical measurements of rocket noise," AIAA Paper 2009-3165 (2009).
- ¹¹ R. Schlinker, S. Liljenberg, D. Polak, K. Post, C. Chipman, and A. Stern, "Supersonic Jet Noise Characteristics & Propagation: Engine and Model Scale," AIAA Paper No. 2007-3623 (2007).
- ¹² T. A. Stout, K. L. Gee, T. B. Neilsen, A. T. Wall, and M. M. James, "Source characterization of full-scale jet noise using vector intensity," *J. Acoust. Soc. Am.*, (paper draft, 2015).
- ¹³ T. A. Stout, K. L. Gee, T. B. Neilsen, A. T. Wall, and M. M. James, "Intensity analysis of the dominant frequencies of military jet aircraft noise," *Proc. of Mtgs. Acoust.* **20**, 040010, (2014).
- ¹⁴ A. T. Wall, K. L. Gee, M. M. James, K. A. Bradley, S. A. McInerny, and T. B. Neilsen, "Near-field noise measurements of a high-performance jet aircraft," *Noise Control Eng. J.* **60**, 421–434 (2012).
- ¹⁵ M. M. James and K. L. Gee, "Aircraft jet plume source noise measurement system," *Sound Vib.* **44**, 14–17 (2010).
- ¹⁶ A. T. Wall, K. L. Gee, T. B. Neilsen, R. L. McKinley, and M. M. James, "Military jet noise source imaging using multisource statistically optimized near-field acoustical holography," *J. Acoust. Soc. Am.* (submitted 2015).
- ¹⁷ A. T. Wall, K. L. Gee, T. B. Neilsen, and M. M. James, "Acoustical holography and proper orthogonal decomposition methods for the analysis of military jet noise," *Proc. Noise-Con*, (2013).

- ¹⁸ A. T. Wall, K. L. Gee, T. B. Neilsen, B. M. Harker, S. A. Mcinerny, R. L. McKinley, and M. M. James, "Investigation of multi-lobed fighter jet noise sources using acoustical holography and partial field decomposition methods," AIAA Paper draft (2015).
- ¹⁹ B. M. Harker, T. B. Neilsen, K. L. Gee, A. T. Wall, and M. M. James, "Spatiotemporal correlation analysis of jet noise from a high-performance military aircraft," AIAA Paper draft (2015).
- ²⁰ B. M. Harker, K. L. Gee, T. B. Neilsen, A. T. Wall, and M. M. James, "Phased-array measurements of full-scale military jet noise," AIAA Paper 2014-3069 (2014).
- ²¹ T. B. Neilsen, K. L. Gee, A. T. Wall and M. M. James, "Similarity spectra analysis of high-performance jet aircraft noise," *J. Acoust. Soc. Am.* **133**, 2116 (2013).
- ²² T. B. Neilsen, K. L. Gee, A. T. Wall, M. M. James and A. A. Atchley, "Comparison of supersonic full-scale and laboratory-scale jet data and the similarity spectra for turbulent mixing noise," *Proc. Mtgs. Acoust.* **19**, 040071 (2013).
- ²³ J. Morgan, T. B. Neilsen, K. L. Gee, A. T. Wall, and M. M. James, "Simple-source model of high-power jet aircraft noise," *Noise Control Eng. J.* **60**, 435–449 (2012).
- ²⁴ D. C. Thomas, B. Y. Christensen, K. L. Gee, "Phase and amplitude gradient method for the estimation of acoustic vector quantities," accepted to *J. Acoust. Soc. Am.* (2015).
- ²⁵ R. Raangs, W. F. Druyvesteyn, and H. E. De Bree, "A low-cost intensity probe," *Journal of the Audio Engineering Society*, **51** (5):344-357 (2003).
- ²⁶ F. Jacobsen, "Sound intensity measurements," Malcolm J Crocker, editor, *Handbook of Noise and Vibration Control*, pgs. 534-548. John Wiley, Hoboken, N.J. (2007).

- ²⁷ M. M. James and K. L. Gee, "Advanced acoustic measurement system for rocket noise source characterization" Proc. Internoise, 7602-7614, Institute of Noise Control Engineering (2012).
- ²⁸ J. H. Giraud, K. L. Gee, and J. E. Ellsworth, "Acoustic temperature measurement in a rocket noise field," J. Acoust. Soc. Am., **127** (5): EL179-EL184 (2010).
- ²⁹ F. J. Fahy, *Sound Intensity*, pages 97-105, (CRC Press, 2002).
- ³⁰ J. H. Giraud, *Experimental analysis of energy-based acoustic arrays for measurement of rocket noise fields* (M.S. Thesis, Brigham Young University, Provo, 2013).
- ³¹ J.-C. Pascal and J.-F. Li, "A systematic method to obtain 3D finite-difference formulations for acoustic intensity and other energy quantities," J. Sound Vib. **310**, 1093–1111 (2008).
- ³² C. P. Wiederhold, K. L. Gee, J. D. Blotter, S. D. Sommerfeldt, and J. H. Giraud. "Comparison of multimicrophone probe design and processing methods in measuring acoustic intensity," J. Acoust. Soc. Am. **135** (5), 2797-2807 (2014).
- ³³ T. B. Neilsen, K. L. Gee, and M. M. James, "Spectral characterization in the near and mid-field of military jet aircraft noise," AIAA Paper 2013-2191 (2013).
- ³⁴ C. K. Tam and S. Parrish, "Noise of high-performance aircrafts at afterburner," AIAA Paper 2014-2754 (2014).
- ³⁵ C. K. W. Tam, M. Golebiowski, and J. M. Seiner, "On the Two Components of Turbulent Mixing Noise from Supersonic Jets," AIAA Paper 96-1716, (1996).
- ³⁶ K. L. Gee, V. W. Sparrow, M. M. James, J. M. Downing, C. M. Hobbs, T. B. Gabrielson, and A. A. Atchley, "The role of nonlinear effects in the propagation of noise from high-power jet aircraft," J. Acoust. Soc. Am. **123** (6), 4082-4093, (2008).

- ³⁷ T. A. Stout, K. L. Gee, T. B. Neilsen, A. T. Wall, and M. M. James, "Acoustic intensity near a high-powered military jet aircraft," accepted to *J. Acoust. Soc. Am.* EL, (2015).
- ³⁸ S. S. Lee and J. Bridges, "Phased-array measurements of single flow hot jets," AIAA Paper 2005-2842, (2005).
- ³⁹ D. Papamoschou and A. Dadvar, "Localization of multiple types of jet noise sources," AIAA Paper 2006-2644, (2006).
- ⁴⁰ R. Dougherty and J. Mendoza, "Phased Array Beamforming with 100-Foot Polar Arc Microphones in a Static Engine Noise Test," Paper No. 2008-51, AIAA, (2008).
- ⁴¹ D. Papamoschou, "Wavepacket modeling of the jet noise source," AIAA Paper 2011-2835, (2011).
- ⁴² P. Jordan and T. Colonius, "Wave packets and turbulent jet noise," *Annu. Rev. Fluid Mech.* **45**, 173-195, (2013).
- ⁴³ J. Hald, "Basic theory and properties of statistically optimized near-field acoustical holography," *J. Acoust. Soc. Am.* **125**, 2105-2120, 2009.
- ⁴⁴ Y. T. Cho, J. S. Bolton and J. Hald, "Source visualization by using statistically optimized near-field acoustical holography in cylindrical coordinates," *J. Acoust. Soc. Am.* **118**, 2355, 2005.
- ⁴⁵ R. Steiner and J. Hald, "Near-field acoustical holography without the errors and limitations caused by the use of spatial DFT," *Int. J. Sound Vib.* **6**, 83-89, 2001.
- ⁴⁶ M. Lee and J. S. Bolton, "Source characterization of a subsonic jet by using near-field acoustical holography," *J. Acoust. Soc. Am.* **121**, 967-977, 2007.
- ⁴⁷ A. T. Wall, K. L. Gee, T. B. Neilsen, and M. M. James. "Acoustical holography imaging of full-scale jet noise fields." INTER-NOISE and NOISE-CON Congress and Conference Proceedings. **246**, 1, 2013.

- ⁴⁸ J. Hald, "Patch holography in cabin environments using a two-layer hand-held array and an extended SONAH algorithm," Proceedings of Euronoise 2006, 2006.
- ⁴⁹ D. W. Krueger, *Array-based characterization of military jet aircraft noise* (M.S. Thesis, Brigham Young University, Provo, 2012).
- ⁵⁰ A. T. Wall, K. L. Gee, T. B. Neilsen, D. W. Krueger, M. M. James, S. D. Sommerfeldt and J. D. Blotter, "Full-scale jet noise characterization using scan-based acoustical holography," AIAA Paper 2012-2081, 2012.
- ⁵¹ A. T. Wall, *The characterization of military aircraft jet noise using near-field acoustical holography methods*, (Dissertation, Brigham Young University, Provo, UT, 2013).
- ⁵² J. Hald, "Patch near-field acoustical holography using a new statistically optimal method," Proc. INTER-NOISE, 2203–2210 (2003).
- ⁵³ E. G. Williams, *Fourier acoustics: Sound radiation and nearfield acoustical holography*, (Academic Press, San Diego, 1999).
- ⁵⁴ Y. J. Kim, J. S. Bolton and H. S. Kwon, "Partial sound field decomposition in multireference nearfield acoustical holography by using optimally located virtual references," J. Acoust. Soc. Am. **115**, 1641-1652 (2004).
- ⁵⁵ A. T. Wall, *et al.*, J. Acoust. Soc. Am. (paper in preparation, 2015).
- ⁵⁶ A. T. Wall, K. L. Gee, M. D. Gardner, T. B. Neilsen and M. M. James, "Near-field acoustical holography applied to high-performance jet aircraft noise," Proc. Mtgs. Acoust. **9**, 040009, 2011.
- ⁵⁷ A. T. Wall, K. L. Gee, D. W. Krueger, T. B. Neilsen, S. D. Sommerfeldt and M. M. James, "Aperture extension for near-field acoustical holography of jet noise," Proc. Mtgs. Acoust. **14**, 065001, 2013.

- ⁵⁸ C. K. W. Tam, K. Viswanathan, K. K. Ahuja, and J. Panda, “The sources of jet noise: experimental evidence”, *J. Fluid Mech.* **615**, 253–292, (2008).
- ⁵⁹ N.P. Valdivia and E.G. Williams, “Study of the comparison of the methods of equivalent sources and boundary element methods for near-field acoustic holography”, *J. Acoust. Soc. Am.*, **120**, 3694–3705, (2006).
- ⁶⁰ M.J. Lighthill, “On Sound generated aerodynamically. Part 1. General Theory”, *Royal Soc. London*, **211**, 564–587, (1952).
- ⁶¹ S. A. E. Miller, "The prediction of jet noise ground effects using an acoustic analogy and a tailored Green's function," *J. Sound Vib.* **333**(4), 1193-1207 (2014).
- ⁶² R. Reba, S. Narayanan, T. Colonius, and T. Suzuki, "Modeling jet noise from organized structures using near-field hydrodynamic pressure," *AIAA Paper 2005-3093*, (2005).
- ⁶³ K. Gudmundsson, and T. Colonius. "Instability wave models for the near-field fluctuations of turbulent jets," *J. Fluid Mech.* **689**, 97-128 (2011).
- ⁶⁴ D. Papamoschou, "Prediction of jet noise shielding," *AIAA paper 2010-653*, (2010).
- ⁶⁵ J. Varnier, “Experimental study and simulation of rocket engine free jet noise,” *AIAA J.* **39**, 1851–1859 (2001).
- ⁶⁶ R. Reba, J. Simonich, and R. Schlinker, "Measurement of source wave-packets in high-speed jets and connection to far-field sound," *AIAA Paper 2008-2891*, (2008).
- ⁶⁷ D. M. Hart, *Bayesian optimization of an equivalent source model for military jet aircraft*, (BS Thesis, Brigham Young University, Provo, UT, 2013)
- ⁶⁸ T. B. Neilsen, K. L. Gee, D. M. Hart, and M. M. James, “Sensitivity analysis of an equivalent source model for military jet aircraft noise,” *Proc. Mtgs. Acoust.* **20**, 045002 (2014); <http://dx.doi.org/10.1121/1.4865249>

⁶⁹ A. T. Wall, K. L. Gee, T. B. Neilsen, and M. M. James, “Partial field decomposition of jet noise sources using optimally located virtual reference microphones,” Proc. Mtgs. Acoust. **18**, 045001 (2012).

⁷⁰ F. Jacobsen, “Sound intensity and its measurement and applications,” Acoustic Technology, Technical University of Denmark (2006).

Appendix

A. Intensity analysis of the dominant frequencies of military jet aircraft noise

Appendix A contains a slightly modified Proceedings of Meetings on Acoustics paper¹³ detailing investigations into the possibility of a dual source mechanism in the F-22 jet plume near 200 Hz. As discussed in the main body of the thesis, this possibility is evidenced by two high-intensity regions, and two radiation lobes, which discretely shift in prominence as frequency is varied.

A.1 Introduction

Acoustic intensity measurements of the F-22A Raptor have been analyzed as part of ongoing efforts to characterize the noise radiating from military jet aircraft. In addition, array-based methods using measurements outside of the jet plume have been used to study important acoustic quantities. Techniques such as beamforming,⁷ near-field acoustical holography,^{46,50,56}

coherence analysis methods, etc. have previously been applied to predict the frequency-dependent nature of sound radiation and source location within the plume.

Intensity, a direct measure of energy flow in a sound field, has not seen much application to jet noise analysis. However, measurement of the vector intensity can provide a map of the frequency-specific sound radiation from turbulent flows. For example, Jaeger and Allen⁸ used a two-dimensional intensity probe to characterize source location within jet plumes of Mach numbers 0.2-0.6, one of the most in-depth applications to aeroacoustics. Recently, three-dimensional intensity probes have been used to measure the sound field of a solid rocket motor plume.^{9,10,27} The same probe design was also used to make near-field acoustic intensity measurements of the F-22A Raptor. The intensity probe was attached to the top of a 90-microphone rectangular array of microphones, which was moved to multiple locations to the sideline and aft of the aircraft.

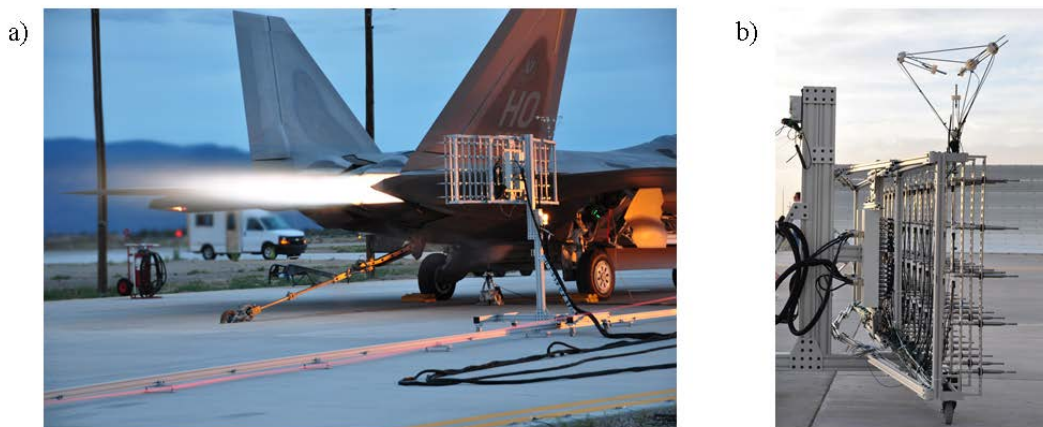


Figure A-1. (a) F-22 engine firing with rig and probe in place, and (b) close-up of the intensity probe positioned on top of the microphone array. The array and probe took measurements at several locations along guide rails while the engine was cycled through four power conditions.

Figure A-2 describes the physical layout of the measurements. The F-22 was tethered to the

center of a concrete run-up pad, and one engine was run up to different conditions while the other was held at idle. The rectangular array and intensity probe were used to acquire measurements at each location for four different conditions: idle, intermediate (80% throttle), military (full throttle), and afterburner. Multiple references explain the procedure and measurement apparatus.^{14,15} In this paper, the intensity measurements are used to explore some unexpected results found by other analysis methods in the peak-frequency region of the F-22 spectrum.

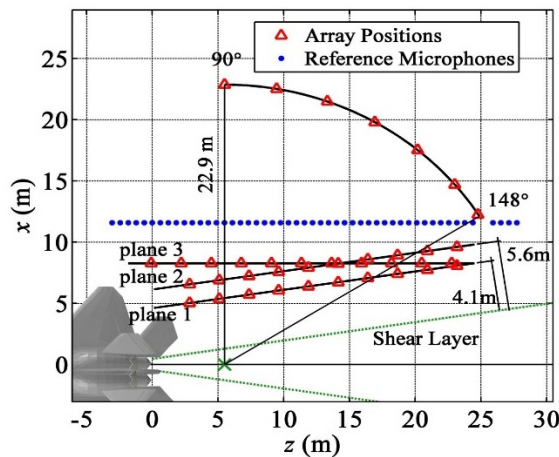


Figure A-2. Top-down schematic of data locations for the F-22 measurements. The red triangles indicate the center of the microphone rig with the intensity probe attached. The mark at 5.5 m downstream describes the estimated source location, set as the center of the 22.9m arc. The blue dots show locations for the ground-based reference array.

A.2 Spectral Analysis

Using data from the array microphones and ground-based reference microphones, multiple analysis techniques have been used to examine the peak-frequency region (from about 100-325 Hz) of the F-22 spectrum. The spectrum recorded at the ground-based microphone locations was matched to two similarity spectra curves, which correspond to radiation from large and fine-scale

turbulence structures.^{21,22} Currently, this generalized two-source representation is a prevalent model used in jet plume source characterization. Except at high frequencies, the similarity spectra curves follow the measured data well in the general frequency trend (from low frequency to several kHz).

The similarity curves, however, do not account for a double peak in the measured spectra. Recently, discrete frequency peaks were discovered,^{21,50} from what appear to be two mutually-incoherent sources which exhibit distinct directionalities.⁴⁷ As seen in Fig. A-3, the spectrum shifts from a maximum at about 250 Hz at 120° to 125 Hz at 140°, without a smooth transition between these frequencies. The discrete nature of the spectral maxima in the peak-frequency region when considering the different radiation directions suggests a shortcoming in the similarity spectra model in the peak-frequency region.

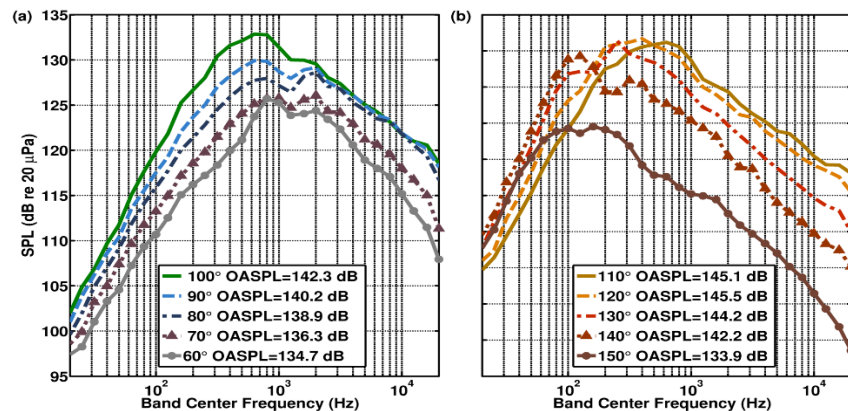


Figure A-3. One-third octave sound pressure levels measured according to direction from assumed source (5.5 m downstream), for military engine conditions (compare the same for afterburner in Ref. 21).

Another way to visualize the spatial variation in frequency content is to examine spectral maps across the ground array. An example of such a map at military power is displayed in Fig. A-4 and shows two distinct lobes – regions of high levels – centered at about 125 Hz and 400 Hz.

Between about 8 m and 24 m downstream, these lobes dominate the radiation. In the middle region, between ~14-18 m, a single microphone receives the superposition of both spectral lobes, which causes a dual peak in the spectrum. Looking from upstream to downstream in this region, the spectral maximum shifts from one lobe to the other, as seen in Fig. A-3.

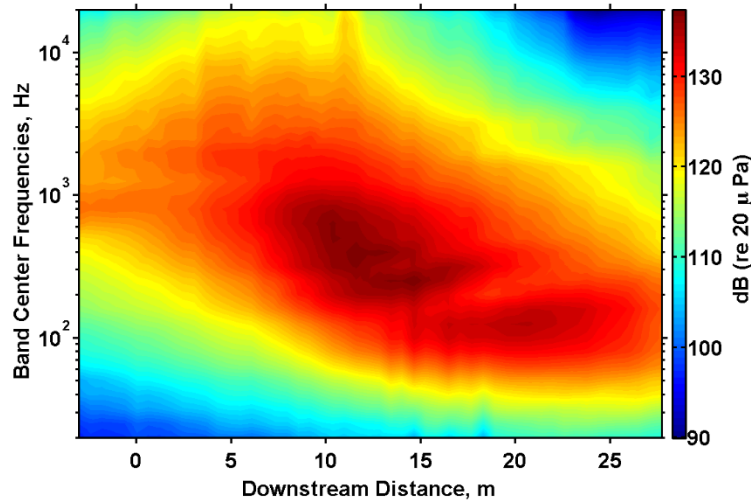


Figure A-4. One-third-octave SPL recorded by the ground microphone array for military engine conditions. Note the two distinct high-level regions centered about 125 Hz and 400 Hz that dominate the radiation from 8m to 24 m downstream.

Not only the ground microphone array, but data from the 90-microphone array also exhibits the dual spectral lobes. Figures A-7(a) and A-8(a) show the one-third-octave SPL recorded by the rig for military and afterburner engine conditions along the measurement plane 4.1 m from the shear layer (plane 1). Again, the dual spectral lobes are apparent as the spectral maximum jumps from 250 Hz to 125 Hz at 10.5-11 m downstream.

To investigate the nature of the two radiation lobes, the coherence between microphones in the ground-based array was analyzed in the peak-frequency region. Fig. A-5 shows the results at 200 Hz. The spatial coherence has two lobes of high coherence (at $z = 9-16$ m and past $z = 20$

m) that correspond to the locations of highest recorded sound power at that frequency (see bottom SPL plot). The fact that there is low coherence between microphones in these two spatial regions, and in between them as well, indicates that the mechanisms responsible for the radiation at those locations are not coherent with each other. This is supported by previous near-field acoustical holography (NAH) results, which reconstructed orthogonal partial fields with distinct directionalities.⁶⁹ Because of the way the partial fields were chosen, this result also suggests two independent source mechanisms that have different directionalities and which radiate with discrete spectral maxima. The hypothesis is tested below in a series of intensity simulations.

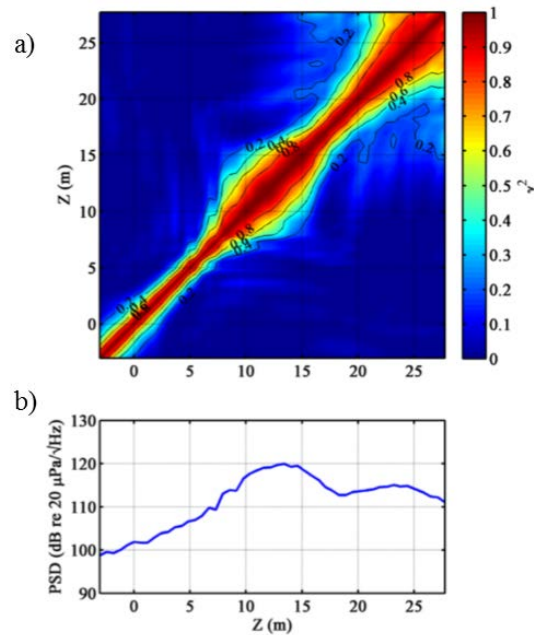


Figure A-5. (a) Coherence between microphones along the ground-based array at 200 Hz. (b) Power spectral density (PSD) values at 200 Hz, along ground-based array. Note the two lobes of high coherence at $z = 9-16$ m and past $z = 20$ m.

A.3 Intensity Measurements

Acoustic intensity vectors were calculated in the usual way based on finite-difference

techniques with cross-spectra from the four intensity probe microphones.⁷⁰ According to the tetrahedral probe geometry, the various cross-spectral components were weighted and summed to give intensity components along the three cardinal directions using the least-squares technique developed by Pascal and Li.³¹ The resulting single-frequency intensity vectors are plotted, as in Fig. A-6, at the measurement locations along plane 2 (see Fig. A-2) to give an indication of the flow of the sound near the F-22. For each frequency, a 3 dB-down region from the maximum intensity vector was identified. Intensity vectors from the 3 dB-down region were traced back to the jet center line as a method of approximating source location.

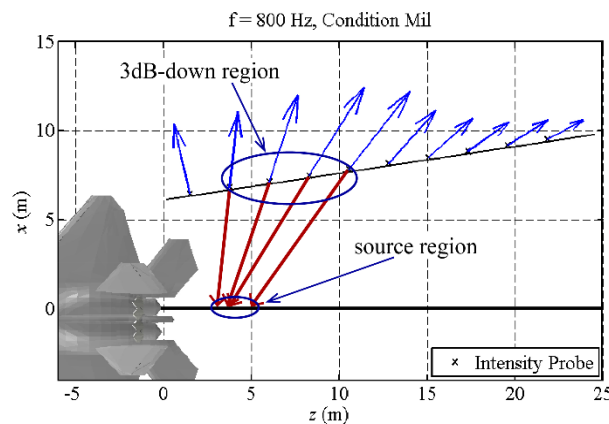


Figure A-6. Intensity results (blue arrows) at 800 Hz, including an example 3 dB-down region, shown as a circle on the second measurement plane. The intensity vectors are traced backwards to the jet centerline (red lines) to give an estimated source region at this frequency.

The approximate source regions obtained from the intensity vectors from measurement plane 2 confirm the general frequency trend expected of radiation from jet plumes. The generalized source region contracts and moves upstream with increasing frequency, as predicted by beamforming results from multiple studies.^{7,38} Figures A-7(b) and A-8(b) show the approximate source location regions for military and afterburner conditions, respectively. These approximate

source regions show the same general trends as the spatial variation in the spectral maxima measured along plane 1 using the rectangular 90-microphone array (Figs. A-7(a), A-8(a)). While results from the two engine conditions are similar, the source region above 200 Hz at afterburner remains broader and extends farther downstream than for military.

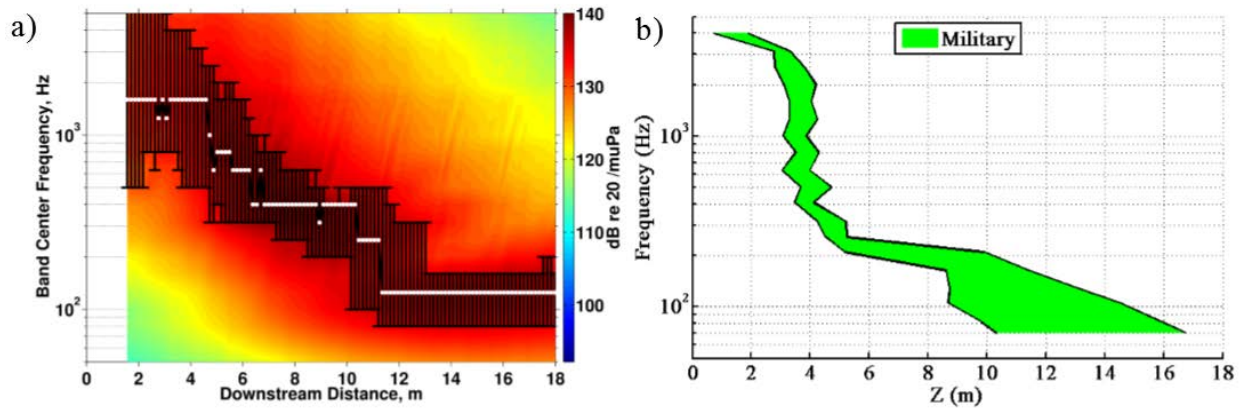


Figure A-7. (a) Height-averaged one-third-octave spectra as measured on the 90-microphone rig at 4.1 m from the shear layer (plane 1), and (b) generalized source location region vs frequency based on intensity results for military engine conditions. Error bars in (a) indicate regions within 3 dB of the spectral maximum, which is indicated as a white dot. At about 11 m downstream, the peak frequency jumps from 250 to 125 Hz. Left and right bounds in (b) describe the edges of the generalized source region estimated from tracing the intensity vectors within 3dB of the maximum; note how the source contracts and moves upstream rapidly after 200 Hz.

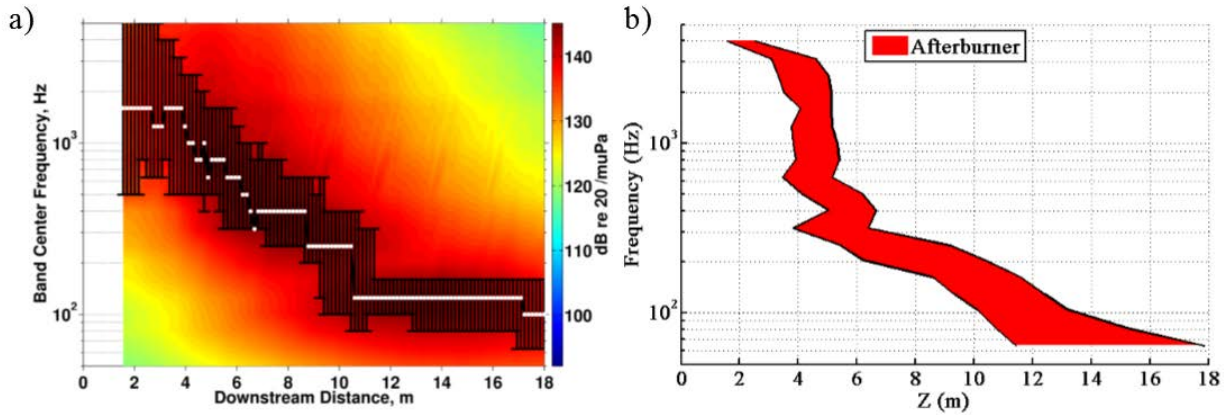


Figure A-8. (a) Height-averaged one-third-octave spectra as measured on the 90-microphone rig at 4.1 m from the shear layer (plane 1) and (b) generalized source location region vs frequency based on intensity results for afterburner engine conditions. As in Fig. A-7, error bars in (a) indicate regions within 3 dB of the spectral maximum, which is indicated as a white dot. At about 10.5 m downstream, the peak frequency jumps from 250 to 125 Hz. Left and right bounds in (b) describe the edges of the generalized source region; note how the source contracts and moves upstream rapidly after about 200 Hz. However, the source region remains broader and extends farther downstream than in Fig. A-7(b).

Figs. A-9 to A-11 show intensity measurements in the peak-frequency region. Between results from 136 Hz to 316 Hz, the maximum intensity region shifts from about $z = 20$ m farther upstream to about $z = 10$ m. Figs. A-9 and A-11 show radiation with intensity maxima centered on about $z = 20$ and $z = 10$ m, respectively. In Fig. A-10, the radiation at 232 Hz produces two spatially distinct intensity maxima. The presence of these maxima can be predicted by close scrutiny of the dual spectral lobes in Fig. A-4. At 232 Hz both lobes are present with distinct spatial locations, while at 136 Hz or 316 Hz only one spectral lobe contributes primarily.

These intensity measurements point to the possibility of two distinct source mechanisms predominantly responsible for radiation in the peak-frequency region. Supposing the presence of these two sources, Figs. A-9 to A-11 can be interpreted in terms of the source contributions to overall

radiation. Between 125 and 315 Hz, the dominating radiation shifts from one source to the other. At 136 Hz, radiation is dominated by one source which radiates at about 140 degrees (relative to the engine inlet). At 232 Hz, contributions from both sources can be seen. At 316 Hz, the second source dominates, radiating at about 120 degrees.

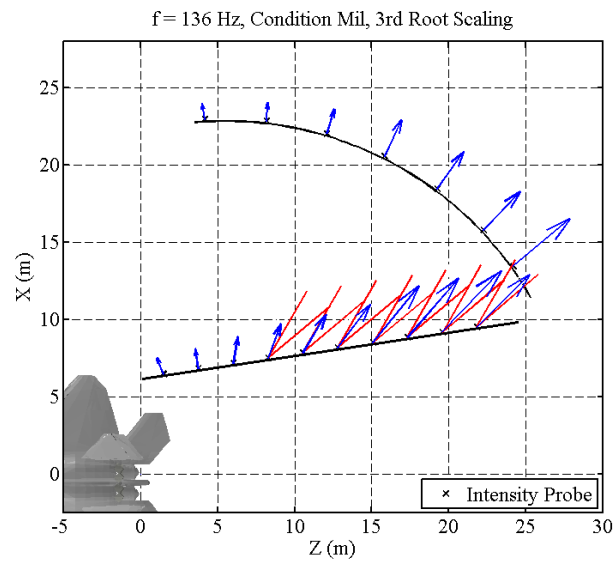


Figure A-9. Intensity measurements (blue arrows) at 136 Hz, military condition on plane 2 and the arc at 23 m. The red lines indicate 120 and 140 degrees relative to the engine inlet. The radiation at this frequency is dominated by one intensity maximum at $z = 20$ m.

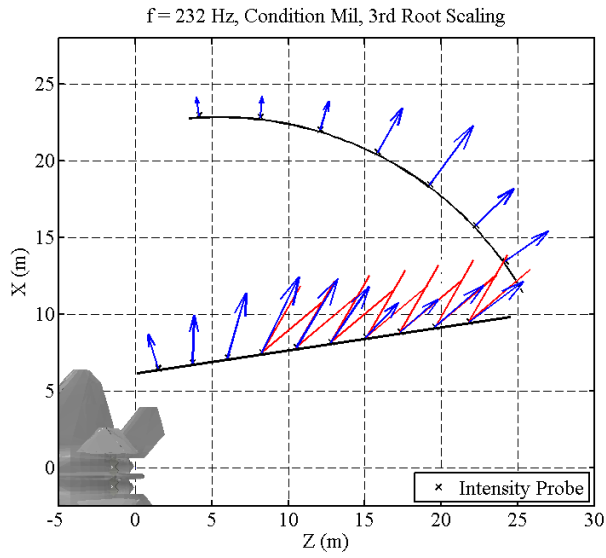


Figure A-10. Similar to Fig. A-9. Intensity measurements at 232 Hz, military condition. Note how the radiation at this frequency produces two distinct maxima, seen spatially at about $z = 10$ m and $z = 20$ m.

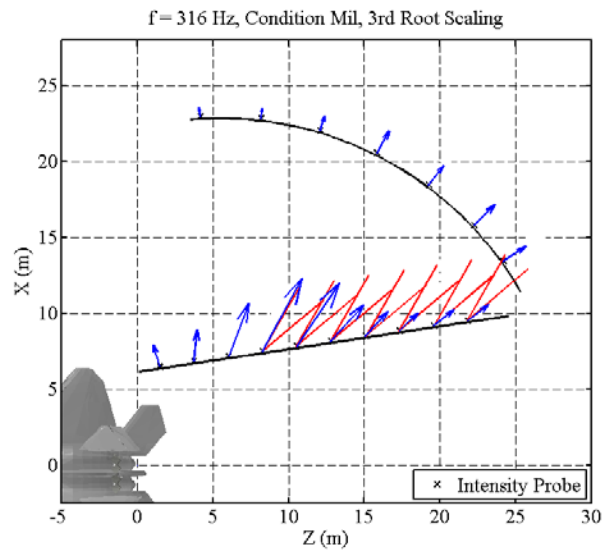


Figure A-11. Similar to Fig. A-9. Intensity measurements at 316 Hz, military condition. The radiation at this frequency is dominated by one intensity maximum at $z = 10$ m.

A.4 Intensity Simulations

To test the hypothesis that the dual lobe could be created by two independently radiating (i.e., incoherent) sources, an equivalent source model involving two line arrays of closely-spaced monopoles has been created. The model is similar to one previously used, which was designed to match to SPL at the rig locations.²³ In this previous method, large and fine-scale radiation was modeled using two line arrays at the same locations along the jet axis, one correlated (thus, directional) and the other uncorrelated. In contrast, the current model seeks to simulate the frequency-dependent intensity patterns using two, self-coherent, mutually incoherent equivalent sources (without attempting to make connections to fine-scale or large-scale flow properties). In addition, the current model is designed to be operational over a range of frequencies, rather than requiring the development of a new model for each frequency. The predictions are matched to intensity measurements rather than SPL.

The features of the two sources, suggested by the aforementioned analysis techniques and intensity measurements, include variation in source locations, radiation directions, and spectra. Monopoles are placed 2 cm apart, starting at $z = 0$ m (the engine nozzle) and ending at $z = 20$ m. Gaussian noise from each monopole is time-delayed to steer each line array in a chosen direction. Each array is comprised of correlated monopoles, with the time delay between sources as stated, but the two arrays are mutually incoherent. As shown in Fig. A-12(a), the amplitude of the noise is spatially weighted according to a Rayleigh distribution, centered at a chosen location downstream. Each source distribution is given a spectral shape according to two Butterworth bandpass filters, as displayed in Fig. A-12(b). This source representation is intended to simulate some spectral overlap between the two sources, so that from 125 to 315 Hz the dominant radiation transitions from one source to the other, with contributions from both sources at intermediate frequencies.

The lower and higher-frequency sources are centered at 10.5 and 5 m downstream, and steered with directionalities of 130 and 115 degrees, respectively. These parameters are chosen to correspond to the approximate source locations indicated by intensity ray-tracing and intensity vector directions from the 3 dB-down regions shown previously in Fig. A-6.

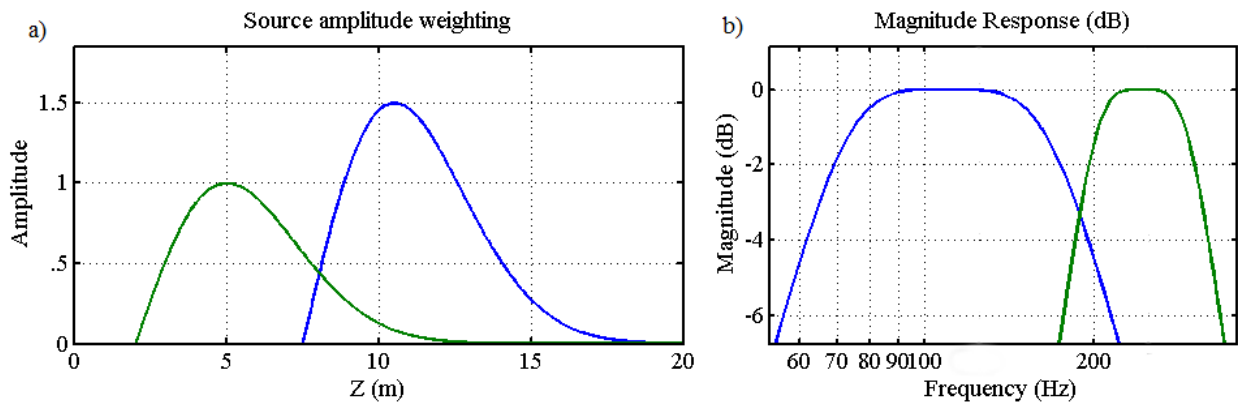


Figure A-12. (a) Location-dependent amplitude weightings of the monopole arrays, and (b) spectral response of filters applied to the noise from both correlated arrays. Coloring for each array is consistent between (a) and (b). The locations were chosen based on intensity measurement results, with centers at $z = 5$ m and $z = 10.5$ m downstream.

The measured and simulated intensities for two frequencies of interest are shown in Fig. A-13. For each measurement location, the simulated intensity is found by calculating the complex pressures and cross spectra at four positions corresponding to a simulated intensity probe. With the simple, overlapping equivalent source model, the simulated intensity results exhibit the same basic trends as the measured intensity. At 160 Hz, mixing between the two independent sources is apparent, with one directionality dominating at 20-25 m downstream, and the other at 6-12 m downstream. At 200 Hz, radiation from the upstream source dominates. The contribution from the second source at 200 Hz (at 20-25 m) is not well represented in the simulation, however, likely due to the assumed spatial extent and spectrum of the sources. Though this simulation represents

an initial, nonoptimized attempt at an equivalent source model, it shows the feasibility of two correlated arrays which are mutually incoherent in explaining the intensity measurement trends.

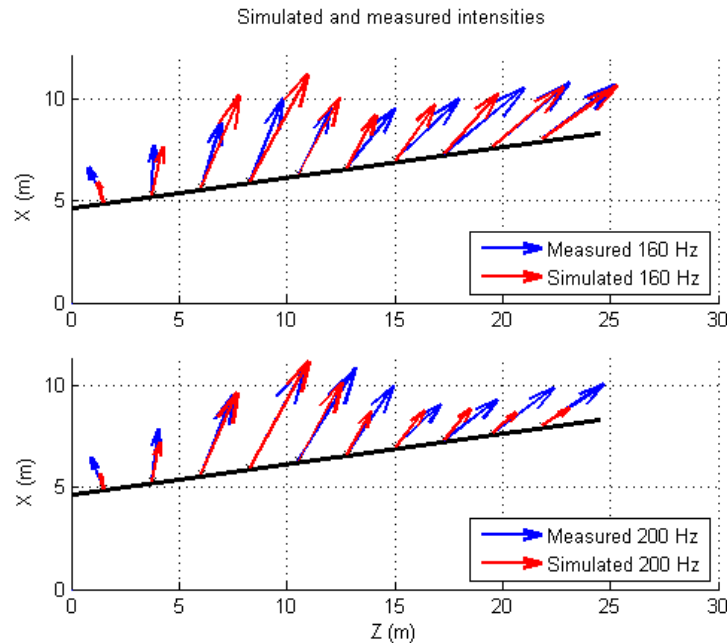


Figure A-13. Intensity simulated at the first measurement plane due to the two correlated line arrays, for 160 Hz (top) and 200 Hz (bottom). The simulation is overlaid onto measurements at 160 Hz and 200 Hz for military engine condition (blue arrows).

Conclusions

This preliminary intensity-based analysis of probe measurements near an F-22 provide a vector description of the noise field. In addition, single-frequency intensity vectors in the maximum region can be traced back to the source to provide an approximate maximum source region. The frequency variation in the estimated source regions follow trends expected for high-power jets. The intensity results around 200 Hz have two maxima, which supports previous observations that there are perhaps two mutually incoherent sources producing a double spectral

peak in the maximum radiation direction for high-performance military jet engine noise, which are not seen in laboratory-scale jets.

To further investigate this feature, an equivalent source simulation has been used to model the intensity resulting from two discrete broadband sources, which are spatially overlapped but mutually incoherent. The intensity simulations tend to agree well with intensity measurements near the F-22. In general, these results confirm the plausibility of two self-correlated, mutually uncorrelated sources with distinct spectral characteristics dominating the full-scale jet radiation in the peak-frequency region. The simulation shows the advantage of an equivalent source model in investigating how the peak-frequency region might be represented by two directional line arrays of monopoles, rather than one. Further work may extend this modeling technique in the effort to improve current theories of jet noise, and account for the anomalous discrete nature of the military fighter jet spectrum in the maximum radiation region.